ISBN 978-82-326-7472-5 (printed ver.)
ISBN 978-82-326-7471-8
(electronic ver.)
ISSN 1503-8181 (printed ver.)

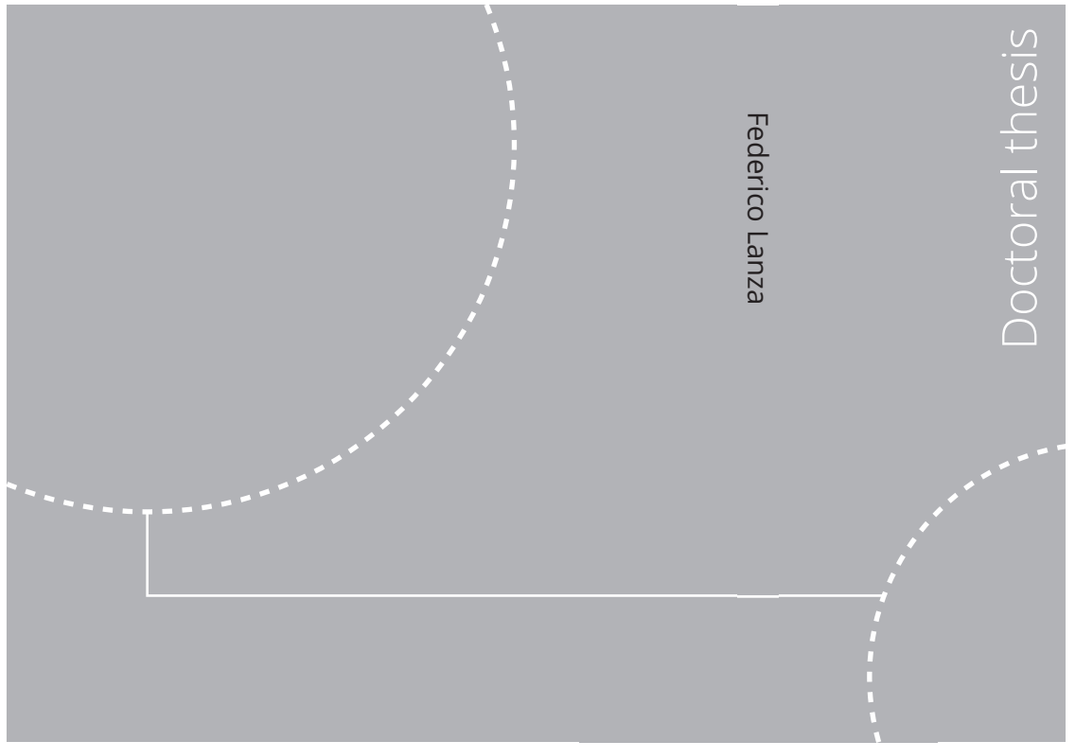

Doctoral theses at NTNU, 2023:386

Federico Lanza

Optimal path for the flow of yield stress fluid

Doctoral theses at NTNU, 2023:386

NTNU
Norwegian University of
Science and Technology
Thesis for the degree of
Philosophiae Doctor
Faculty of Natural Sciences
Department of Physics

NTNU
Norwegian University of
Science and Technology

NTNU
Norwegian University of
Science and Technology

Federico Lanza

Optimal path for the flow of yield stress fluid

Thesis for the degree of Philosophiae Doctor

Trondheim, November 2023

Norwegian University of Science and Technology
Faculty of Natural Sciences
Department of Physics

NTNU
Norwegian University of
Science and Technology

NTNU
Norwegian University of Science and Technology

Thesis for the degree of Philosophiae Doctor

Faculty of Natural Sciences
Department of Physics

ISBN 978-82-326-7472-5 (printed ver.)
ISBN 978-82-326-7471-8 (electronic ver.)
ISSN 1503-8181 (printed ver.)
ISSN 2703-8084 (electronic ver.)

Doctoral theses at NTNU, 2023:386

Printed by Skipnes Kommunikasjon AS

ABSTRACT IN ENGLISH

Numerous industrial and environmental applications rely on an understanding of fluid behavior within porous materials, from remediating groundwater contamination to carbon dioxide storage. Yield stress fluids, which resist flow until a critical stress threshold is exceeded, present both unique challenges and opportunities. Capillary forces, responsible for separating immiscible fluids, significantly influence multi-phase flow in porous structures. This thesis embarks on a theoretical exploration of non-linear flow within porous media, where both forces contribute to the overall rheology, interacting with the geometrical disorder at the pore level. The present study investigates the steady-state flow of yield stress blobs in a capillary fiber bundle filled with Newtonian liquid, as well as the flow of a single Bingham fluid in a tree-like pore network. We derive expressions for the pressure threshold and the average flow rate as a function of the applied pressure drop. In both problems, the non-linearity observed stems from the sequential opening of flowing paths with increasing pressure drop, and the distribution of pressure thresholds related to these paths defines the specific flow rate law. Furthermore, we explore the transition from viscous fingering to foam during immiscible drainage in a two-dimensional porous medium. We characterize this transition through numerical simulations using a dynamic pore network model, measuring the transition location, overall flow rate, and local pressure gradient as a function of imposed global pressure and viscosity ratio. We discuss potential mechanisms leading to this transition, considering local flow rate fluctuations, which we also measure and characterize. In all three cases studied, the porous medium's heterogeneity emerges as a pivotal factor.

RÉSUMÉ EN FRANÇAIS

De nombreuses applications industrielles et environnementales reposent sur une compréhension du comportement des fluides au sein d'un milieu poreux, allant de la remédiation de la contamination des eaux souterraines au stockage du dioxyde de carbone. Les fluides à seuil, qui résistent aux contraintes jusqu'à un certain seuil, présentent à la fois des défis uniques et des opportunités. Les forces capillaires, responsables de la séparation des fluides non miscibles, influencent également de manière significative l'écoulement multiphasique dans les structures poreuses. Cette thèse entreprend une exploration théorique de l'écoulement non linéaire au sein de milieux poreux, dans lesquels ces deux forces contribuent à une rhéologie effective globale en interagissant avec le désordre géométrique à l'échelle des pores. Cette étude examine l'écoulement à l'état stationnaire de blobs de fluide à seuil d'écoulement dans un faisceau de fibres capillaires rempli d'un liquide newtonien, ainsi que l'écoulement d'un seul fluide de Bingham dans un réseau poreux de type arborescent. Nous dérivons des expressions pour le seuil de pression et le débit moyen en fonction de la chute de pression appliquée. Dans les deux cas, la non-linéarité observée découle de l'ouverture séquentielle des chemins d'écoulement avec l'augmentation de la chute de pression. La distribution des seuils de pression liés à ces chemins définit ainsi la loi de débit-pression. Enfin, nous explorons la transition entre un écoulement visqueux et l'apparition de mousse lors du drainage immiscible dans un milieu poreux bidimensionnel. Nous caractérisons cette transition grâce à des simulations numériques utilisant un modèle dynamique de réseau poreux. Nous mesurons la localisation de la transition, le débit global et le gradient de pression local en fonction de la pression globale imposée et du rapport de viscosité. Nous discutons des mécanismes potentiels à l'origine de cette transition, en tenant compte des fluctuations locales du débit, que nous mesurons également et caractérisons. Dans les trois cas étudiés, l'hétérogénéité du milieu poreux émerge comme un facteur déterminant.

PREFACE

This thesis has been submitted to Université Paris-Saclay (UPS) and to the Norwegian University of Science and Technology (NTNU) as a partial requirement for the degree of Doctor of Philosophy (Ph.D.), in the framework of a joint international supervision ("cotutelle"). The research presented in this work was primarily carried out at both Laboratoire de Physique Théorique et Modèles Statistiques (LPTMS) and at PoreLab – Centre of Excellence, under the supervision of Alberto Rosso and Alex Hansen and the co-supervision of Laurent Talon. This thesis will be defended at the Norwegian University of Science and Technology, Trondheim, Norway.

Financial support for this Ph.D. research was mainly provided by "Investissements d'Avenir du LabEx" PALM (ANR-10-LABX-0039-PALM). This work was also supported by the Research Council of Norway through its Center of Excellence funding scheme, project number 262644. Further support, also from the Research Council of Norway, was provided through its INTPART program, project number 309139.

The main objective of the present work is to study both the flow of yield stress fluids and the flow of two immiscible phases in porous media, from a theoretical point of view.

The published articles on which the present thesis is based are listed in the following.

- Federico Lanza, Alberto Rosso, Laurent Talon and Alex Hansen. "Non-Newtonian Rheology in a Capillary Tube with Varying Radius". In: *Transp. Porous Med.* 145 (2022), pp. 245–269. DOI: 10.1007/s11242-022-01848-7. URL: `https://doi.org/10.1007/s11242-022-01848-7`.

- Vincenzo Maria Schimmenti, Federico Lanza, Alex Hansen, Silvio Franz, Alberto Rosso, Laurent Talon and Andrea De Luca. "Darcy's law of yield stress fluids on a treelike network". In: *Phys. Rev. E* 108 (2023), L023102. DOI: 10.1103/PhysRevE.108.L023102. URL: `https://link.aps.org/doi/10.1103/PhysRevE.108.L023102`.

The articles to be published, currently under peer-review, on which the present thesis is based are listed in the following.

- Federico Lanza, Santanu Sinha, Alex Hansen, Alberto Rosso and Laurent Talon. "Transition from viscous fingers to foam during drainage in heteroge-

neous porous media". ArXiv preprint (2023). DOI: 10.48550/arXiv.2307.13451. URL: https://arxiv.org/abs/2307.13451.

This thesis was inspired by the material present in the listed articles, including text, equations and figures. A proper rearrangement of this material was done as long as it was functional for giving more clarity to the document and conveying a general but unitary message coherent to the objective of the present work, without changing or distorting the content. The style of this document was also unified, including symbols and abbreviations. This was done also to match the criteria required by both the universities for the thesis evaluation. In particular, UPS demands the production of a unified monography. On the other hand, NTNU gives the freedom to opt for either a paper-based document or a monography, although the first modality is frequently chosen.

ACKNOWLEDGEMENTS

This work represent the final step of a journey of three years through my doctoral program in cotutelle between Université Paris-Saclay, in France, and NTNU, in Norway. The list of people I've met in both countries, both in and outside the laboratories, is incredibly long; nevertheless, I'm grateful for all the nice moments I shared with each of them.

First of all, I would like to express my deep gratitude to my supervisors Alberto Rosso and Alex Hansen for giving me the opportunity to embark on this experience and get a taste of what it means to do science as a job. I'm grateful they guided me this far throughout my PhD, their suggestions and counseling were helpful and supportive to me.

A big thanks goes to my co-supervisor Laurent Talon, who gave me a precious help for the most part of my work, providing an answer to literally all my questions and concerns. He was always available for enjoyable scientific discussions and suggestions, which were always insightful and, at the same time, conducted in a friendly way.

A particular acknowledgment goes also to Santanu Sinha, who provide me a valuable help with scientific exchanges and technical suggestions, always in a handy and informal way, making himself available every time I needed.

I thank all the members of both my laboratories, the LPTMS in Orsay and the PoreLab in Trondheim, that I've met during these three years. I thank the administrative heads of the labs, respectively Claudine and Marie-Laure, for they efficient assistance in many practical aspects.

Among the people from PoreLab, I want to thank all the students I had the pleasure to meet (Ailo, Andreas, Astrid, Eivind, Håkon, Hursanay, Hyejeong, Ilaria, Kim, Marlo, Michael, Olav, Sebastian) for scientific, and not, discussions, and relaxing chitchats during coffe break. I thank Håkon and Hursanay for the fruitful conversations during our weekly meeting with our common supervisor Alex. A special thanks goes to Andreas, which I had the great pleasure of co-supervising. His passion and enthusiasm were inspiring for me, and I'm glad we also shared nice moments of fun.

Moving to LPTMS, I want to thank all the student and Postdocs (Ana, Andrea, Benjamin, Charbel, Enrico, Fabian, Francesco, Flavio, Gabriel, Jules, Lara, Lenart, Li, Lorenzo, Louis, Mauro, Marco, Matteo, Nadia, Sap, Saverio, Valerio, Vincenzo) for the light-hearted moments of jokes and fun, also outside the laboratory. Especially the first year, during the times of restrictions due to the pandemic, the laboratory has become a fundamental meeting and social point. I thank my former flatmate and friend Vincenzo, whose jolliness and folly made my days at

work, at home, and around Paris, brighter; I thank him also for the scienfitic help he provided me. Thanks to Sap, the best mentor that a laboratory can have, and for having been a faithful friend. Thanks to my officemate and friend Enrico, for all the passionate discussions.
Outside the laboratory communities, I would like to thank my former flatmates Michael, Sander and Davide in Trondheim, and Denise in France, for having contributed to a warm environment at home. I want to thank Adamantia, my best friend during my Norwegian experience, for having shared with me joyful conversations, sweets moments and reciprocal support, that definitely helped me getting through my period in Trondheim.
I would like to thank my therapist Beatrice for all the support provided me in these years. Thanks by heart all my friends in Verona, who I have the chance to meet every time I came back to Italy for holidays. In particular, thanks to Vittorio and Fabio for having been great adventure mates. A deep thanks by heart to my old and dearest friends Elisabetta and Piero, who, by pure chance, happened to be by my side in Paris during my very last months of my doctorate, allowing me to end this experience on a high note. The sweetness of Elisabetta warmed my heart and gave me serenity in so many occasions, and the enthusiasm of Piero always cheers me up.
All my gratitude to my family for the tremendous support given to me. My parents were always by my side in all my choices, and I wouldn't be where I am here now without their constant and unwavering love and affection.
And finally, thanks to me. I remember how, before starting, I was intimidated about the idea to live for a long time abroad, where I almost didn't know anyone, and I didn't know what to expect. And now that I'm almost at the end, despite all the difficulties I had to face, I have no doubt in saying that, if I came back in time, I would choose to do it again without thinking twice. I've grown so much both scientifically and as a person, done a lot of amazing experiences, met new friends, and pushed myself where I thought I could never go three years ago. It was a long ride, but it was worth it.

CONTENTS

LIST OF SYMBOLS AND ABBREVIATIONS

List of symbols used in this document in alphabetic order:

Ca_P	Pressure based capillary number
Ca_Q	Flow rate based capillary number
E	Energy of a level in the REM / energy of a directed polymer
k	Consistency index of a Herschel–Bulkley fluid
l	Length of a tube
M	Viscosity ratio
n	Flow index of a Herschel–Bulkley fluid
n^{ch}	Number of channels above the one at minimal pressure in the Cayley tree pore network
n^{ind}	Number of independent channels above the one at minimal pressure
n^{REM}	Number of energy levels above the minimal in the REM
n^{full}	Number of energy levels above the minimal for the directed polymer on the Cayley tree
P_{in}	Pressure at the inlet of a porous medium
P_{out}	Pressure at the outlet of a porous medium
P_γ	Pressure drop given by surface tension
P_{τ_c}	Pressure drop given by yield stress
$\hat{q}$	Overlap between two channels / directed polymers
Q	Volumetric flow rate
r_0	Characteristic radius of a tube
$\hat{\gamma}$	Surface tension between two fluids
ΔP	Pressure drop across a porous medium

ΔP_c Critical pressure drop for a single flowing path in a porous medium (a tube in capillary bundles, a channel in pore networks)

$\Delta P_{\min}$ Critical pressure drop for a porous medium

ΔP^* Effective critical pressure drop for a porous medium

θ Contact angle between the fluid and the solid surface

$\dot{\vartheta}$ Shear rate of a fluid

κ Permeability of a porous medium

Λ Distance from the inlet to the fingering-to-foam transition

μ Viscosity of a Newtonian fluid or a Bingham fluid

Σ Cross-sectional area of a porous medium

τ Shear stress applied to a fluid

τ_c Yield stress of Herschel–Bulkley fluid

List of abbreviations used in this document in alphabetic order:

IPV Injected Pore Volume

KPP Kolmogorov-Petrovsky-Piskuno

PDF Probability Density Function

PNM Pore Network Model

REM Random Energy Model

YSF Yield Stress Fluid

CHAPTER

ONE

INTRODUCTION

Studying the flow of fluids in porous media holds profound significance across a spectrum of scientific, industrial, and environmental contexts. Porous media, characterized by intricate networks of interconnected pores, can be found in diverse natural and engineered systems, ranging from geological formations to biological tissues and industrial filtration units. Understanding the behavior of fluids within these porous structures is essential for several compelling reasons.

The most cited and longstanding example, that historically has given greater impetus to the study of flow in porous media, consists in the exploration of underground resources such as oil and gas. As of 2022, oil and gas represent together about the 56% of the world energy consumption share [1]. For reservoir engineering, comprehending how fluids flow through porous rock formations is relevant for efficient resource extraction and management.

In a world gradually phasing out from fossil fuels, the understanding of fluid flow in porous media continues to be valuable across numerous other fields. A fundamental application arises in the field of environmental science, in particular concerning soil contamination. The majority of the water utilized for human consumption is stored within subterranean formations made of permeable rocks and granular materials, known as aquifers. Understanding how impure water migrate is vital for preventing contamination or remediating already polluted sites, safeguarding the water resources and minimizing the environmental damage.

Another remarkable example consist in the carbon dioxide sequestration, part of the carbon capture and storage (CCS) process aiming to reduce greenhouse gas emissions in the atmosphere and thus mitigate climate change. Once captured, the carbon dioxide is usually conserved in underground geological formations, so knowing the laws governing the gas flow in these porous structure helps in managing the process and preventing leakage [2].

If describing the flow of oil, water and gases is already a challenging task, this challenge becomes even harder when dealing with fluids exhibiting a more complex rheological behavior. Among these, Non-Newtonian fluids with yield stress represent an emblematic case. These fluids behave as solids below a certain critical pressure but transition to a liquid state above it, resulting in highly non-linear flow dynamics. Additionally, when multiple immiscible fluids flow simultaneously, the complexity of the flow further intensifies, due to the capillary forces separating the phases. In both cases, the non-linearity emerges from the interplay between the

disorder in the pores geometry and the forces into play (yield stress and capillary, respectively).
In the last years, accurate models of fluid flow in porous media have started to be developed and refined taking into account the non-linear behaviours that were previously neglected. Modifications to the Darcy law, valid only for Newtonian fluids, were proposed and tested experimentally and numerically, for the flow of yield stress fluids on one hand, and of the immiscible two-phase flow on the other hand. However, a complete characterization of the flow of yield stress fluids in porous media is still missing, especially when combined together with the multi-phase problem. Moreover, the role of the heterogeneity of the material at the pore level in defining the macroscopic flow is yet to be completely understood.
In parallel to this, in the context of two-phase flow, significant progresses were made in the last forty years in characterizing the different geometrical patterns that immiscible fluids may create when they displace each others, redistributing them trough the porous medium. Experiments and simulations confirmed the predictions, and stochastic models able to reproduce them were proposed. Still, the transitions between different distinct patterns has not been properly investigated in some cases. For example, the conditions that allow the transition from a continuous, fingering-like invasion pattern to a discontinuous one remain unclear.
The goal of the present work is to contribute in the investigation of the open questions addressed by both the yield stress and the two-phase problem, in steady and unsteady states. The research conducted in this work encompasses theoretical aspects, consisting in analytical derivation of physical laws, as well as numerical simulations of specific scenarios and their evolution.

This thesis is organized as following.
In Chapter 2 the theory relevant to the current study is presented, illustrating the basic concepts and providing a review of the pertinent knowledge within the current state-of-the-art literature. This includes the physical laws governing the macroscopic steady-state flow, the description of the evolution of the fluids pattern in unsteady-state flow, and the models adopted for both the analytical and numerical studies of the present work.
Chapter 3 illustrates a theoretical study of the flow of a two-phase non-Newtonian flow in a capillary bundle. The study focuses first on the analysis of a single tube, where expressions for the pressure threshold and the average flow rate are analytically derived as a function of the tube geometry, the rheological parameters and the fluids arrangement. Both the capillary and the yield stress forces are shown to be relevant in contributing to the overall threshold and thus in regulating the flow dynamics. The extension to many parallel tubes is then performed, by computing the distribution of the tubes pressure threshold in the limit of many tubes, and deriving then the bundle average flow rate.
In Chapter 4 the problem of a Bingham fluid flowing in a tree-like porous structure is illustrated. This system present a critical pressure over which the flow rate evolves exponentially as a function of the pressure drop, before reaching linearity. This is demonstrated computing the number of channels that opens just above the critical pressure, and showing that they share a low overlap between them, behaving like independent channels. A parallelism is then tracked with the problem of a Bingham flow in independent channels, which is also studied and discussed.

Chapter 5 is dedicated to a numerical investigation of drainage events in a porous medium which exhibit a transition from a continuous invading pattern to a highly discontinuous one, leading to foam formation. Simulations are done in the framework of a dynamic pore network model, whose details are shown. The displacement characteristics, including the transition location and the total flow rate, are studied as a function the pressure drop imposed to the system and the viscosity ratio between the two immiscible fluids. Furthermore, the flow rate at the pore level exhibits fluctuations which are measured depending on the flow regime, and discussed in connection to the foam origin.
Finally, Chapter 6 is devoted to drawing conclusions to the works presented and providing insight into potential future developments of these researches.

CHAPTER

TWO

LITERATURE SURVEY

The purpose of this Chapter is to offer a concise overview of the current body of literature and the main concepts pertinent to the studies carried out in the following Chapters. In Section 2.1 a brief overview of the Darcy law is provided, including its modifications in the context of non-linear flow. Section 2.2 includes insights on the immiscible displacement phenomena, focusing in particular on the description of the patterns created during drainage and foam formation. Finally, Section 2.3 is dedicated to give a summary of the models implemented in the present work for a theoretical study of the porous media.

2.1 Non-linear flow in porous media

One of the primary aspects of characterizing flow within a porous medium is finding a relation between the pressure difference applied at the edges of the system and the total flow rate flowing in it. Within this Section, we demonstrate both the appropriateness of assuming a linear relationship (Subsection 2.1.1), and its shortcomings in certain significant scenarios, including the flow of a yield stress fluid (Subsection 2.1.2) and the flow of two immiscible phases (Subsection 2.1.3). We refer here to the study of steady-state flow [3]. This means that the total flow rate is supposed to not evolve in time, neglecting fluctuations, when imposing a constant pressure drop (and vice versa). In this way, a characteristic law between the total flow rate and the pressure drop can be determined.

2.1.1 Darcy law

The founding act of the study of flow in porous media is traced back to Henry Darcy (1803 - 1858), a French engineer remembered for having designed an realized in the city of Dijon the prototype of the modern aqueduct, consisting in an articulate system of water distribution based on pressurized pipes driven by gravity. From 1855 to 1856, he performed several experiments involving the flow of water in columns filled with sand [4], like the one shown in Figure 2.1.1. In particular, he found a linear relationship between the ratio $\Delta P/L$, where $\Delta P = P_{\text{in}} - P_{\text{out}}$ is the *pressure drop* applied at the edges of the sand column and L the column height, and the *flow rate* Q, namely the volumetric amount of water per time outgoing from the bottom of the column. The constant of proportionality was found to

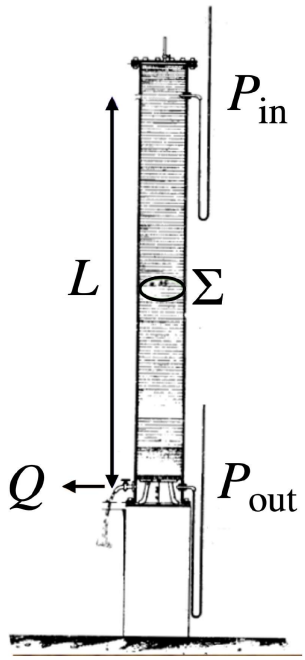

Figure 2.1.1: Sketch of the the experimental setup realized by Darcy. A piston regulates the pressure at the inlet. Water is flowing out from the bottom. (Image taken from [4]).

depend on the cross-sectional area of the column Σ and on the type of sand used. In the subsequent decades, it was discovered that this empirical proportional relationship, initially identified by Darcy only for water, also held true for various other liquids, notably including oil flowing through sandstone. The relationship was then adjusted to incorporate the *viscosity* μ of the fluid in motion, resulting in the derivation of a *permeability* coefficient κ specific of the solid material [5]. This brought to the current formulation of the Darcy law:

$$Q = \frac{\Sigma\,\kappa}{\mu}\frac{\Delta P}{L}. \tag{2.1}$$

Numerous corrections to Eq. (2.1) were suggested later in order to extend its validity to different cases, always with the goal of describing the flow of a fluid (often referred as *phase*) in a porous media.
For example, the Darcy law can be implied to describe the flow of a gas. It was however found that the permeability measured when using a gas is different from when we instead inject a gas in the same porous material, due to the fact that for the gas the slippage close to the solid wall is not negligible. The permeability in Eq. (2.1) needs to be adjusted as proposed in [6] where the authors write $\kappa = \kappa_g/(1 + b_K(P_{\text{in}} + P_{\text{out}})/2)$, κ_g being the permeability measured using the gas and b_K a constant.
Furthermore, Eq. (2.1) holds only for sufficiently low Reynolds numbers, for which the creeping-laminar flow regime holds at the pore level. To keep into account weak inertial effects, corrections were proposed to Eq. (2.1) that include terms

quadratic or cubic in Q [7, 8].
Moreover, a term proportional to the Laplacian of the flow rate $\nabla^2 Q$, derived from the Stokes equation, have to be included when the porous medium is rarefied, namely when $\sqrt{\kappa} \gg L$, with L the characteristic size of the medium [9].
Additionally, we are assuming here that the porosity, namely the fraction of porous non-solid volume in the porous material, is not affected by the fluid flow, such that the permeability remains invariant as well. However, during particle-laden flows, erosion and deposition phenomena can decrease and increase the porosity, respectively, resulting in clogging of pores [10] and in time fluctuations of the permeability [11, 12]. These mechanisms are found to be dependent from the size, concentration and adhesive forces of the particles, as well as changes in the flow paths.
The list of derogations to the Darcy law does not end here, as an enormous number of other variables can be taken into consideration. In the present work, we are in particular interested in two distinct scenarios, for which a significant effort has been put in characterizing the macroscopic flow: (i) when the fluid flowing in the porous material is non-Newtonian, in particular presenting a yield stress (ii) when two (or more) immiscible fluids are coexisting in the porous structure. We will thoroughly examine these two cases in the following two subsections.

2.1.2 Darcy law for yield stress fluids

Non-Newtonian fluids are commonly implied in numerous industrial, geophysical, and biological scenarios involving porous materials. In fact, many fluids exhibit non-linear rheological properties, including substances like gels[13], heavy oils [14], suspensions [15, 16] as well as certain biological fluids such as blood [17, 18]. Our focus here is on yield stress fluids, which necessitate a minimum applied stress to initiate flow. These fluids play crucial roles in various practical applications, including oil extraction processes like fracking, where proppant fluids are injected into the ground [19], or biomedical engineering applications such as the stabilization of fractures and metastatic lesions in cancellous bones [20]
To determine whether a fluid is Newtonian or not, experiments are usually performed in which a shear stress τ is applied to a portion of the fluid under exam, and the shear rate $\dot{\vartheta}$, namely the velocity of shear deformation, induced by the stress is measured. Herschel and Bulkley [21] proposed an equation for modeling non-Newtonian fluids presenting yield stress a power-law between τ e $\dot{\vartheta}$. Assuming $\tau > 0$, it writes

$$\begin{cases} \dot{\vartheta} = 0 & \text{if } \tau < \tau_c \\ \tau = \tau_c + k\,\dot{\vartheta}^n & \text{if } \tau > \tau_c \end{cases} \tag{2.2}$$

where τ_c is the yield stress, k the consistency index and n the flow index. When $\tau \leq \tau_c$, the Herschel-Bulkley fluid behaves like a rigid, non-deformable solid, while the flow is recovered for $\tau > \tau_c$. If $n < 1$ the fluid is defined as shear-thinning (or pseudoplastic), while for $n > 1$ the fluid is shear-thickening (or dilatant). In the special case where $n = 1$ and $\tau_c = 0$, Eq. (2.2) simplifies to that of a Newtonian fluid and k corresponds to its viscosity.
Several investigations [22, 23, 24, 25] have explored the behavior of yield stress fluids within various porous media. It was proven that no flow is observed below

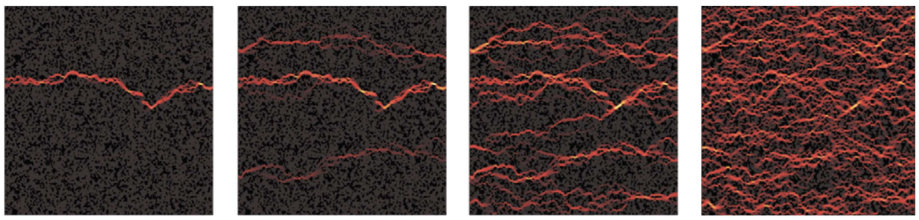

Figure 2.1.2: Numerical simulations of flow of a Bingham fluid in a porous medium. Images from left to right refers to growing values of ΔP. The flowing channels are pictured in red, while black indicates the immobilized part. (Image taken from Fig. 5 of [30]).

a *critical pressure drop* (also called *pressure threshold*) $\Delta P_{\min}$. Flow is recovered only if $\Delta P > \Delta P_{\min}$, but the fluid in the porous medium is not mobilized all at the same time. Due to the heterogeneity of the local porous geometry, some regions are easier to yield than others. In general, for a certain imposed pressure above the minimal, only some channels, namely paths in the porous medium connecting the inlet to the outlet, are flowing, while all the others are still blocked. A gradual increase of ΔP results then in a subsequent opening of new channels, as shown in Figure 2.1.2. This was confirmed by both experiments [26, 27] and numerical simulations [28, 29, 30, 31, 32]. We can then identify three different regimes depending on the value of ΔP:

- When ΔP is close to $\Delta P_{\min}$, fluid is flowing in only one channel, the first one that opens at $\Delta P_{\min}$. In this case, the flow in the porous medium corresponds to the one in a single channel.
- For increased values of ΔP, more and more paths opens. The flow rate as a function of the pressure drop will be then influenced by the increasing number of channels flowing from the inlet to the outlet.
- At a sufficiently high ΔP all channels are open, so the fluid is flowing in all the medium. The porous medium in its entirety can be thought as a single channel whose conductivity is given by its permeability. The relationship between flow rate and the pressure drop is then analogous to the one of a channel.

In general, the relation between ΔP and Q for $Q > 0$ can be written as

$$Q \propto (\Delta P - \Delta P^*)^{\beta}. \tag{2.3}$$

With respect to the Darcy law (2.1), valid for Newtonian fluids, we have introduced an effective pressure threshold ΔP^* and an exponent $\beta > 0$ which in general is different than 1. The values of ΔP^* and β depend on the regime in which the flow is occurring, so essentially on ΔP.
Some studies have considered in particular the flow of a Bingham fluid (or Bingham plastic), consisting in a material that flows like a Newtonian fluid above the critical stress. It can be modeled by Eq. (2.2) if we choose $n = 1$ and a generic $\tau_c > 0$. Numerical simulations in two dimensional pore network models have

proven that, in the regime of subsequent opening channels, Eq. (2.3) holds with $\beta = 2$ [28, 30], a value which seems not to depend on the type of disorder chosen to model the heterogeneity of the pore throats geometry [32]. On the other hand, a theoretical study for a one-dimensional porous medium, consisting in a uniform bundle of channels, showed that the flow curve above the threshold depends very strongly on the kind of distribution of the channels widths [33]. However, both the one and two dimensional cases share the fact that at very high pressures the linear Darcy law (2.1) is recovered, so $\beta = 1$.
We remind that, so far, we have addressed to a condition of low Reynolds numbers, hence inertial effects are not involved in the phenomena discussed. Interestingly, an analogous flow behaviour to the one just illustrated was found tuning the Reynolds number related to the Bingham flow in a disordered porous media [34]. Numerical simulations found that, while in the creeping-laminar regime the flow follows the linear Darcy law, for moderate Reynolds numbers the flow is concentrated in preferential channels due to local viscosity fluctuations. The Darcy law's porous medium permeability is reestablished only for sufficiently high Reynolds numbers.

2.1.3 Darcy law for two-phase flow

Another source of complexity in generalizing the Darcy law, independently from the Newtonian, or not, nature of the fluids, is represented by the presence of two or more immiscible fluids. The study of multi-phase flow in porous media is a longstanding and extensive field [35], and it continues to be the subject of numerous ongoing research efforts. Immiscible fluids coexisting in a porous medium are assumed to never mix during their flow, so we can always refer to their respective phase separately. When two immiscible fluids come into contact, a pressure discontinuity arises at the interface, known as *capillary pressure*, which in general influences the dynamics of the flow.
Despite the system is made of two separate fluids, we consider an approach based on deriving a single Darcy law for the flow of the two-phase system in its entirety. In this regard, the combination of two immiscible phases can be seen as a single, complex fluid [36], from which non-linearity might emerge, even if both fluids are Newtonian. In particular, in the last few years, different experiments [37, 38, 39, 40] and numerical studies [36, 41, 42] have revealed the existence of a non-linear regime for the Newtonian two-phase flow at sufficiently low flow rates. Specifically, due to capillary forces, interfaces can only move when a certain pressure is applied. Within a medium where the pore sizes are distributed in an disordered way, the interface movement is facilitated more in some regions than others. In general, imposing a certain pressure drop on the system, the displacement of interfaces occurs essentially along a limited number of paths from the inlet to the outlet, and this number increases as the applied pressure rises [43]. Hence, like the case of yield stress fluids, heterogeneity controls the flow behaviour.
The flow rate can be then described by a non-linear Darcy equation like Eq. (2.3). In the non-linear regime, the literature mostly seem to agree on $\beta \simeq 2$. This value was measured experimentally [37, 38], numerically [41], and confirmed by an argument based on energy dissipation balance between the viscous and the capillary forces resulted in $\beta = 2$ [37]. A calculation based on mean-field theory, indepen-

dent from the dimension of the porous medium, also found $\beta = 2$ [36]. Significant variations are reported in the range $\beta \in [1.35, 1.49]$ [44] and $\beta \in [1.4, 2.3]$ [40] depending on the fractional flow rate, namely the ratio between the flow rates of the different phases injected. Another remarkable exception is given by the one dimensional capillary tube model, for which β can be either 3/2 or 2 depending on the distribution of the pressure thresholds [45]. Nevertheless, in all cases at sufficiently high pressure the linear regime with $\beta = 1$ is restored.

2.2 Immiscible displacement in two-phase flow

In the context of two-phase flow, beside the characterization of the steady-state, one can try to study unsteady events, for which the physical quantities related to both phases have not reached an equilibrium state, but are changing in time. In particular, during displacement events, it is interesting to see how the spatial distribution of the two different phases evolves in time, in particular looking for characteristic patterns depending on the flow conditions. The distinctive shapes generated by a displacement process vary indeed according to the characteristic forces involved. Here we will restrict the study to the case where only viscosities of the two fluids and capillary forces separating the two phases are present, neglecting for example gravity [46] and wettability changes [47]. Nevertheless, the interplay of the viscous and capillary forces with the heterogeneity in the local porous geometry offers a rich variety of scenarios.
We will define the more- and less-wetting fluids as wetting and non-wetting fluids respectively. When a wetting fluid displaces a non-wetting fluid inside a porous medium, the flow is referred as *drainage*. The opposite case, namely the displacement of a non-wetting fluid carried out by a wetting one is instead defined as *imbibition*. In Subsection 2.2.1 we will focus on the first of these two processes, while in Subsection 2.2.2 we review some literature about foam formation during immiscible displacement.

2.2.1 Displacement patterns during drainage

Suppose we have a porous medium completely filled with a wetting fluid, and from the inlet we inject a non-wetting one. In reaching the outlet, the invading non-wetting phase will displace the defending wetting one. The displacement pattern that forms during the drainage process varies according to the ratio between the forces into play (the two viscous and the capillary). In particular, three scenarios can occur:

- *Capillary fingering.* When the capillary force dominates both the viscous ones, the non-wetting phase enters the porous medium in the form of short paths, of the order of few pores, that tend to ramify and grow isotropically, including towards the inlet [48]. This is due to the disorder in the capillary forces related to the pore size distribution; indeed, their structure can be well modeled by invasion percolation theory [49, 50].

- *Viscous fingering.* If the viscous force related to the wetting phase overcome both the non-wetting viscous force and the capillary one, we have

longer, less ramified paths than the capillary fingers, and their growth occurs mainly through the outlet [51, 52, 53]. Structure of such fingers are strongly analogous to diffusion limited aggregation (DLA) [54], a statistical process that obey Laplacian growth.

- *Stable displacement.* When the viscosity of the non-wetting fluid is much higher than the one of the wetting one, neglecting also capillary forces, we have a stable invading front [55] which is not completely flat but present some roughness at the scale of few pores, and leave behind cluster of wetting fluids still of the order of few pores. This can be modeled by an anti-DLA process [56], or equivalently by diffusion limited annihilation [57].

Lenormand et al. [58] delved into a in-depth examination of the transition between these three regimes resulting from the interplay between viscous and capillary effects, performing quasi-2D experiments and PNM simulations. The authors first introduced two commonly used dimensionless number that are able to fully characterize the displacement pattern: the *capillary number*, expressing the ratio between the viscous forces and the capillary forces, and the *viscosity ratio*, namely the ratio of the two viscosities. A 'phase diagram' for drainage can thus be constructed by charting the ranges where the three distinct mechanisms are valid onto a plane whose axes are defined by the capillary number and the viscosity ratio, like the one shown in Figure 2.2.1. The existence of the same patterns also in three dimensional porous media was confirmed later, both experimentally [60] and numerically [61].
Although the different patterns can be easily recognizable to the naked eye due to their qualitative difference, it is useful to characterize them quantitatively, for example measuring the non-wetting saturation, namely the fraction of total pore volume occupied by the non-wetting fluid, at breakthrough [58]. In the cases of fingering patterns, since they exhibit a fractal structure, it also is possible to quantify their fractal dimension measuring the related Hausdorff dimension D [62]. Considering two-dimensional porous media, for capillary fingering we typically have $D \simeq 1.8$ [48, 63], while a lower value is measured for viscous fingers, around $D \simeq 1.6$ [51, 64].
Up to now, we have assumed both fluids to be Newtonian. An extension of the drainage patterns characterization was done assuming that the defending wetting phase is a Bingham fluid [65]. Beside the capillary number and the the viscosity ratio, the authors introduced the Bingham number, expressing the ratio between the yield stress and the capillary force. Numerical simulations found that for high Bingham numbers a new pattern was found, consisting in a quasi one-dimensional non-wetting finger, corresponding to the minimum threshold path. For low Bingham numbers, the patterns approach those of the corresponding Newtonian displacement. To our knowledge, no further progress has been made in the characterization of immiscible displacements involving yield stress fluids.

2.2.2 Foam formation and mobilization

The patterns illustrated in the previous Section share the common feature that the invading fluid remains connected. However, in various scenarios involving the flow of two phases, it's not unusual for the invading fluid to rupture and become

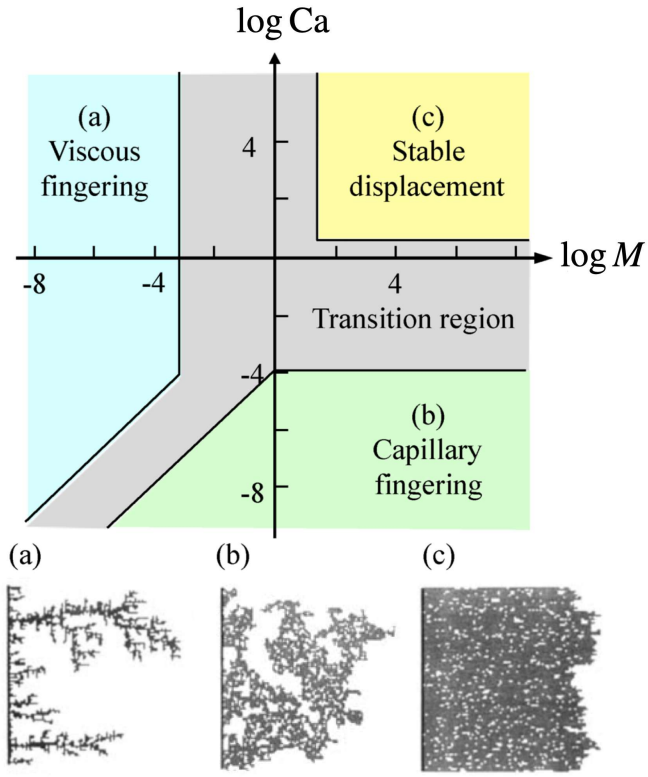

Figure 2.2.1: Phase diagram of the immiscible displacement patterns in porous media. Ca and M refers to capillary number and viscosity ratio, respectively. (Images taken from Fig. 4 of [58] and Fig. 1 of [59])

discontinuous with respect to the other phase. The breakage of the invading phase might lead to formation of *foam*, which here we simply define as the combination of two immiscible fluids in a certain region in a highly discontinuous way, separated from each others by numerous menisci. Within a foam, it is possible to observe many blobs of both phases, which consists in small portions of fluid typically with dimensions on the scale of a pore or even smaller. A small blob of wetting phase is usually called either lens, when their thickness is large enough to remain relatively stable, or lamella, if they are thinner such that they can break more easily. However, from the point of view of the non-wetting fluid, both a lens and a lamella contributes in separating it and blocking the flow through the throat [66]. Due to the presence of numerous menisci exerting capillary pressure drops, the mobility of the porous medium, defined as the ratio between the overall flow rate and the global pressure drop, is expected to be impacted. In literature we often find a distinction between "weak" (or "coarse") and "strong" foam, whether the foam does not impact much the global mobility of the system, or it contributes to significantly reduce it, respectively [67, 68, 69]; note that we don't have a precise criterion to distinguish between the two, being more relative concepts. To measure the loss in mobility due to the presence of foam, one can look at the increase in pressure gradient along the system, averaged over fluctuations in space and time,

when the flow rate injection is imposed [67], or, on the contrary, at the decrease of total flow rate when the pressure drop is imposed [68, 69].
The mechanisms that leads to fragmentation of the fluids within porous material have extensively examined in the last years [70]. In brief, the following processes occurring at the pore level are commonly cited.

- *Roof snap-off.* As the leading tip of the invading fluid moves out of a narrow pore throat, the curvature at the edge decreases, while the curvature inside the throat remains high. This creates a pressure disparity that could lead to a reverse flow of the defending fluid, causing the incoming fluid to rupture [71, 72].

- *Dynamical breakup.* When the tip of a phase encounters a juncture of two pores, the tip might divide to infiltrate both pores, consequently disconnecting the other phase [73]. The same mechanism can happen for lenses and lamellae, which can divide into two when they encounter a branching point. The phenomenon is referred as *lamella (lens) division*, and the new blob created will remain stable depending on its thickness and on the surface tension between the two phases [66, 69].

- *Leave-behind.* In drainage events, lamellae or lenses of wetting phase can be created in pore throats as the invading non-wetting fluid occupies adjacent pore bodies while advancing through continuous paths. Again, they can then break or remain stable, depending also on their thickness [66].

- *Pinch-off.* A continuous fluid filament can break into smaller segments due to the Rayleigh-Plateau instability [74]. Inside a porous medium, this instability can be induced, for example, by a neighbour blob and a solid wall delimiting the filament, or by two neighbouring blobs surrounding it [75].

A schematic sketch for each of the listed mechanism is shown in Figure 2.2.2.
Even if the literature on this subject is extensive, establishing the actual importance and impact of these mechanisms in both the formation and displacement of foam in porous materials remains challenging. For instance, despite it was affirmed that snap-off is a primary mechanism for generating foam [67, 66], rather recent pore network simulations have demonstrated that substantial foam generation can happen without the necessity of the Roof snap-off mechanism [29, 76]. Moreover, once strong foam is created, it seems that the details of the generation of new lenses or lamellae become less important, as the stability of foam is governed by more global factors, like the permeability of the porous medium or the presence of surfactants that regulate the surface tension [69]. Nevertheless, both experiments and simulations agrees on the fact that a minimum pressure gradient, or equivalently a minimum flow rate, is require to initiate foam on the system and sustain it [67, 66, 77, 69, 76, 78].

2.3 Modeling the porous media

A theoretical study of the flow in a porous medium necessarily requires a model of the porous medium itself. In this Section we introduce the main aspects of the

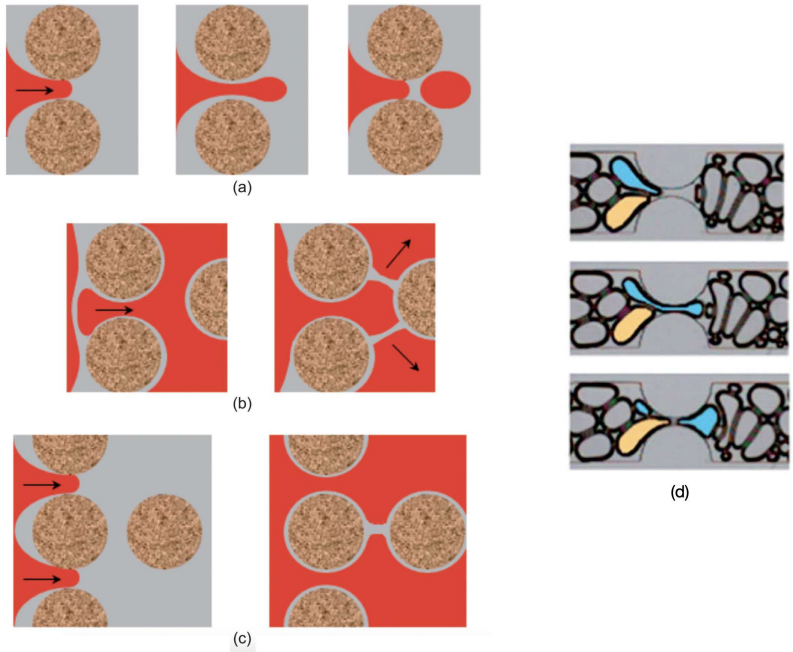

Figure 2.2.2: Schematic drawings of (a) Roof snap-off, (b) lamella (lens) division, (c) leave-behind and (d) pinch-off. For the figures (a)-(c), the wetting and non-wetting phase are coloured in grey and red respectively. For figure (d), the two (non-wetting) blobs involved in the mechanism are depicted in blue and yellow (Images taken from Fig. 1 and Fig. 5 of [75])

models implied in the present work: the capillary tube bundle model (Subsection 2.3.1), adopted in Chapter 3, and the pore network model (Subsection 2.3.2), implemented in the studies of both Chapter 4 and Chapter 5. Both models share the common feature that they are able to describe the flow at the Darcy scale (or meso-scale), namely at the scale of a porous sample for which the Darcy law can be considered valid, so much larger than the scale of a single pore in it. These models imply a strong simplification of the pore geometry, so they are not able to describe in detail the fluids arrangement inside a pore. However, they allow for studying the flow behaviour at much larger scale, deriving it analytically when possible, or calculating it at a reasonable computational cost, in case of numerical studies. This includes the possibility to look for statistical properties of the flow. Other modeling methods, not considered here, have been successfully implied for the study of the macroscopic flow in porous media, including the finite volume methods [79] and the Lattice Boltzmann methods [30], both based on a discretization of the porous medium.

2.3.1 Capillary bundle model

With capillary bundle (or tube bundle) we refer to an array of several capillary tubes which are parallel, namely they do not intersect each other [80, 81]. This

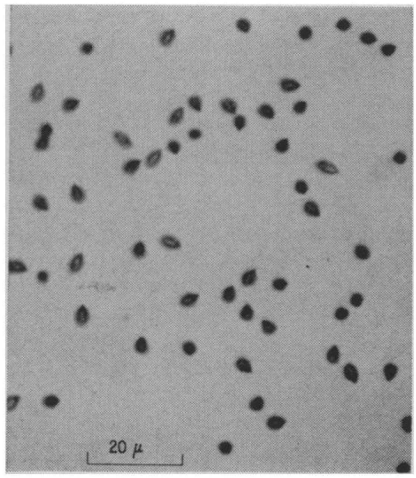

Figure 2.3.1: Picture of a sample of cellulose nitrate, on whose surface the tracks left by fission fragments are visible as black dots. (Image taken from Fig. 2 of [82])

can be seen as a model of 1D porous media, in which the flow occurs along only one preferential direction. An example of these materials consists in Nuclepore filters (see Fig. 2.3.1), namely membranes of polycarbonates or other plastics in which cylindrical pores of diameter in the range between 1 nm to a few μm are created through irradiation with heavily ionizing particles and dissolution of the nuclear trails by certain chemicals [82].

Studies of the flow in generic porous substances, where the fluid paths can intersect each other, adopting the capillary tube bundle model, are still possible in certain extents. For example, the Darcy law for Newtonian fluids can be derived modeling the material as a bundle of effective capillaries, whose length can be extrapolated experimentally by a characterization of the sample, finding expressions for the permeability as a function of the porosity and the cross-sectional area [83, 84]. However, the fact that the flow can occur only in one direction, since the different channels don't cross each others, constitutes the major limit of the model.

Nevertheless, the relevance of the capillary tube bundle model relies on the fact that it is a model for immiscible flow which is analytically tractable [45], namely for which it is possible to derive analytically flow dynamics relations, starting from some assumptions on the tubes geometry and on the rheological properties of the fluids. The simplest choice for the tube shape would consist in taking perfectly cylindrical tubes, for which analytical expressions are already known for the flow of both Newtonian and non-Newtonian fluids. However, to take into account heterogeneity in the model, one can introduce variations in the geometry, for example

Figure 2.3.2: Left: sketch of a porous medium characterized by a solid structure, formed by a collection of grains (depicted in black), within which the fluid can move. Right: Drawing of a pore network, composed by large spherical pore bodies connected by narrow cylindrical throats of variable radius. (Image taken from Fig. 1 of [32])

modifying the value of the radius along each tube according to some function [85, 45, 86], or varying the characteristic radius between different tubes [33], generating the values randomly from a certain probability distribution.

2.3.2 Pore Network Model

The Pore Network Model (PNM) was first introduced in the 50s [87], and is by far the most common model implied for meso-scale numerical simulations. Essentially, the model consist in a collection of large voids, the pores bodies, connected by narrow tubes, the pore throats, as shown in Fig. 2.3.2. The arrangement of those elements follows the structure provided by a network, where the bodies and the throats corresponds to the nodes and the links of the the network, respectively. The volume of the pore bodies is significantly larger than the one of the throats such that the pressure inside it can be considered constant, so we can associate an unique value of pressure to each node.

In general it is possible, from a sample of a porous material, to reconstruct the corresponding pore network combining imaging techniques with ad-hoc algorithms for modeling the pore bodies and throats [88]. Nevertheless, two or three dimensional regular lattices with fixed connectivity are commonly implied in numerical studies, especially when we are interested in statistical properties which are not sample-dependent. The connectivity and the dimensionality of the porous model correspond then to those of the underlying network.

Each body and throat present a simplified geometry, such that we can implement already known equations for describing the flow across them. Heterogeneity is then included in the model varying randomly all or some of the geometrical parameters characterizing the porous elements. For example, it is possible to model the pore throats as cylinders where the length is kept the same, while the radius varies according to some probability distribution [58, 32].

In general, the resolution of the equations for the flow at the pore level allows to find the values of the pressure drops between the nodes of distinct pores, which in turn regulate the displacement of the fluids between them. In the context of two-phase flow, fluid displacement occurs following precise algorithms. In this extent, pore network models can be divided into quasi-static models and dynamic

models. In the *quasi-static* models, fluid displacement is carried out by sequentially filling individual pores using invasion percolation-like algorithms. This can be done when the flow is dominated by a force, like capillary [54, 89, 48] or yield stress [65], and the dynamic effects given by the viscosity are neglected, such that the system is considered to undergo in subsequent equilibrium states, corresponding to the subsequent filling steps. The decision to fill specific pores is based on their entry pressures, or, in case of capillary-dominant systems, by evaluating the stability of a meniscus with respect to a given contact angle [90]. The success of these models relies on the dominance on one force on the others, so they generally fail in describing system in which different forces, including viscous, regulates the flow at pore level. This is taken into account in *dynamic* pore network models [91]. The invasion at the pore scale is still determined by the capillary pressure (or the yield stress, if present), but now the time rate of the invasion is given also by the local viscous pressure drop. The local flow rate between different pores is then computed as a function of all the forces into play, and the fluid displacement between that pores will occur according to it.
The equations for the local flow rates must be coupled with other equation expressing the conservation of the mass and the momentum in the pores. In case of incompressible fluids, this condition can be expressed by an equivalent of the Kirchhoff law for the electrical current, which, for a pore labeled by i, can be written

$$\sum_{j \in \mathrm{ngb}(i)} Q_{ij} = 0 \,, \tag{2.4}$$

where j labels all the pores that are nearest neighbours of i, and Q_{ij} is the flow rate from pore i to pore j. The solution for both the local pressure drops and flow rates can be found solving the system formed by the local flow rate equation for all pore throats and the Kirchhoff condition (2.4) for all pore nodes.
Regulating the displacement of the fluids in dynamic pore network models constitutes a significant challenge, since efficient algorithms have to be implemented for the redistribution of the fluids in the different pores, in particular when one or more fluids invade a pore coming from the neighbour ones. Significant progress in this sense was made when algorithms able to track the position of the menisci separating the different phases were introduced [92]. In models implementing these algorithms, the configuration of the fluids inside the pores can be reconstructed explicitly by the positions of all the menisci along the pore throats.
In a recent work [93], a set of meniscus-tracking algorithms for dynamic pore network model was presented, where detailed rules about the redistribution of the fluids were illustrated, allowing for the formation of both continuous paths and separated blobs. These algorithms are able to reproduce well-established results for both drainage displacement and steady-state flow for systems made of two immiscible Newtonian fluids. The numerical simulations of the work presented in Chapter were performed adopting a dynamical pore network model implementing the algorithms set from [93].

CHAPTER

THREE

TWO-PHASE NON-NEWTONIAN FLOW IN CAPILLARY TUBES

In this Chapter, we characterize the flow dynamics of a bundle of identical parallel tubes filled with a Newtonian fluid, and in which blobs of immiscible non-Newtonian fluid presenting yield stress are randomly injected. As discussed in Section 2.3.1, the capillary bundle can be seen as a model of a porous medium, where analytical calculations are possible. In a recent work an analogous system was studied, although in the fully Newtonian case, where Newtonian blobs were randomly injected in each tube [45]. There, it was found that the behaviour of the flow rate averaged over the tubes versus the pressure drop applied depends in general on the probability distribution for the critical pressure, namely the probability density that a tube present a certain critical pressure. This means the disorder in the threshold distribution controls the effective flow properties. An analogous conclusion was reached in another study of the flow in a capillary bundle, in this case in presence of only a Bingham fluid [33].
However, in [45] the relation between the fluid configurations in the tubes and the respective threshold distributions was not discussed, as the distributions were imposed on the system. Here we try instead to derive the critical pressure distribution from both the geometry of the tubes and the rheological properties of the fluids; moreover, we extend the study to blobs of non-Newtonian Herschel-Bulkley fluid, which appears to be novel.
We assume here that both fluids are always immiscible and incompressible. We also assume that the contact angle between the meniscus separating the two phases and the link wall does not vary during the motion of the blobs.
In deriving and illustrating our results, we adopt a bottom-up approach, starting from simpler models and then, in some extent, combining them together. In Section 3.1 we first study the model of one blob flowing in a single tube; then, always dealing with one tube, in Section 3.1 we introduce multiple blobs; finally, the extension of the study to many identical tubes is carried out in Section 3.3. For all of these intermediate models, we analytically derive expressions for threshold pressure drop and the flow rate versus applied pressure drop.

In general for a single tube, we find a critical pressure threshold ΔP_c below which there is no flow. Above this threshold, the flow Q is in general non-linear

and grows with a characteristic exponent:

$$Q(\Delta P) \propto (\Delta P - \Delta P_c)^{\beta}. \tag{3.1}$$

If we have a single non-Newtonian blob in the tube, for a tube of uniform radius r_0, the value of the threshold is $\Delta P_c = P_{\tau_c} = 2\tau_c \Delta x_b / r_0$, where τ_c is the yield stress of the non-Newtonian blob of size Δx_b. For a non-uniform tube of radius $r(x) = r_0/(1 + af(x/r_0))$, ΔP_c is modified

$$\Delta P_c = P_{\tau_c} + P_t, \tag{3.2}$$

where the value of P_t depends on the geometry of the tube, and can be written in general

$$P_t = a \max_{0<x<l} \left[P_{\tau_c} f\left(\frac{x}{r_0}\right) + P_\sigma \frac{\Delta x_b}{r_0} P_{\tau_c} f'\left(\frac{x}{r_0}\right) \right], \tag{3.3}$$

where P_σ is the contribution of the surface tension, and l is the length of the tube. The exponent β in Eq. (3.1) depends on both the rheology and the geometry of the tube.

When having different blobs in a tube, in the case of a uniform radius, the value of the threshold coincides with the one of a single blob with the same amount of fluid, so the flow curve is identical as for the single blob. If instead the tube is non-uniform tube, the value ΔP_c depends explicitly on the number of blobs and their relative distance. Assuming that the blobs are identical and evenly distributed, we show that ΔP_c can be written as

$$\Delta P_c = N P_{\tau_c} + \sqrt{N} A P_t, \tag{3.4}$$

where A is a non-dimensional positive random variable of order 1. Similarly to the one blob case, the power-law regulating the flow rate relies on both the rheology and the geometry of the tube.

For a tube bundle model, in the limit of many tubes the total flow curve results from averaging all the blobs position configurations. In general we have

$$\overline{Q(\Delta P)} \propto (\Delta P - \Delta P_{\min})^{\beta} \quad \text{for } \Delta P \to \Delta P^{+}_{\min}, \tag{3.5}$$

where $\Delta P_{\min} = N P_{\tau_c}$ and the overline stands for an average over all blobs configurations. The exponent β can be computed from $\Pi(A)$, the probability distribution for A, which depends on the tube shape. We studied the following particular cases:

- Sinusoidal deformation, $f(x/r_0) = \cos(2\pi x)/l$. We found an explicit formula for $\Pi(A)$, valid in the limit of many blobs

$$\Pi(A) = 2Ae^{-A^2}. \tag{3.6}$$

- Triangular deformation, $f(x/r_0) = (4r_0/l)\,|x/r_0 - l/(2r_0)| - 1$. We don't have an explicit formula for $\Pi(A)$, but we show how $\Pi(A)$ vanishes when $A \to 0$, in two limiting cases:

  1. Newtonian fluid:

$$\Pi(A \to 0) \propto \frac{1}{A^3} e^{-\frac{k}{A^2}}, \tag{3.7}$$

  where k is a numerical constant.

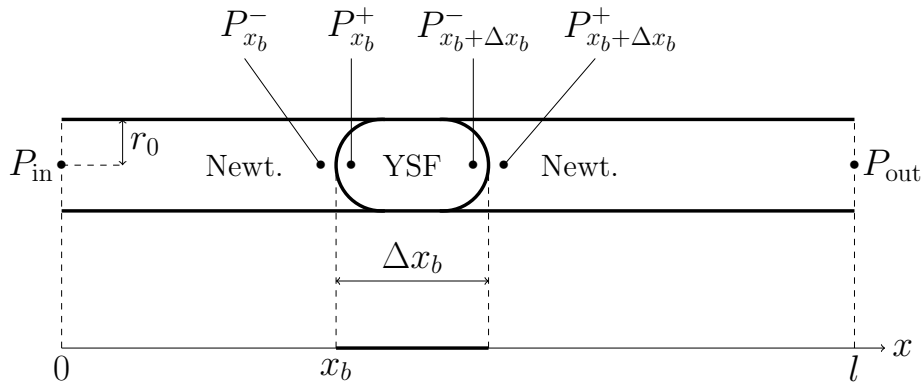

Figure 3.1.1: Two-dimensional sketch of a blob of yield stress fluid in a uniform tube. On the x-axis, the one-dimensional model relative to the problem is pictured, where the thick line is the projection along x of the yield stress blob, while the thin line represent the part occupied by the Newtonian fluid.

2. Non-Newtonian fluid neglecting capillary effects:

$$\Pi(A \to 0) \propto \frac{1}{A^{5/3}} e^{-\frac{k^*}{A^{2/3}}}, \tag{3.8}$$

where k^* is another numerical constant.

The PDFs found for A in those specific cases are confirmed by numerical simulations.

3.1 Model for a single blob in a tube

3.1.1 Constant radius

Let's consider the case of an uniform tube, namely a cylindrical tube with constant radius r_0. For a perfect cylindrical tube completely filled with a non-Newtonian yield stress fluid described by the Herschel-Bulkley relation, the critical pressure drop is $\Delta P_c = 2\tau_c l/r_0$ and the flow rate law [94]:

$$Q(\Delta P) = \begin{cases} C_0\, r_0^{4+\frac{1}{n}} \left(\frac{\Delta P - \Delta P_c}{l}\right)^{\frac{1}{n}+1} & \text{if } \Delta P \to \Delta P_c^+, \\ \\ C_\infty\, r_0^{3+\frac{1}{n}} \left(\frac{\Delta P - \Delta \widetilde{P}_c}{l}\right)^{\frac{1}{n}} & \text{if } \Delta P \gg \Delta P_c, \end{cases} \tag{3.9}$$

where $C_0 = n\pi/((n+1)2^{1+1/n}k^{1/n}\tau_c)$, $C_\infty = n\pi/((3n+1)(2k)^{1/n})$ and $\Delta\widetilde{P}_c = ((3n+1)/(2n+1))\Delta P_c$.
We consider now the case of a tube filled with a Newtonian liquid, in which one blob of yield stress fluid (YSF) of size Δx_b is injected at a certain position x_b, as pictured in Figure 3.1.1. The total pressure drop ΔP needed to sustain a flow rate Q can be expressed as the sum of the pressure drops across every portion of fluid. We call $P^-_{x_b}$ and $P^+_{x_b}$, respectively, the pressure value just before and just after

the left surface separating the Newtonian fluid from the blob (positioned at x_b), while $P^-_{x_b+\Delta x_b}$ and $P^+_{x_b+\Delta x_b}$ will be, respectively, the pressure just before and just after the right surface (positioned at $x_b + \Delta x_b$). The pressure drops across both portions of Newtonian fluid, in the intervals $0 < x < x_b$ and $x_b + \Delta x_b < x < l$, are given by the Poiseuille law

$$\begin{aligned} P_{\text{in}} - P^-_{x_b} &= Q\frac{8\mu x_b}{\pi r_0^4}, \\ P^+_{x_b+\Delta x_b} - P_{\text{out}} &= Q\,\frac{8\mu(l - x_b - \Delta x_b)}{\pi r_0^4}. \end{aligned} \tag{3.10}$$

The pressure drop across the blob is instead given by Equation (3.9) and writes

$$P^+_{x_b} - P^-_{x_b+\Delta x_b} = \begin{cases} \left(\frac{Q}{C_0\, r_0^{4+\frac{1}{n}}}\right)^{\frac{n}{n+1}} \Delta x_b + \Delta P_c & \text{if } \Delta P \to \Delta P_c^+, \\ Q^n \frac{\Delta x_b}{C_\infty^n r_0^{3n+1}} + \Delta \widetilde{P}_c & \text{if } \Delta P \gg \Delta P_c. \end{cases} \tag{3.11}$$

where now $\Delta P = P_{\tau_c} = 2\tau_c \Delta x_b / r_0$.
The capillary pressure discontinuity across the two interfaces are given by the Young-Laplace law, namely $P^-_{x_b} - P^+_{x_b} = -2\gamma/r_0$ and $P^-_{x_b+\Delta x_b} - P^+_{x_b+\Delta x_b} = 2\gamma/r_0$ respectively; here $\gamma = \hat{\gamma}\cos\theta$, being the surface tension between the two fluids and θ the contact angle. The two pressure discontinuities are equal in modulus but opposite in sign, as the interfaces are identical but have opposite curvature. As a consequence, in a perfect cylindrical tube, the total capillary pressure across the two interfaces of a blob cancels out.
The sum of the three pressure drops given in equations (3.10) and (3.11) in the limit $\Delta P \to \Delta P_c^+$ is then

$$\Delta P = Q\frac{8\mu(l - \Delta x_b)}{\pi r_0^4} + Q^{\frac{n}{n+1}} \frac{\Delta x_b}{C_0^{\frac{n}{n+1}} r_0^{\frac{4n+1}{n+1}}} + \Delta P_c. \tag{3.12}$$

In this limit the flow vanishes to 0, so we can neglect the linear term in equation (3.12) as $n/(n+1) < 1 \;\forall\; n > 0$.
In the opposite limit $\Delta P \gg \Delta P_c$ we have

$$\Delta P = Q\frac{8\mu(l - \Delta x_b)}{\pi r_0^4} + Q^n \frac{\Delta x_b}{C_\infty^n r_0^{3n+1}} + \Delta \widetilde{P}_c. \tag{3.13}$$

Since now $Q \to \infty$, we should distinguish between a shear-thinning fluid and a shear-thickening fluid, for which $n < 1$ and $n > 1$ respectively. In the first case, the leading term is the one proportional to Q^n, while in the other case the leading term is the linear one. Finally, we can write the volumetric flow rate in the two different limits:

$$Q(\Delta P) = \begin{cases} C_0\, r_0^{4+\frac{1}{n}} \left(\frac{\Delta P - \Delta P_c}{\Delta x_b}\right)^{1+\frac{1}{n}} & \text{if } Q \to 0 \\ \begin{cases} C_\infty r_0^{3+\frac{1}{n}} \left(\frac{\Delta P - \Delta \widetilde{P}_c}{\Delta x_b}\right)^{\frac{1}{n}} & \text{if } n < 1 \\ \frac{\pi r_0^4}{8\mu} \frac{\Delta P - \Delta \widetilde{P}_c}{l - \Delta x_b} & \text{if } n > 1 \end{cases} & \text{if } Q \to +\infty \end{cases} \tag{3.14}$$

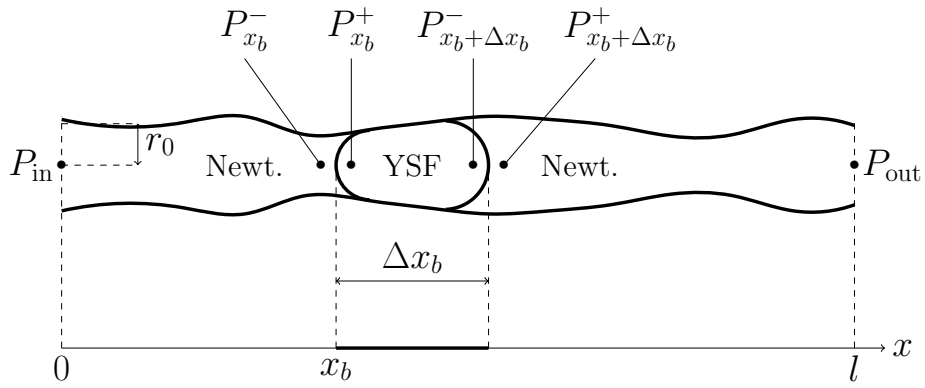

Figure 3.1.2: Two-dimensional sketch of a blob of yield stress fluid in a non-uniform tube. On the x-axis, the one-dimensional model relative to the problem is pictured, where the thick line is the projection along x of the yield stress blob, while the thin line represent the part occupied by the Newtonian fluid.

3.1.2 Generic analytical radius variability

We consider now a tube still of length l, but with varying radius $r(x)$ (see figure 3.1.2) described by the following equation

$$r(x) = \frac{r_0}{1 + af(x/r_0)}, \tag{3.15}$$

where $a \ll 1$ is a dimensionless constant, while $f(x/r_0)$ is a bounded function with zero average in the interval $x/r_0 \in [0, l/r_0]$ and periodic in l, namely $f((x+l)/r_0) = f(x/r_0)$. This periodicity can describe two different situations: (i) a tube of length l with periodic boundary conditions (ii) a tube of length $L \gg l$ presenting a periodic deformation of spatial period l. In the latter case, the blob can in general be located on different periods, but it is convenient to shift its position in the first period: more precisely, if the blob is located at a certain position in the k-th period, the dynamics of the system does not change if we subtract the quantity $(k-1)l$ from that position.

We assume that the radius varies slowly enough, namely $f' \ll 1$ in all the interval. In this way, the lubrication approximation can be applied, allowing to neglect the radial component of the fluid velocity with respect to the axial component. Also, the size of the blob Δx_b can also be considered constant along the tube.

In this Section we assume $f(x/r_0)$ to be analytic in $x \in [0, l]$. Two modifications should be included with respect to the case of the tube with constant radius. First, the capillary pressure across the blob interfaces do not cancel anymore. Since $P^-_{x_b} - P^+_{x_b} = 2\gamma/r(x_b)$ and $P^+_{x_b+\Delta x_b} - P^-_{x_b+\Delta x_b} = 2\gamma/r(x_b + \Delta x_b)$, their difference is in general non zero and approximately equal to

$$\frac{2\gamma}{r(x_b)} - \frac{2\gamma}{r(x_b + \Delta x_b)} \simeq a\frac{P_\gamma \Delta x_b}{r_0} f'(x_b/r_0), \tag{3.16}$$

with $P_\gamma = 2\gamma/r_0$ and $f'(x_b/r_0)$ the derivative of f at x_b. Secondly, as $r(x)$ is non-constant, both Poiseuille law and Eq. (3.9) can be considered valid only

along infinitesimal intervals of length dx. For both reasons, the flow rate varies in time as a function of the blob location x_b. The Poiseuille equation becomes $Q(x_b) = -\pi r(x)^4 (dP/dx)/(8\mu)$ from which, integrating along both portions of Newtonian fluids, at the first order of a we get:

$$P_{\text{in}} - P^-_{x_b} = Q(x_b)\,\frac{8\mu}{\pi r_0^4}\left(x_b + 4a\int_0^{x_b} f(x/r_0)dx\right), \tag{3.17}$$

$$P^+_{x_b+\Delta x_b} - P_{\text{out}} = Q(x_b)\,\frac{8\mu}{\pi r_0^4}\left(l - x_b - \Delta x_b + 4a\int_{x_b+\Delta x_b}^{l} f(x/r_0)dx\right) \tag{3.18}$$

Considering the limit $\Delta P \to \Delta P_c^+$, eq. (3.9) becomes instead $Q(x_b) = C_0\, r(x)^{4+\frac{1}{n}}\,(dP/dx - 2\tau_c/r(x))^{\frac{1}{n}+1}$, which, integrated along the blob interval, gives:

$$P^+_{x_b} - P^-_{x_b+\Delta x_b} \simeq \left(\frac{Q(x_b)}{C_0\, r_0^{4+\frac{1}{n}}}\right)^{\frac{n}{n+1}} \Delta x_b + P_{\tau_c}\left[1 + a f(x_b/r_0)\right], \tag{3.19}$$

where $P_{\tau_c} = 2\tau\Delta x_b/r_0$. Note that we approximated the following integral

$$\int_{x_b}^{x_b+\Delta x_b} \frac{1}{r^{\frac{4n+1}{n+1}}(x)}dx \simeq \frac{1}{r_0^{\frac{4n+1}{n+1}}}\Delta x_b, \tag{3.20}$$

because the correction only affects the prefactor of the flow curve, and not the exponent or the threshold. Since in this limit $Q(x_b) \ll 1$, the leading behavior of the flow curve can be written as:

$$Q(x_b) \simeq C_0\, r_0^{4+\frac{1}{n}} \left[\frac{\Delta P - \Gamma(x_b/r_0)}{\Delta x_b}\right]^{1+\frac{1}{n}}, \tag{3.21}$$

where we have defined the function

$$\begin{aligned}\Gamma(x_b/r_0) &= P_{\tau_c} + a\left[P_{\tau_c} f(x_b/r_0) + P_\gamma \frac{\Delta x_b}{r_0} f'(x_b/r_0)\right]. \\ &= P_{\tau_c}\left\{1 + a\left[f(x_b/r_0) + \frac{\gamma}{r_0\tau_c} f'(x_b/r_0)\right]\right\}\end{aligned} \tag{3.22}$$

The blob position moves as $dx_b/dt = Q/(\pi r_0^2)$, hence from eq. (3.21) we get the equation of motion

$$\frac{dx_b}{dt} = \frac{C_0\, r_0^{2+\frac{1}{n}}}{\pi \Delta x_b^{1+\frac{1}{n}}}\left[\Delta P - \Gamma(x_b/r_0)\right]^{1+\frac{1}{n}}. \tag{3.23}$$

From eq. (3.23), we can see that the condition for the blob to move along a tube period in a finite time is that the pressure imposed is bigger than the maximum of $\Gamma(x_b)$, namely $\Delta P > \max_{0<x_b<l}\Gamma(x_b/r_0)$. On the contrary, the blob is either completely stopped if $\Delta P < \min_{0<x_b<l}\Gamma(x_b/r_0)$, or it moves in general if $\min_{0<x_b<l} < \Delta P < \max_{0<x_b<l}\Gamma(x_b/r_0)$ but the time needed for the blob to complete a period diverges to infinite. So, in a deformed tube, the critical pressure

drop ΔP_c above which flow along a tube period is possible has increased with respect to the cylindrical tube, and is equal to the maximum of $\Gamma(x_b)$:

$$\Delta P_c = P_{\tau_c}\left\{1 + a \max_{0<x_b<l}\left[f(x_b/r_0) + \frac{\gamma}{\tau_c r_0} f'(x_b/r_0)\right]\right\}. \tag{3.24}$$

We denote with x_m the position of such maximum along the tube. Three terms contribute to the pressure threshold. The first one, constant, is due to the yield stress threshold. The second is also due to the yield stress, but depends on the tube shape. The last one, related to the capillary force, is based on the derivative of f. The competition between the last two terms is then governed by the ratio between the relative derivative f/f' and the dimensionless number $P_\gamma \Delta x_b/(P_\tau r_0) = \gamma/(\tau r_0)$.
The time T needed for the blob to move from one end of the tube to the other can be computed from (3.23):

$$T = \int_0^T dt = \int_0^l \frac{dx_b}{dx_b/dt} \propto \int_0^l \frac{dx_b}{[\Delta P - \Gamma(x_b/r_0)]^{1+\frac{1}{n}}}. \tag{3.25}$$

In general $\Gamma(x_b/r_0)$ relies on the specific form of $f(x_b/r_0)$. However, supposing that $f(x_b/r_0)$ is analytical, we can expand $\Gamma(x_b/r_0)$ around x_m: $\Gamma(x_b/r_0) = \Delta P_c - \alpha(x_b - x_m)^2 + \dots$
For $\Delta P \to \Delta P_c^+$, the dominant contribution to the integral of eq. (3.25) is around x_m, so we can write

$$T \propto \int_0^l \frac{dx_b}{[\Delta P - \Delta P_c + \alpha(x_b - x_m)^2]^{1+\frac{1}{n}}} \propto (\Delta P - \Delta P_c)^{-\left(\frac{1}{n}+\frac{1}{2}\right)}. \tag{3.26}$$

The flow rate averaged over the time T, $\langle Q\rangle_T$, is then

$$\langle Q\rangle_T = \frac{\pi r_0^2 l}{T} \propto (\Delta P - \Delta P_c)^{\frac{1}{n}+\frac{1}{2}}. \tag{3.27}$$

Note that, close to the yield threshold ΔP_c, the power-law exponent $1/n + 1/2$ of the flow rate turns out to be different from $1 + 1/n$ in eq. (3.14) for the uniform tube.
On the other hand, in the opposite limit $\Delta P \gg \Delta P_c$, since the variations of the critical pressure along the tube are negligible, we expect the same behaviour of the cylindrical tube, namely

$$\langle Q\rangle_T \propto \begin{cases} (\Delta P - \Delta \widetilde{P}_c)^{\frac{1}{n}} & \text{if } n < 1, \\ \Delta P - \Delta \widetilde{P}_c & \text{if } n > 1. \end{cases} \tag{3.28}$$

3.1.2.1 Non-analytic radius variability

We discuss now the case where $f(x_b/r_0)$ is not analytic. In the framework of the fiber bundle model, capillary tubes presenting non analytic points allows to model porous materials presenting a rough and angular micro-structure, e.g. matrices of randomly packed grains of quartz sand [95]. In the limit $\Delta P \to \Delta P_c^+$, the

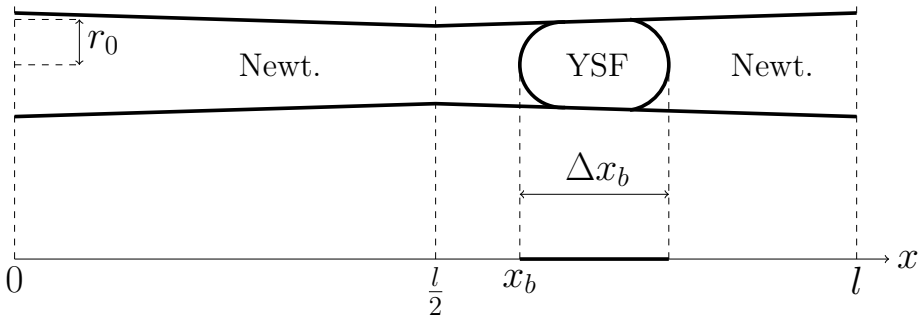

Figure 3.1.3: Two-dimensional sketch of a blob of yield stress fluid in a triangular tube. On the x-axis, the one-dimensional model relative to the problem is pictured, where the thick line is the projection along x of the yield stress blob, while the thin line represent the part occupied by the Newtonian fluid.

non-linear prediction of eq. (3.27) hold only if $\gamma(x_b/r_0)$ is derivable at least twice. Otherwise, its expansion around x_m is of the form: $\gamma(x_b) = \Delta P_c + \alpha|x_b - x_m|^\delta + \ldots$, with $\delta > 0$. In this case, the behavior of the integral in eq. (3.26) is modified and the flux averaged over T is then

$$\langle Q \rangle_T \propto (\Delta P - \Delta P_c)^{\frac{1}{n}+1-\frac{1}{\delta}}. \tag{3.29}$$

To provide a concrete example, we consider a saw-tooth triangular geometry:

$$f\left(x/r_0\right) = \frac{4r_0}{l}\left|\frac{x}{r_0} - \frac{l}{2r_0}\right| - 1, \quad x \in \left]0, l\right]. \tag{3.30}$$

A sketch of such geometry is shown in Figure 3.1.3. In this case we have

$$\Gamma(x_b/r_0) = P_{\tau_c}\left\{1 + \frac{4ar_0}{l}\left[\left|\frac{x_b}{r_0} - \frac{l}{2r_0}\right| + \frac{\gamma}{\tau_c r_0}\,\mathrm{sgn}\left(\frac{x_b}{r_0} - \frac{l}{2r_0}\right)\right]\right\} \tag{3.31}$$

Its maximum is located at the discontinuity point $x_m = l$ and writes

$$\Delta P_c = P_{\tau_c}\left\{1 + 2a\left[1 + \frac{2\gamma}{\tau_c l}\right]\right\}.$$

Integrating eq. (3.25) yields to $\delta = 1$ if the blob fluid presents yield stress, while $\langle Q \rangle_T \propto (\Delta P - \Delta P_c)^{\frac{1}{n}+1}$ in absence of yield stress ($\tau_c = 0$).

3.2 Model for many blobs in a tube

In this section we address the case of several identical blobs of non-Newtonian fluid in a tube (see figure 3.2.1). During the flow, the relative distances between different blobs remain constant as the fluids are incompressible.
In a uniform tube, since the capillary pressures across the interfaces of all blobs are canceling each other, the flow curve obtained when a single shot of non-Newtonian fluid is injected is identical to the one obtained when the same amount of fluid is split into N small blobs. Eq. (3.14) still holds, with the only modification

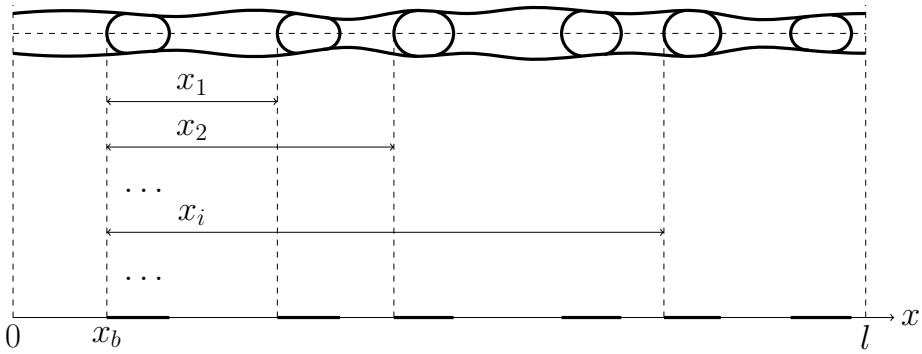

Figure 3.2.1: Two-dimensional sketch of several blobs of yield stress fluid in a non-uniform tube of length l. On the x-axis, the one-dimensional model relative to the problem is pictured, where the thick line is the projection along x of the yield stress blobs, while the thin line represent the part occupied by the Newtonian fluid.

that Δx_b has to be replaced with the total length occupied by the non-Newtonian fluid, $N\Delta x_b$. The same conclusion holds for a non-uniform tube in the limit $\Delta P \gg \Delta P_c$, for which the fluctuations given by the non-uniformity of the radius can be neglected.
On the other hand, for a non-uniform tube in the limit $\Delta P \to \Delta P_c^+$, it comes out that the critical pressure drop obtained with N blobs of length Δx_b is larger than $NP_{\tau_c} = 2N\Delta x_b\,\tau_c/r_0$, the value expected for a single shot of length equal to $N\Delta x_b$. The difference depends on the total number of blobs and on the specific blob configuration. Nevertheless, the behaviour of the flow rate averaged over a period will be identical, presenting the same power-law exponent $1/2 - 1/n$ for analytical radius deformations, or $1 - 1/n - 1/\delta$ for non-analytical ones.
Analogously to the situation with one blob, we parametrize the radius of the tube according to (3.15), and we shift the position of all blobs in the first period $0 < x < l$ by subtracting the quantity $(k-1)l$ for a blob located in the k-th period. We then denote with x_b the position of the most left blob and with x_i the distance from its i-th blob neighbour. Thus $i = 1, \ldots, N-1$, and the i-th right neighbour is located at $x_b + x_i$. When x_b moves from 0 to l, all the other blobs move exactly one period.
In the limit of small flow rate $Q \to 0$, the pressure drop at the edges of the i-th blob is

$$P^+_{x_b+x_i} - P^-_{x_b+x_i+\Delta x_b} = \Delta x_b \left(\frac{Q}{C_0 r_0^{4+\frac{1}{n}}}\right)^{\frac{n}{n+1}} + P_{\tau_c} + aP_{\tau_c} f\left(\frac{x_b + x_i}{r_0}\right). \qquad (3.32)$$

At this, one must add the capillary pressure drop $aP_\gamma \frac{\Delta x_b}{r_0} f'(\frac{x_b+x_i}{r_0})$. Summing the contributions of all the N blobs and neglecting the pressure drop induced by the Newtonian fluid, we obtain the following flow rate equation, that depends not only on the variable x_b, but also on the set of constant values $\{x_i\}$:

$$Q(x_b; \{x_i\}) = C_0 r_0^{4+\frac{1}{n}} \left[\frac{\Delta P - \Gamma(x_b/r_0; \{x_i/r_0\})}{N\Delta x_b}\right]^{\frac{1}{n}+1}, \qquad (3.33)$$

with

$$\Gamma\left(\frac{x_b}{r_0};\left\{\frac{x_i}{r_0}\right\}\right) = NP_{\tau_c} + a\left[P_{\tau_c}F\left(\frac{x_b}{r_0};\left\{\frac{x_i}{r_0}\right\}\right) + P_\gamma\frac{\Delta x_b}{r_0}F'\left(\frac{x_b}{r_0};\left\{\frac{x_i}{r_0}\right\}\right)\right], \tag{3.34}$$

where the function

$$F\left(\frac{x_b}{r_0};\left\{\frac{x_i}{r_0}\right\}\right) = f(x_b/r_0) + \sum_{i=1}^{N-1} f\left(\frac{x_b + x_i}{r_0}\right), \tag{3.35}$$

and $F'(y;\{\frac{x_i}{r_0}\})$ is the first derivative of $F(y;\{\frac{x_i}{r_0}\})$ with respect to y. The critical pressure ΔP_c needed for the system to flow is then given by the maximum of $\Gamma(\frac{x_b}{r_0},\{\frac{x_i}{r_0}\})$ in the interval $0 < x_b < l$:

$$\Delta P_c\left(\left\{\frac{x_i}{r_0}\right\}\right) = \max_{0\le x_b<l}\left[\Gamma\left(\frac{x_b}{r_0},\left\{\frac{x_i}{r_0}\right\}\right)\right]. \tag{3.36}$$

From eq. (3.36) we can see that the value of the critical pressure drop relies thus not only on the number of blobs, but also on the specific configuration of the blobs position along the tube, namely on their distances $\{x_i\}$. As a consequence, the flow of a given tube averaged over a period, $\langle Q\rangle_T = \langle Q(\{x_i\})\rangle_T$, depends on its specific blobs configuration, since it depends on its pressure threshold value $\Delta P_c = \Delta P_c(\{x_i\})$. However, we can manage to calculate its behaviour for $\Delta P \to \Delta P_c^+$:

$$T \propto \int_0^l \frac{dx_b}{\left[\Delta P - \Gamma\left(\frac{x_b}{r_0};\left\{\frac{x_i}{r_0}\right\}\right)\right]^{1+\frac{1}{n}}} \propto (\Delta P - \Delta P_c)^{-\left(\frac{1}{n}+\frac{1}{2}\right)} \tag{3.37}$$

and thus $\langle Q\rangle_T \propto (\Delta P - \Delta P_c)^{1/n+1/2}$ if the tube modulation is analytical, or, more generally, $\langle Q\rangle_T \propto (\Delta P - \Delta P_c)^{1/n+1-1/\delta}$. In the following Subsections we will show how to compute the pressure threshold for two specific tube geometries: sinusoidal geometry and triangular geometry, respectively.

3.2.1 Sinusoidal tube variability

We consider now a sinusoidal deformation of the tube, corresponding to

$$f(x/r_0) = \cos(2\pi x/l). \tag{3.38}$$

Since, in a porous medium, a typical pore consists of a narrow pore throat with two wide pore bodies at its ends, a long capillary tube with sinusoidal variability can be seen as a series of many pores. The flow in tubes deformed according to Eq. (3.38) was studied in the fully Newtonian case, when Newtonian blobs injected in a tube filled with another Newtonian fluid [36]. There, the authors analytically derived exact values for the pressure threshold and the mean flow rate averaged over a tube period, in both limits of pressure close to the threshold and high pressure. Here we derive an expression for ΔP_c, explicating its dependence on the blob position, and we compute $\langle Q\rangle_T$ in the limit $\Delta P \to \Delta P_c^+$.

It is useful to introduce the angle variables $\theta_b = 2\pi\frac{x_b}{l}$ and $\theta_i = 2\pi\frac{x_i}{l}$. Using the trigonometric relations, we can write

$$F(\theta_b;\{\theta_i\}) = \cos(\theta_b) + \sum_{i=1}^{N-1}\cos(\theta_b+\theta_i) = \sqrt{N}A\cos(\theta_b+\phi) \tag{3.39}$$

where the amplitude A and the phase shift ϕ are, respectively,

$$A = \frac{1}{\sqrt{N}}\sqrt{\left(1+\sum_{i=1}^{N-1}\cos\theta_i\right)^2+\left(\sum_{i=1}^{N-1}\sin\theta_i\right)^2} \tag{3.40}$$

$$\phi = \arcsin\left(\sqrt{N}\sum_{i=1}^{N-1}\sin\theta_i/A\right) \tag{3.41}$$

Similarly, we obtain $F'(\theta_b) = -(2\pi/l)\sqrt{N}A\sin(\theta_b+\phi)$. So $\Gamma(\theta_b,\{\theta_i\})$ can be written as a cosine function

$$\Gamma(\theta_b;\{\theta_i\}) = NP_\tau + \sqrt{N}A\,P_t\cos(\theta_b+\phi+\varphi) \tag{3.42}$$

where

$$P_t = a\sqrt{(P_{\tau_c})^2+\left(\frac{2\pi P_\gamma \Delta x_b}{l}\right)^2} = aP_{\tau_c}\sqrt{1+\left(\frac{2\pi\gamma}{\tau_c l}\right)^2}, \tag{3.43}$$

$$\varphi = -\arccos\left(\frac{P_{\tau_c}}{P_t}\right), \tag{3.44}$$

from which we can see that the pressure threshold is

$$\Delta P_c = NP_{\tau_c} + \sqrt{N}A\,P_t = P_{\tau_c}\left[N + a\sqrt{N}A\sqrt{1+\left(\frac{2\pi\gamma}{\tau_c l}\right)^2}\right]. \tag{3.45}$$

We now discuss two different cases, each related to a particular configurations of the blobs positions:

- Each blob is separated from its nearest neighbours by a distance equal to the spatial period l, namely $\theta_i = 0\ \forall\ i$. This implies that $A = \sqrt{N}$, and ΔP_c reaches the highest possible value

$$\Delta P_c = N\left(P_{\tau_c} + P_t\right) \tag{3.46}$$

- Each blob is separated from its nearest neighbours by half of the spatial period $l/2$, so $\theta_i = \pi$ for i odd and $\theta_i = 2\pi$ for i even. It follows that $A = 0$ if N is even, or $A = 1$ if N is odd, and ΔP_c takes the lowest possible value

$$\Delta P_c = \begin{cases} NP_{\tau_c} & \text{if } N \text{ even} \\ \\ NP_{\tau_c} + P_\gamma & \text{if } N \text{ odd} \end{cases} \tag{3.47}$$

In general, A can vary between these two extremes, depending on the blobs configuration.
The flow rate (3.33) can be written in angular coordinates

$$\frac{d\theta_b}{dt} = \frac{2C_0\, r_0^{2+\frac{1}{n}}}{l\Delta x_b^{1+\frac{1}{n}}}\left[\frac{\Delta P - NP_{\tau_c} - \sqrt{N}A\,P_t\cos(\theta_b+\phi+\varphi)}{N\Delta x_b}\right]^{\frac{1}{n}+1}, \tag{3.48}$$

from which we can write directly the time period

$$T = \frac{l\Delta x_b^{1+\frac{1}{n}}}{2C_0\, r_0^{2+\frac{1}{n}}}\int_0^{2\pi}\frac{d\theta_b}{\left[\Delta P - NP_{\tau_c} - \sqrt{N}A\,P_t\cos(\theta_b+\phi+\varphi)\right]^{1+\frac{1}{n}}} \tag{3.49}$$

The integral (3.49) is solvable once we set a value for n. For example, choosing $n = 1$ (Bingham fluid), since $\int_0^{2\pi} dx\,(K-\cos(x))^{-2} = 2\pi K(K^2-1)^{-3/2}$ for any $K > 1$, we can compute an explicit expression for the mean flow rate

$$\langle Q\rangle_T = \frac{\pi r_0^5}{8\Delta x_b \mu_b \tau_c}\frac{((\Delta P - NP_{\tau_c})^2 - NA^2P_t^2)^{\frac{3}{2}}}{\Delta P - NP_{\tau_c}}. \tag{3.50}$$

where we called μ_b the viscosity of the Bingham blob. As expected, $\langle Q\rangle_T \propto (\Delta P - \Delta P_c)^{\frac{3}{2}}$ as $\Delta P \to \Delta P_c^+$.

3.2.2 Triangular tube variability

We now discuss in detail the triangular saw tooth shape introduced in eq. (3.30). For simplicity, we focus on two limit cases: the fully Newtonian case (for which $\tau_c = 0$), and the case of non-Newtonian blobs but where capillarity effects can be neglected (for which $\gamma = 0$).

3.2.2.1 Blobs of Newtonian fluid

If the tube is non uniform, Newtonian blobs in a tube lead to a critical pressure due to the capillary pressure drop at their interfaces. The value of ΔP_c corresponds to the global maximum, in the interval $[0, l]$, of the function $\Gamma(x_b/r_0)$, expressed by Eq. (3.34), with $P_\tau = 0$, namely

$$\Delta P_c = \sqrt{N}AP_t, \tag{3.51}$$

where

$$A = \frac{1}{\sqrt{N}}\frac{l}{4r_0}\max_{0\le x_b<l}\left|F'\left(\frac{x_b}{r_0};\left\{\frac{x_i}{r_0}\right\}\right)\right| \tag{3.52}$$

and $P_t = (4r_0/l)aP_\gamma\Delta x_b$. We remind that $F'(y;\{\frac{x_i}{r_0}\})$ is the first derivative of Eq. (3.35) with respect to y, and can be seen as the sum of N contributions. For the triangular saw tooth shape, there is a contribution $-4r_0/l$ for every blob located in the semi-period interval $[0, l/2]$ and $+4r_0/l$ for every blob in the other semi-period $[l/2, l]$. When x_b moves from 0 to l, all the blobs are shifted of the same quantity. The function $\Gamma\,(x_b/r_0;\{x_i/r_0\})$ remains constant until one of the two facts occurs: either the most right blob belonging to the first semi-period enters

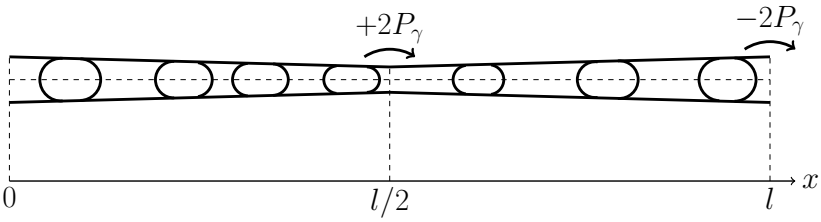

Figure 3.2.2: Sketch of several blobs in a tube presenting the triangular modulation given by Eq. (3.30).

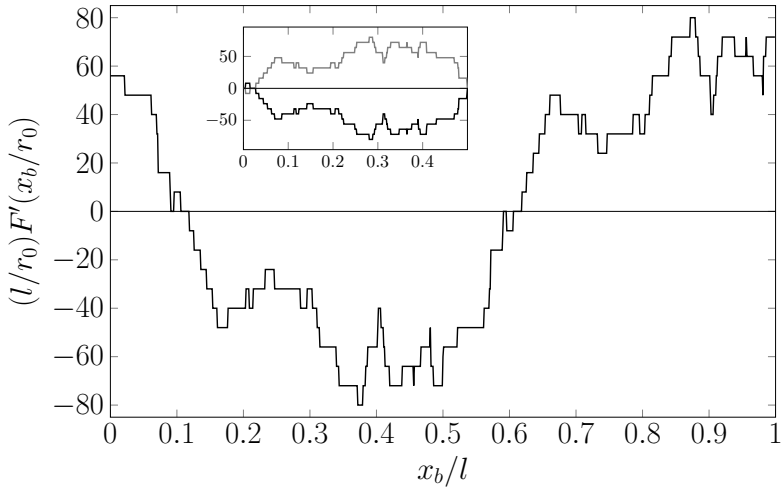

Figure 3.2.3: Plot of a typical $F'(x_b/r_0)$, obtained from eq. (3.30) and (3.35), in a triangular tube with $N = 50$ blobs uniformly distributed in $[0, l]$. Here we set $l = 1$. The two bridges are shown separately in the inset.

the second, so that the function Γ increases by $2P_t$, or the last blob belonging to the second semi-period enters the first, so that Γ decreases by $-2P_t$. A sketch of this procedure is shown in figure 3.2.2.

Increasing x_b further, other jumps occur for every blob entering in a new semi-period. γ corresponds then to a 1-dimensional *simple random walk* [96], a process in which, for each of the N steps corresponding to the N blobs, Γ will perform a step-wise increment of $\pm 2P_t$. Since the probability for a blob to be in the first or second semi-period is the same, Γ can increase by $2P_t$ or $-2P_t$ with equal probability, so this random walk is symmetric with a diffusion coefficient of $D = 2P_t^2$. Moreover, due to the periodicity of the system, this random walk is periodical of period l. A typical trajectory is shown in figure 3.2.3. The random walk displays the symmetry $\Gamma\left(x_b/r_0; \{x_i/x_0\}\right) = -\Gamma\left((l/2 + x_b)/r_0; \{x_i/x_0\}\right)$ and can be decomposed into two Brownian bridges with mirror symmetry, namely two Brownian processes constraint to both start and end at 0 and with opposite sign. If we denote the two processes $z_1(i)$ and $z_2(i)$, they evolve from $i = 0$, in which $z_1(0) = z_2(0) = 0$, to $i = N$, in which $z_1(N) = z_2(N) = 0$; the two bridges are identical but opposite in sign, namely $z_1(i) = -z_2(i)$. As a consequence, equation

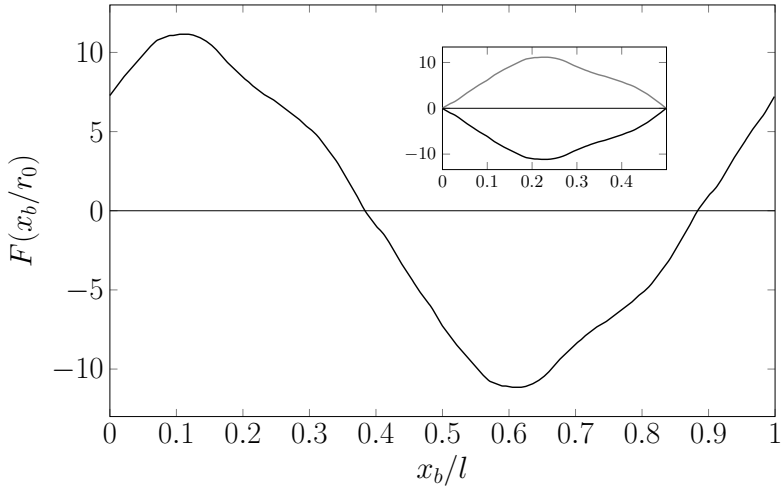

Figure 3.2.4: Plot of a typical $F(x_b/r_0)$, obtained from eq. (3.30) and (3.35), in a triangular tube with $N = 50$ blobs uniformly distributed in $[0, l]$. Here we set $l = 1$. The two bridges are shown separately in the inset.

(3.52) can be written as

$$A = \frac{1}{\sqrt{N}} \frac{l}{4r_0} \max_{0<i<N} |z_1(i)| \tag{3.53}$$

3.2.2.2 Blobs of yield stress fluid without capillary effects

The same approach allows to solve the case of blobs of Non-Newtonian fluid for which we neglect capillary effects. The value of ΔP_c corresponds to the maximum, in the interval $0 \leq x_b < l$, of (3.34) with $P_\gamma = 0$, namely

$$\Delta P_c = N P_{\tau_c} + \sqrt{N} A P_\gamma \tag{3.54}$$

where

$$A = \frac{1}{\sqrt{N}} \max_{0 \leq x_b < l} \left| F\left(\frac{x_b}{r_0}; \left\{\frac{x_i}{r_0}\right\}\right)\right| \tag{3.55}$$

and $P_t = a P_{\tau_c}$. Here $F\left(x_b/r_0; \{x_i/r_0\}\right)$ is the integral of the random walk discussed in the Newtonian case. A typical trajectory is shown in figure 3.2.4 and corresponds to the trajectory of a Random Acceleration Process (RAP) [97], a piecewise linear function where the slope performs a Random walk; in particular, this Gaussian process represents the integral of a Brownian Bridge, and is characterized by $H = 3/2$.

3.3 Model for a capillary tube bundle

Once the pressure threshold and the temporal averaged flow rate for a tube are obtained, we can calculate the flow rate in a capillary tube bundle, in which the same pressure drop ΔP is applied to many tubes which are identically shaped.

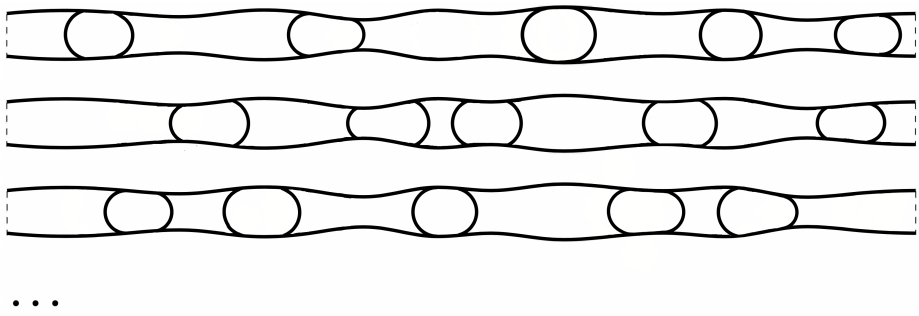

Figure 3.3.1: Sketch of a fiber bundle of identically shaped tubes, each filled with blobs randomly located along it.

Each tube is assumed to be filled with a Newtonian liquid together with N blobs injected at random positions along the tube, as pictured in Figure 3.3.1.

In the limit of many tubes, the mean flow rate averaged over the tubes is obtained by averaging over all possible configurations of the blobs positions. We will call it $\overline{\langle Q\rangle_T}$, where the overline denotes the average over the blob configurations. Since there is no preferred position of the blobs along the tube, the most important configuration is the one where the positions of the blobs are uniformly (evenly) distributed. In the diluted limit where $N\Delta x_b$ is very small compared to the tube length, the position of every blob shifted in the first period is uniformly distributed in the interval $[0, l]$. From this assumption, it is possible to calculate the probability distribution function of the critical pressure, $\Pi(\Delta P_c)$.

For ΔP slightly greater than NP_{τ_c}, we expect that the flow rate of every tube of the fiber bundle follows the small flow power-law exponent $1/n + 1 - 1/\delta$ if the pressure drop applied is greater than the pressure threshold of that tube, namely $\Delta P > \Delta P_c$, or is null if on the contrary $\Delta P \leq \Delta P_c$. Instead, we have tubes in the large flow limit, whose flow rate is described by the second case of eq. (3.14), only if ΔP is sufficiently greater than $\Delta\widetilde{P}_c = ((3n + 1)/(2n + 1))NP_\tau$. Since $NP_{\tau_c} < \Delta\widetilde{P}_c < (3/2)NP_{\tau_c}$ for all $n > 0$, there's always a finite range of values of ΔP for which all tubes in the bundle presenting non-null flow obey to the small flow regime. Moreover, $\Delta P_c \geq NP_{\tau_c}$ but is typically much lower than $\Delta\widetilde{P}_c$, because the fluctuations on the value of ΔP_c are smaller than the difference between NP_{τ_c} and $\Delta\widetilde{P}_c$. The effects on the mean flow rate caused by the non-uniformity of the tubes can then be seen only if ΔP is sufficiently close to NP_{τ_c}. In this limit we can compute the mean flow rate per tube as

$$\overline{\langle Q\rangle_T} \propto \int_{NP_{\tau_c}}^{\Delta P} d\Delta P_c\, \Pi(\Delta P_c)(\Delta P - \Delta P_c)^{\frac{1}{n}+1-\frac{1}{\delta}}. \tag{3.56}$$

In the following Subsections we will address to the specific cases of bundles of tubes presenting, respectively, sinusoidal and triangular deformation. While in the first case we explicitly compute an expression for $\Pi(\Delta P_c)$, in the latter only an estimation of its behaviour for $\Delta P_c \to NP_{\tau_c}$ (or $\Delta P_c \to 0$ in the fully Newtonian case) was provided. Nevertheless, in all cases we derive the behaviour of $\overline{\langle Q\rangle_T}$ for $\Delta P \to NP_{\tau_c}$ ($\Delta P \to 0$). It comes out that $\Pi(\Delta P_c)$, and thus the mean flow

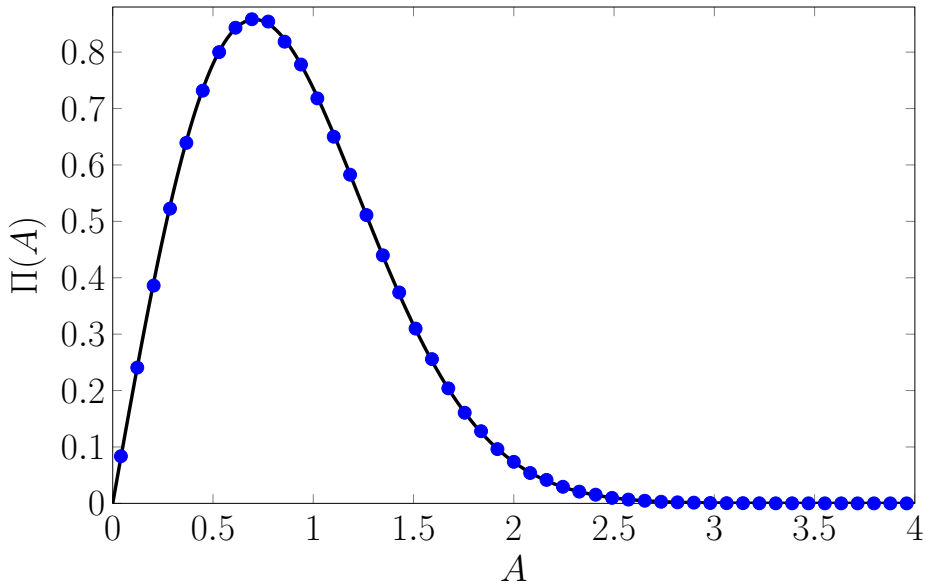

Figure 3.3.2: Probability distribution of the amplitude A defined in equation (3.41). Blue dots represent the histogram of 10^6 numerical samplings of A, each obtained generating $N = 1000$ values of θ_i uniformly distributed in $(0, 2\pi)$; the samplings are collected in 50 bins of equal size in the domain $[0, 4]$. The solid line is the analytical prediction given by equation (3.61).

rate of a fiber bundle, strongly relies on the geometry of the tubes. In particular, essential singularities are developed in presence of non-analytical behaviours.

3.3.1 Sinusoidal tube variability

In Subsection 3.2.1 we discussed the case when many blobs are injected in a sinusoidal tube, and we derived an expression for the threshold pressure, reported in Eq. (3.2.1). Since the fluctuations of ΔP_c corresponds to the fluctuations of A, we compute the probability distribution for A to derive the one for ΔP_c.
Assuming an uniform distribution for the position of every blob along the tube is equivalent to suppose that all the $N-1$ angular differences θ_i are uniformly distributed in the interval $[0, 2\pi]$. In the limit of N sufficiently large, A follows, in the interval $[0, +\infty[$, the probability distribution

$$\Pi(A) = 2A\, e^{-A^2}. \tag{3.57}$$

In order to prove eq. (3.57), we first calculate the probability distribution of the variable $B = NA^2$:

$$g(B) = \frac{1}{(2\pi)^{N-1}} \int_0^{2\pi} d\theta_1 \cdots \int_0^{2\pi} d\theta_{N-1}\, \delta\left(B - NA^2\right). \tag{3.58}$$

To solve (3.58), it's convenient to perform a Laplace transform:

$$\begin{aligned}\widetilde{g}(s) &= \int_0^{+\infty} dB\; e^{-sB} g(B) \\ &= \frac{1}{(2\pi)^{N-1}} \int_0^{2\pi} d\theta_1 \cdots \int_0^{2\pi} d\theta_{N-1}\, e^{-s\left(\left(1+\sum_{i=1}^{N-1}\cos\theta_i\right)^2+\left(\sum_{i=1}^{N-1}\sin\theta_i\right)^2\right)}\end{aligned} \tag{3.59}$$

We define $m_x = \sum_{i=1}^{N-1}\cos\theta_i$ and $m_y = \sum_{i=1}^{N-1}\sin\theta_i$. Note that the average and the variance of both $\cos\theta_i$ and $\sin\theta_i$ in the interval $[0, 2\pi]$, are respectively 0 and 1/2. Moreover, their crossed integral (the covariance) in the same interval is zero, meaning that m_x and m_y are statistical independent. According to the central limit theorem, when $N-1 \simeq N$ is sufficiently large, the distribution of both m_x and m_y is Gaussian with mean zero and variance $N/2$. Eq. (3.59) can be rewritten as

$$\begin{aligned}\widetilde{g}(s) \quad &= \int_{-\infty}^{+\infty} dm_x \frac{e^{-\frac{m_x^2}{N}}}{\sqrt{\pi N}} \int_{-\infty}^{+\infty} dm_y \frac{e^{-\frac{m_y^2}{N}}}{\sqrt{\pi N}} e^{-s\left((1+m_x)^2+m_y^2\right)} \\ &= \frac{e^{-s+\frac{s^2}{1/N+s}}}{1+Ns} \xrightarrow{N\gg 1} \frac{1}{1+Ns}.\end{aligned} \tag{3.60}$$

The inverse Laplace transform leads to $g(B) = \exp(-B/N)/N$, from which eq. (3.57) follows directly.
From $\Pi(A)$ we get the distribution of ΔP_c in the interval $[NP_{\tau_c}, +\infty[$:

$$\Pi(\Delta P_c) = \frac{2(\Delta P_c - NP_{\tau_c})}{NP_t^2}\, e^{-\frac{(\Delta P_c - NP_{\tau_c})^2}{NP_t^2}}. \tag{3.61}$$

The mean flow rate per tube is finally obtained from (3.56) and using $\Delta P \to (NP_{\tau_c})^+$ in eq. (3.61)

$$\overline{\langle Q\rangle_T} \propto (\Delta P - NP_{\tau_c})^{\frac{1}{n}+\frac{5}{2}}. \tag{3.62}$$

We can prove that this result is still robust if the N blobs have slightly different sizes (see Appendix A).

3.3.2 Triangular tube variability

Starting from the expressions for the critical pressure derived in Section 3.2.2, respectively for the fully Newtonian case and for the case without capillary effects, we now discuss the behaviour of their probability distributions and thus of the mean flow rate for a triangular tube bundle. We discover that, in both cases, $\overline{\langle Q\rangle_T}$ develops an essential singularity, which can be traced back to the presence of non-analytical points on the tube profile.

3.3.2.1 Blobs of Newtonian fluid

The amplitude of the critical pressure of a train of Newtonian blobs in a triangular tube corresponds to the maximum of a Brownian bridge, as reported in Eq. (3.53). The exact calculation of the distribution of the extreme values of Brownian bridges can be done using the methods discussed in [98]. However, the statistical behaviour

of $\max_{0<i\leq N}|z_1(i)|$ should be similar to the one of the span S of the process, defined as $S = \max_{0<i\leq N}(z_1) - \min_{0<i\leq N}(z_1)$. For the span, rigorous results are proven not only for the Brownian motion but for Gaussian processes with generic Hurst exponent H (the Brownian motion corresponds to $H = 1/2$). In particular, the probability to have a small span ε is known to vanish singularly as

$$\text{Prob}[S < \varepsilon] \propto e^{-\frac{kN}{\varepsilon^{1/H}}} \quad \text{for } \varepsilon \to 0, \tag{3.63}$$

where k is a numerical prefactor of order one [99]. From eq. (3.63), we can infer that the probability distribution of A vanishes as

$$\Pi(A) \propto A^{-3} e^{-\frac{k}{A^2}} \quad \text{for } A \to 0. \tag{3.64}$$

The presence of an essential singularity at the origin indicates that the tubes with small critical pressure are extremely rare. From (3.64) it follows that the probability distribution of ΔP_c goes as

$$\Pi(\Delta P_c) \propto (\Delta P_c)^{-3} e^{-\frac{2kNP_t^2}{(\Delta P_c)^2}} \quad \text{for } \Delta P_c \to 0. \tag{3.65}$$

From eq. (3.56) we then find that, in the limit of small ΔP, the mean flow rate per tube vanishes exponentially as

$$\overline{\langle Q\rangle_T} \propto e^{-\frac{2kNP_t^2}{\Delta P^2}}. \tag{3.66}$$

3.3.2.2 Blobs of yield stress fluid without capillary effects

In this case, the amplitude A corresponds to the maximum of a Random Acceleration Process, as shown in eq. (3.55). The methods discussed in [100] may be a starting point for deriving an exact form for the distribution of the extreme values of a RAP. However, following the lines of the previous discussion, we expect that the distribution of A vanishes at 0 as

$$\Pi(A) \propto \frac{1}{A^{5/3}} e^{-\frac{k^*}{A^{2/3}}} \quad \text{for } A \to 0. \tag{3.67}$$

k^* is a numerical prefactor different from k. It follows that the distribution of the critical pressure vanishes at NP_τ as

$$\Pi(\Delta P_c) \propto (\Delta P_c - NP_{\tau_c})^{-\frac{5}{3}} e^{-\frac{k^* N^{1/3} P_t^{2/3}}{(\Delta P_c - NP_{\tau_c})^{2/3}}} \quad \text{for } \Delta P_c \to NP_{\tau_c}. \tag{3.68}$$

For $\Delta P \gtrsim NP_{\tau_c}$ the mean flow rate per tube scales now as

$$\overline{\langle Q\rangle_T} \propto e^{-\frac{k^* NP_t^{2/3}}{(\Delta P - NP_{\tau_c})^{2/3}}}. \tag{3.69}$$

As a final remark we note that, as $H \to +\infty$ the function $\Gamma\left(\frac{x_b}{r_0}, \left\{\frac{x_i}{r_0}\right\}\right)$ becomes smoother in x_b and the critical pressure distribution remains singular, but at a higher order of derivative. The linear behaviour in the limit $\Delta P_c \to 0$ found for the sinusoidal case represents then the most regular behaviour we can expect.

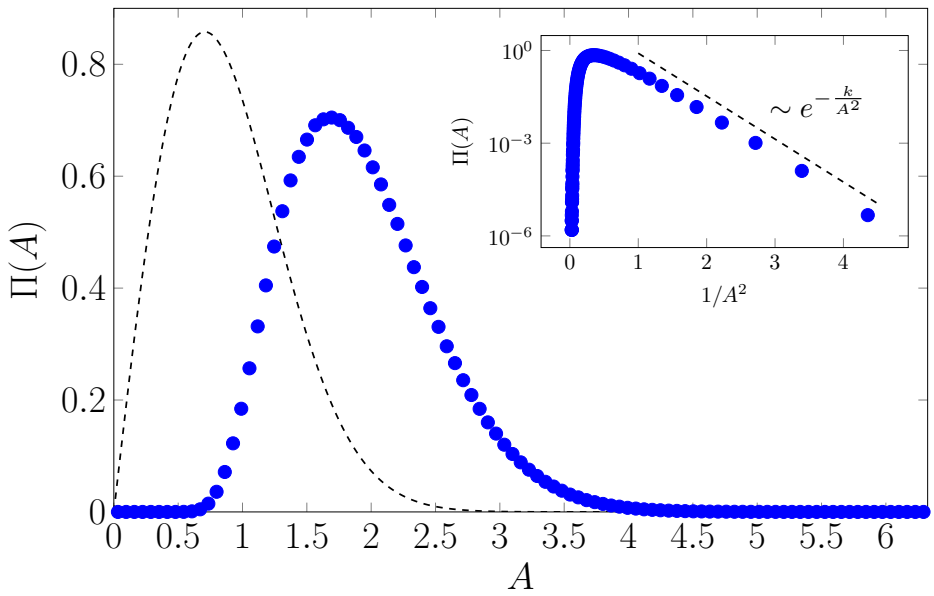

Figure 3.3.3: Distribution of A for a train of blobs of Newtonian fluid in a triangular tube. Blue dots represent the histogram of 10^7 numerical samplings of A, each obtained generating $N = 1000$ values of blob positions and calculating (3.52); the samplings are collected in 100 bins of equal size in the domain $\left[0, 200/\sqrt{N}\right]$. The dashed curve is the probability distribution (3.61) valid for a sinusoidal tube. In the inset, the numerical data $(A^{-2}, \Pi(A))$ are compared to the asymptotic trend of eq. (3.65) setting $k \simeq 3.2$.

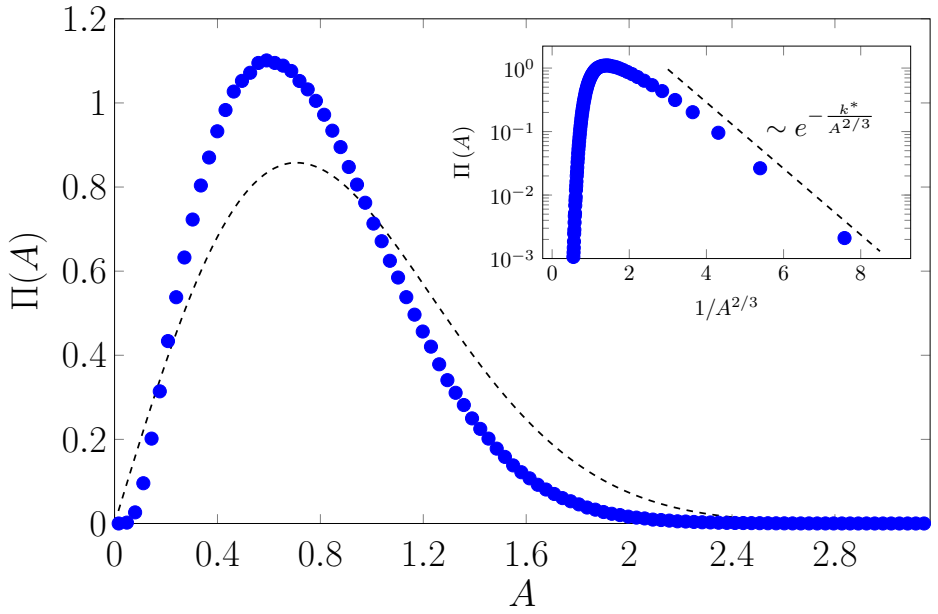

Figure 3.3.4: Distribution of A for a train of blobs of yield stress fluid in a triangular tube neglecting capillary effects. Blue dots represent the histogram of 10^7 numerical samplings of A, each obtained generating $N = 1000$ values of blob positions and calculating (3.55); the samplings are collected in 100 bins of equal size in the domain $\left[0, 100/\sqrt{N}\right]$. The dashed curve is the probability distribution (3.61) valid for a sinusoidal tube. In the inset, the numerical data $(A^{-2}, \Pi(A))$ are compared to the asymptotic trend of eq. (3.65) setting $k^* \simeq 1.2$.

CHAPTER

FOUR

BINGHAM FLOW IN A TREE-LIKE NETWORK

The goal of this Chapter is to study the Darcy problem of a Bingham fluid flowing in a pore network structured as a binary Cayley tree. This geometry is the simplest with intersecting channels, although is realistic for several biological networks (e.g. alveoli system in lungs [101] or leaf veins). Also, the Bingham approximation is the simplest among all possible models of fluids presenting yield stress, since it recovers a linear Newtonian behaviour after its threshold is overcome. Nevertheless, this model is able to reproduce a non-linear behaviour of the flow rate as a function of the applied pressure drop, which is typical of yield stress fluids in porous media, as explained in Section 2.1.2. Moreover, it can give important insights in predicting the evolution of the un-yielded region in a porous system, and thus of its permeability.
Before addressing to this study, we first illustrate in Section 4.1 a simpler model, namely a pore network made of several non-intersecting channels. This can be helpful in better understanding the study of the flow in the Cayley tree pore network, which is then addressed in Section 4.2.

In a porous system composed of several channels filled with a Bingham fluid, in general only a subset of them is flowing, depending whether the imposed pressure drop is greater than the critical one ΔP_c associated to each of them. Considering a collection of independent channels, each one made of t tubes presenting a random threshold, ΔP_c is distributed according to a Gaussian PDF in the limit of high t. Hence, we use a mapping with the Random Energy Model to prove that the number of flowing channels, when a pressure drop ΔP is imposed on the system, is

$$\lim_{t\to\infty} \overline{n^{\mathrm{ind}}(\Delta P - \Delta P_{\mathrm{min}})} = e^{\beta_c(\Delta P - \Delta P_{\mathrm{min}})}, \tag{4.1}$$

where ΔP_{min} is the minimum value of ΔP_c among all channels, β_c is a non-universal constant, and the overline stands for an average over many configurations of the tubes thresholds. The flow rate of a Bingham fluid in such a pore network can be then written as the sum of the contribution from each channel. For moderate pressure drops we have

$$\overline{Q_t(\Delta P)} \overset{t\gg 1}{=} \frac{e^{\beta_c(\Delta P - \Delta P_{\mathrm{min}})} - 1}{\beta_c t} \quad \text{for } \Delta P > \Delta P_{\mathrm{min}}, \tag{4.2}$$

while for much higher pressures all channels are open, and we have

$$\overline{Q_t(\Delta P)} = \frac{2^t}{t}(\Delta P - t\overline{P_\tau}) \quad \text{for } \Delta P \to \infty \tag{4.3}$$

where $\overline{P_\tau}$ is the average tubes threshold.
In a pore network shaped as a binary Cayley tree, filled with a Bingham fluid, we can identify channels starting from the root and finishing to any of the tree leaves, that can be open or not depending on their value of ΔP_c. We establish a precise mapping between the Darcy problem for Bingham fluids and the directed polymer on Cayley tree, a model displaying one-step replica symmetry breaking (1-RSB). Starting from the first channel that opens at $\Delta P_{\min}$ and increasing ΔP, the first channels where flow occurs correspond to those low-energies directed polymers with small overlaps (i.e. they share a short common path). The number of flowing channels above the minimum turns out to be equivalent to the same number for the model of independent channels, namely

$$\lim_{\hat{q}\to\infty} \overline{m_{\hat{q}}(\Delta P - \Delta P_{\min})} = e^{\beta_c(\Delta P - \Delta P_{\min})}. \tag{4.4}$$

Again, the total flow rate comes from the contribution of the single channels, so for rather low pressure drops we have

$$\overline{Q_t(\Delta P)} \overset{t\gg 1}{=} \frac{e^{\beta_c(\Delta P - \Delta P_{\min})} - 1}{\beta_c t} \quad \text{for } \Delta P > \Delta P_{\min}, \tag{4.5}$$

and at higher pressures the linear behaviour is recovered, but with a much lower permeability with respect to the case of non-intersecting channels

$$\overline{Q_t(\Delta P)} = \frac{1}{2}(\Delta P - t\overline{P_\tau}) \quad \text{for } \Delta P \to \infty. \tag{4.6}$$

This implies that it is sufficient to open $\sim t$ channels to reach the permeability at saturation, and thus the linear regime of Eq. (4.6).

4.1 Model for a Bingham fluid in independent channels

In this Section we deal with a pore network model made of N independent channels, each one made of t tubes connected in series (see Figure 4.1.1). The tubes, representing the pore throats, embed all the pore network volume, while the nodes are seen only as crossing points of zero volume. We fill the network with a Bingham fluid and we apply the same pressure drop $\Delta P > 0$ at the edges of each channel. As every tube presents in general a different geometry, both its pressure threshold and conductivity might vary. We consider here the simplified case in which the conductivity is equal to 1 for all tubes, while the pressure threshold P_τ fluctuates from tube to tube according to a certain probability distribution $\rho(P_\tau)$, where we indicate with $\overline{P_\tau}$ and σ its mean and standard deviation respectively. We are interested in calculating the total flow rate Q_t of the pore network as a function of the pressure applied ΔP.

For every channel, the flow rate across its i-th tube, between the pore i, at pressure P_i, and the pore $i+1$, at pressure $P_i + 1 > P_i$ (with $i = 1, \ldots, t$) reads

$$Q_i = (P_{i+1} - P_i - P_{\tau,i})_+ \tag{4.7}$$

where we denote $(x)_+ = \max(0, x)$. The tube is open if $P_{i+1} - P_i > P_{\tau,i}$. From

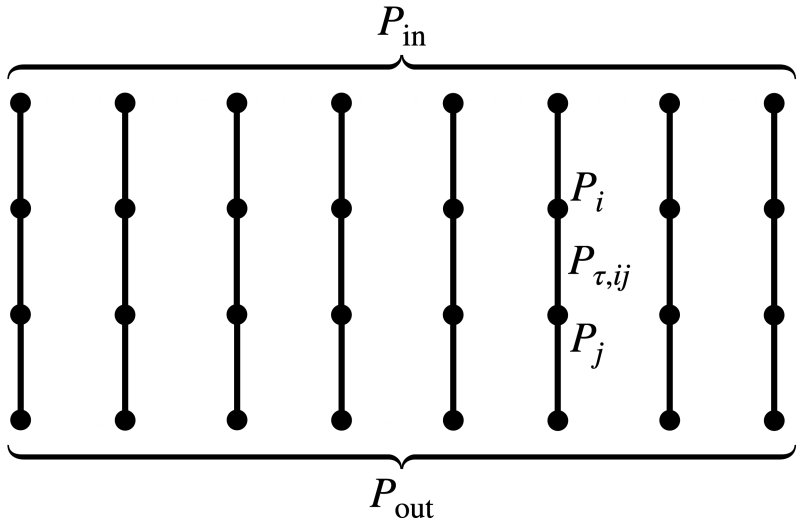

Figure 4.1.1: Sketch of a pore network made of $2^3 = 8$ non-intersecting channels, each one made of 3 tubes. A pressure $\Delta P = P_{\text{in}} - P_{\text{out}}$ is imposed at the edge of each channel. The pressure threshold $P_{\tau,ij}$ assigned to the tube connecting the nodes i and j is highlighted, together with the pressures P_i and P_j at the respective nodes.

eq. (4.7), using the Kirchhoff condition $Q_i = Q_{i+1}$ for all i, we can derive the flow rate $Q_{\alpha,t}$ along the α-th channel (with $\alpha = 1, \ldots, N$) as a function of ΔP:

$$Q_{\alpha,t}(\Delta P) = \frac{1}{t}\left(\Delta P - \Delta P_c^{(\alpha)}\right)_+ \tag{4.8}$$

where $\Delta P_c^{(\alpha)}$ is the pressure threshold related to the α-th channel, equal to the sum of the pressure thresholds of each of its t tubes

$$\Delta P_c^{(\alpha)} = \sum_{i=1}^{t} P_{\tau,i}. \tag{4.9}$$

Since the different channels are independent, the total flow rate of the network is simply the sum of the flow rates (4.8) across each channel

$$Q_t(\Delta P) = \sum_{\alpha=1}^{N} Q_{\alpha,t}(\Delta P) = \frac{1}{t}\sum_{\alpha=1}^{N}\left(\Delta P - \Delta P_c^{(\alpha)}\right)_+ . \tag{4.10}$$

Clearly, the flow in the network is non-null only if $\Delta P > \Delta P_{\min} \equiv \min_\alpha \Delta P_c^{(\alpha)}$. We now define the number of open channels, above the one with the minimal critical pressure $\Delta P_{\min}$, up to a quantity $x > 0$ as

$$n_t^{\mathrm{ind}}(x) = \#\left(\Delta P_c^{(\alpha)} : \Delta P_{\min} \leq \Delta P_c^{(\alpha)} < \Delta P_{\min} + x\right) = \sum_{\alpha=1}^{N} \vartheta\left(\Delta P_{\min} + x - \Delta P_c^{(\alpha)}\right). \tag{4.11}$$

where the label 'ind' refers to the independent channels model, and $\vartheta(x)$ is the Heaviside theta function. The derivative of (4.11), namely

$$\frac{dn_t^{\mathrm{ind}}(x)}{dx} = \sum_{\alpha=1}^{N} \delta\left(\Delta P_{\min} + x - \Delta P_c^{(\alpha)}\right), \tag{4.12}$$

where $\delta(x)$ is the Dirac delta function, gives the density of open channels above the minimum. Using Eq. (4.12), the total flow rate (4.10) can be rewritten in an integral form

$$Q_t(\Delta P) = \frac{1}{t}\int_0^x dx'\,(x - x')\frac{dn_t^{\mathrm{ind}}(x')}{dx} = \frac{1}{t}\int_0^x dx'\, n_\infty^{\mathrm{ind}}(x'); \tag{4.13}$$

in the first passage we have introduced the variables $x = \Delta P - \Delta P_{\min}$ and $x' = \Delta P_c - \Delta P_{\min}$, while in the second we performed an integration by parts. As illustrated in the following, an expression for $n_t^{\mathrm{ind}}(x)$ can be computed thanks to a mapping between this pore network model and the Random Energy Model (REM), introduced and discussed in Appendix B.1.
For sufficiently large t, thanks to the central limit theorem, the PDF of ΔP_c is well-approximated by a Gaussian of mean $t\overline{P_\tau}$ and standard deviation $t\sigma^2$:

$$\Pi_t(\Delta P_c) = \frac{e^{-\frac{(\Delta P_c - t\overline{P_\tau})}{t\sigma^2}}}{\sqrt{\pi t}\sigma}. \tag{4.14}$$

Assuming the power-law scaling $N = 2^t$, the model of N channels can thus be seen as a Random Energy Model. The pressure thresholds of the independent channels corresponds to the energy levels of the REM, which are generated according to a Gaussian distribution analogous to (4.14). As a consequence, the number of open channels above $\Delta P_{\min}$ is equivalent to the the number of energy levels above the minimum in the REM, that we call n_t^{REM}. In Appendix B.1 we computed an explicit expression for n_t^{REM}, when we average it over many realizations of the disorder and we take the limit of large t. So, given that $n_t^{\mathrm{ind}} \equiv n_t^{\mathrm{REM}}$, we have

$$n_\infty^{\mathrm{ind}}(x) = \lim_{t\to\infty} \overline{n^{\mathrm{ind}}(x)} = e^{\beta_c x}; \tag{4.15}$$

here $\beta_c = \sqrt{2\log 2}/\sigma$, and the overline stands for an average over many realizations of the pressure thresholds. Hence, using both Equations (4.13) and (4.15), we get the average of (4.13) in the limit of many channels:

$$\overline{Q_t(\Delta P_{\min} + x)} \overset{t\gg 1}{=} \frac{e^{\beta_c x} - 1}{\beta_c t}. \tag{4.16}$$

The growth of the flow rate with the pressure drop applied is thus highly non-linear, showing an exponential behaviour. This implies that in the limit $\Delta P \to$

$\Delta P^+_{\min}$ the flow is linear $Q_t(\Delta P) = (\Delta P - \Delta P_{\min})/t$, which corresponds to the case where only the channel with minimum threshold is open. Equation (4.16) holds only for moderately high pressure drops. Instead, for very high ΔP, all the 2^t tubes are open and we recover linearity

$$\overline{Q_t(\Delta P)} = \frac{2^t}{t}(\Delta P - \Delta P^*) \quad \text{for } \Delta P \to \infty \tag{4.17}$$

The effective threshold ΔP^* in Eq. (4.17) can be computed observing that, when all tubes are open,

$$\overline{Q_t(\Delta P)} = \sum_{\alpha=1}^{2^t} \frac{\Delta P - \Delta P_c^{(\alpha)}}{t} \overset{t\gg 1}{=} \frac{2^t}{t}(\Delta P - t\overline{P_\tau}), \tag{4.18}$$

so $\Delta P^* = t\overline{P_\tau}$. Equations (4.16) and (4.17) are both valid in different ranges of ΔP, so there will be a pressure drop, that we name ΔP_{sat}, at which the crossover between the two different regimes occurs. We can estimate ΔP_{sat} imposing the effective permeability in the exponential regime, namely $\overline{\kappa_{\text{eff}}} = d\overline{Q_t}/d\Delta P \sim \exp(\beta_c(\Delta P - \Delta P_{\min}))/t$, to be equal to the one in the high pressure drop regime, $\frac{2^t}{t}$. In this way we obtain

$$\Delta P_{\text{sat}} = \Delta P_{\min} + \frac{\ln 2}{\beta_c} t \tag{4.19}$$

As a consequence, at the saturation pressure, the number of channels obtained by Equation (4.15) is 2^t, meaning that all channels open already at $\Delta P = \Delta P_{\text{sat}}$. The problem of independent channels proves to be helpful for understanding another, more complex problem, the flow of a Bingham fluid in a pore network structured as a Cayley tree. We analyze it in detail the next Section, also highlighting the similarities between the two models.

4.2 Model for a Bingham fluid on a Cayley tree

We consider a pore network with the structure of a binary Cayley tree of t levels (see Figure 4.2.1). We fill the structure with a Bingham fluid and we apply a pressure P_{in} to the root pore and a pressure P_{out} to each of the 2^{t-1} leaf pores, such that the pressure drop $\Delta P = P_{\text{in}} - P_{\text{out}} > 0$ between the root and the leaves is the same. Similarly to Section 4.1, we suppose that each tube connecting two pores present conductivity equal to 1 and a pressure threshold P_τ randomly generated from a probability distribution $\rho(P_\tau)$. The flow rate in the tube between the generic nodes i and j can still be described by the modified Poiseuille equation

$$Q_{ij} = (P_i - P_j - P_{\tau,ij})_+. \tag{4.20}$$

As for the previous problem, we are interested in calculating the total flow rate Q across the network as a function of the imposed pressure drop ΔP.

According to Kirchhoff's law, for every node in the bulk (different from the root and the leaves), the flow in the incoming tube, coming from the previous level, must be equal to the sum of the flow in the two outgoing tubes, reaching the

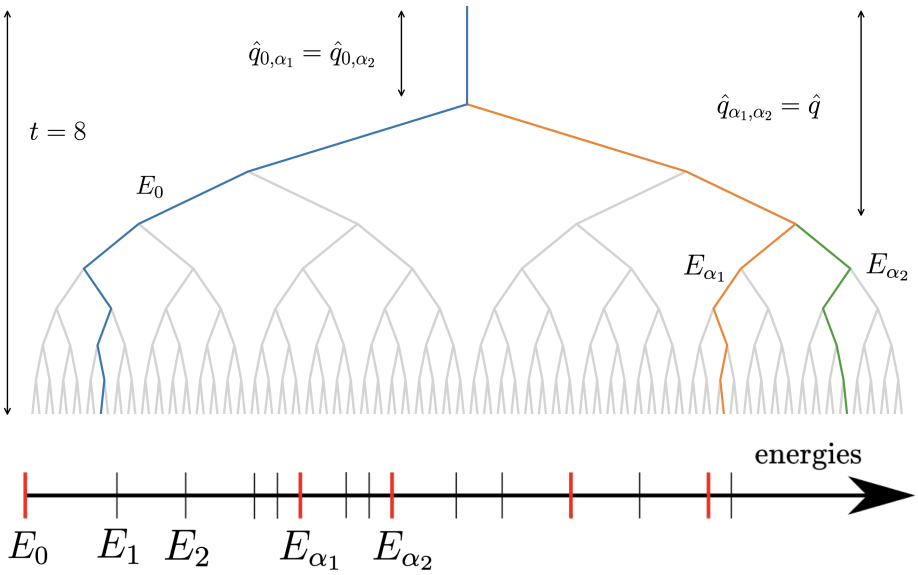

Figure 4.2.1: Top: Binary Cayley tree with $t = 8$ levels. The first channels where flow occur are the leftmost path in blue, at the pressure $\Delta P_c^{(0)}$, the middle path in orange α_1, at pressure $\Delta P_c^{(1)} > \Delta P_c^{(0)}$ and the rightmost path in green α_2, at pressure $\Delta P_c^{(2)} > \Delta P_c^{(1)}$. We denote with $\hat{q}_{\alpha_1\alpha_2}$ the overlap between α_1 and α_2, namely the length of the common path between them (here $\hat{q}_{\alpha_1\alpha_2} = 3$). Similarly $\hat{q}_{0\alpha_1}$ and $\hat{q}_{0\alpha_2}$ are the overlaps of α_1 and α_2 with the blue path (here $\hat{q}_{0,\alpha_1} = \hat{q}_{0,\alpha_2} = 1$) and $\hat{q}$ is the maximal overlap between all of them (here $\hat{q} = 3$). Bottom: sorted energies of the associated directed polymer $E_0 < E_1 < E_2, \ldots$. The energies corresponding to small overlap paths are in red. In the large-t limit we show that $\hat{q} \ll t$ and $\Delta P_c^{(1)} = E_{\alpha_1}, \Delta P_c^{(2)} = E_{\alpha_2}, \ldots$.

following level. It follows that, given an open incoming tube, there must be at least one outgoing open tube. Thus, along a channel from the root to a leaf, flow occurs if all its t tubes are open. There are then 2^{t-1} channels across the pore network, each of which can be open or closed whether the pressure drop ΔP applied to the system is larger or smaller than the correspondent critical pressure at which it opens. We can order these critical pressures as $\Delta P_c^{(0)} < \Delta P_c^{(1)} < \Delta P_c^{(2)} < \ldots$, where the number (a) in the superscript indicates the $a+1$-th channel that opens if we gradually increase ΔP from 0 (so (0) refers to the first channel that opens). In this extent, we can establish a mapping between this pore network model and the problem of the directed polymer on a Cayley tree, illustrated in Appendix B.2. Each channel from the root to a leaf in the porous structure corresponds to a directed polymer on the tree network. Moreover, the sum of the pressure thresholds along the channel corresponds to the energy of the associated directed polymer. It is then useful to label the channels α by ordering their energies as $E_0 < E_1 < E_2 < \ldots$.

We now investigate the behaviour of the first channels that opens when increasing the pressure starting from the minimal one, namely $\Delta P_c^{(0)}$. We will show that

the first channels present low overlap, that, in the limit of high t, translates into vanishing overlap. In this way, similarly to the problem of independent channels, the computation of the total flow rate reduces to the calculation of the number of channels that opens above $\Delta P_{\min} = \Delta P_c^{(0)}$, which will be derived thanks to the mapping with the directed polymer problem.

4.2.1 Opening of the first channels

The pressure $\Delta P_c^{(0)}$ at which the first channel opens is given by

$$\Delta P_c^{(0)} = \min_{\alpha} \sum_{(ij)\in\alpha} P_{\tau,ij}. \tag{4.21}$$

As observed in [32], the threshold pressure drop $\Delta P_c^{(0)}$ identifies with the ground state energy of the associated directed polymer model, namely $\Delta P_c^{(0)} = E_0$. The fluid starts to flow in the network only above the critical pressure drop $\Delta P_c^{(0)}$ and only along the channel that coincides with the ground state of the directed polymer. In this case the flow rate is equal to

$$Q_t(\Delta P) = \frac{\Delta P - \Delta P_c^{(0)}}{t} \tag{4.22}$$

Equation (4.22) holds for $\Delta P \in [\Delta P_c^{(0)}, \Delta P_c^{(1)}]$, being $\Delta P_c^{(1)}$ the pressure drop at which a second channel opens. The pressures $\Delta P_c^{(1)}, \Delta P_c^{(2)}, \dots$ at which the following channels open are still related to the low-energy levels of the directed polymer, although the relation is not trivial anymore.
For example, the pressure drop $\Delta P_c^{(1)}$ at which the second channel opens can be computed using Kirchhoff's law and is equal to

$$\Delta P_c^{(1)} = \Delta P_c^{(0)} + \min_{\alpha\neq 0} \frac{E_\alpha - \Delta P_c^{(0)}}{1 - \hat{q}_{0\alpha}/t} = \Delta P_c^{(0)} + \frac{E_{\alpha_1} - \Delta P_c^{(0)}}{1 - \hat{q}_{0\alpha_1}/t}; \tag{4.23}$$

see Appendix C.1 for a complete proof. Here $\hat{q}_{0\alpha}$ stands for the overlap between the α channel and the ground state, namely the number of common tubes between the two channels. The path α_1 realises the minimum and corresponds to the channel that opens just above $\Delta P_c^{(1)}$. The minimization involves two terms: the term $E_\alpha - \Delta P_c^{(0)}$ favors low-energy paths while the term $1/(1 - \hat{q}_{0\alpha}/t)$ selects the ones with a small overlap with the ground state. The low overlap occurring between low-energy paths can be explained by the one step replica symmetry breaking displayed by the directed polymer on Cayley tree (see Appendix B.2). The total flow reduces thus to the sum of the contribution from each channel, namely $Q_t(\Delta P) = (\Delta P - \Delta P_c^{(0)})/t + (\Delta P - \Delta P_c^{(1)})/t$ for $\Delta P \in [\Delta P_c^{(1)}, \Delta P_c^{(2)}]$. The same property holds for the following pressures (see Appendix C.2 for a proof for $\Delta P_c^{(2)}$): the channels $\alpha_2, \alpha_3, \dots$ correspond to paths with the low-energy and low-overlap and $\Delta P_c^{(2)}, \Delta P_c^{(3)}, \dots$ coincide with the energies $E_{\alpha_2}, E_{\alpha_3}, \dots$ (see sorted energies at the bottom of Fig. 4.2.1). Similarly, the total flow reduces to the sum of the contribution from each channel.
As a consequence, like for the independent channels, the computation of the flow

rate problem reduces to determine the evolution of the number of open channels above the minimal one as a function of $x = \Delta P - \Delta P_c^{(0)}$, namely

$$n_t^{\rm ch}(x) = \sum_{\alpha=1}^{2^{t-1}} \vartheta\left(x - \left(\Delta P_c^{(\alpha)} - \Delta P_c^{(0)}\right)\right). \tag{4.24}$$

In the limit $t \to \infty$, the open channels coincide with the low-energy paths with vanishing overlap and the pressures $\Delta P_c^{(1)}, \Delta P_c^{(2)}, \ldots$ with the corresponding path energies $E_{\alpha_1}, E_{\alpha_2}, \ldots$. So $n^{\rm ch}(x)$ identifies with the number of low-energy levels of the directed polymer provided that they have low overlap among them. In the next Subsection, we will show how to calculate it.

4.2.2 Number of open channels above the minimum

In Appendix B.2 we introduce $n_t^{\rm full}$, namely the number of directed polymers on the Cayley tree with energy above the minimum. Thanks to an approach based on the discrete KPP equation [102, 103, 104, 105, 106, 107], in the limit of $t \to \infty$ we have

$$\overline{n_\infty^{\rm full}}(x) \simeq x e^{\beta_c c x}; \tag{4.25}$$

here the overline refer to the average over many realizations of the energies of the tree links. Since the open channels in the Cayley tree pore network coincide with the low-energy paths with vanishing overlap, the number of open channels $n_t^{\rm ch}(x)$ will consist in a subset of low-energy paths. In this Section we modify the KPP approach used in the Appendix to compute $\overline{n_\infty^{\rm ch}(x)}$, namely the number of open channels in the limit $t \to \infty$ averaged over many realizations of the tubes thresholds.

We introduce the quantity $m_{\hat{q}}(x)$, which counts in an infinite tree the number of paths with energy $E_0 \le E_\alpha < E_0 + x$ and maximum overlap between any of them $\hat{q}$. This is equivalent to first take the limit $t \to \infty$ and then consider only low-energy paths with vanishing overlap $\hat{q} \ll t$. This remains valid also for high $\hat{q}$, even in the limit $\hat{q} \to \infty$, so that

$$n_\infty^{\rm ch}(x) = \lim_{\hat{q}\to\infty} \overline{m_{\hat{q}}(x)} \tag{4.26}$$

We now introduce a procedure that can be referred as "pruning" (see Fig. 4.2.2): at the level $\hat{q}$ of the full Cayley tree, there are $2^{\hat{q}}$ subtrees that we label by $a = 1, \ldots, 2^{\hat{q}}$. We replace each of these subtrees with a single tube with a minimum energy $E_0^{(a)}$. This way we obtain a tree of $\hat{q}$ levels containing the $2^{\hat{q}}$ low energies paths with maximal overlap $\hat{q}$. This procedure is equivalent to growing a tree with $\hat{q}$ levels where the leaves thresholds are drawn from the distribution of the minimum of an infinite tree. We call $w_{\min}(x)$ the probability that the minimal energy of an infinite tree is larger than x.

The equations describing $\overline{m_{\hat{q}}(x)}$ will then be similar to the ones introduced in Appendix B.2 for $\overline{n_\infty^{\rm full}(x)}$. Namely, we have that $\overline{m_{\hat{q}}(x)} = \int dx'\, r_{\hat{q}}(x'; x)$, where the function $r_{\hat{q}}(x'; x)$ satisfies the following recursive equation:

$$r_{\hat{q}+1}(x'; x) = 2 \int dP_\tau\, \Pi(P_\tau) \Omega_t(x' - P_\tau) r_t(x' - P_\tau; x), \tag{4.27}$$

$$w_{\min}(x + c(\beta_c)) = \int dP_\tau\, \Pi(P_\tau) w_{\min}^2(x - P_\tau), \tag{4.28}$$

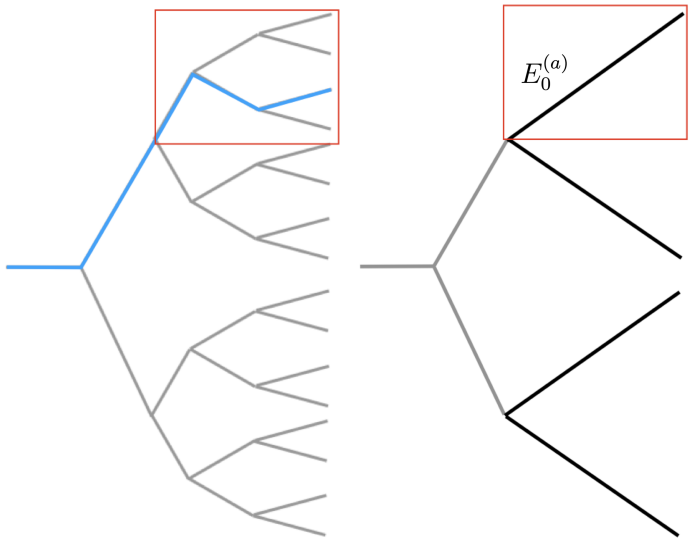

Figure 4.2.2: Left: An example of Cayley tree. The minimal path of the topmost subbranch after $\hat{q} = 2$ generations is shown highlighted in blue. Right: Pruning of the full Cayley tree, where within each subtree starting from the $\hat{q} = 2$ generation, only the minimal path is retained.

with the initial condition $r_{\hat{q}=1}(x';x) = -w'_{\min}(x + x')$. Equation (4.27) is the discrete KPP equation, which corresponds to growing a $\hat{q}$+1-level tree starting from two $\hat{q}$-level trees. Unlike for $\overline{n_\infty^{\text{full}}(x)}$, the recurrence is implemented in $\hat{q}$ instead of t. Equation (4.28) is a fixed-point equation which admits travelling wave solutions; $c(\beta_c)$ is the minimal value for which eq. (4.28) has a solution, and corresponds to the velocity of the travelling wave. Its value can be obtained as:

$$\beta_c = \arg\min_\beta c(\beta) \tag{4.29a}$$

$$c(\beta) = \frac{1}{\beta}\log\left(2\int d\tau p(\tau)e^{-\beta\tau}\right) \tag{4.29b}$$

The function $w_{\min}(x)$ corresponds then to a sigmoid with $w_{\min}(x) \simeq 1 - x\exp(\beta_c x)$ for $x \to -\infty$ and $w_{\min}(x) \simeq 0$ for $x \to \infty$. The solution of eq. (4.28) is defined up to an arbitrary shift that we set to zero for simplicity. (More information about the derivation of $w_{\min}$ and its velocity $c(\beta_c)$, and more in general about the discrete KPP equation, are reported in Appendix (B.2.1).)
A direct numerical integration of $r_{\hat{q}}(x';x)$ (Fig. 4.2.4 (right)) show that, when $\hat{q} \to \infty$, the expression of $n_\infty^{\text{ch}}(x)$ is:

$$n_\infty^{\text{ch}}(x) = \lim_{\hat{q}\to\infty} \overline{m_{\hat{q}}(x)} = e^{\beta_c x}. \tag{4.30}$$

It comes out that the number of open channels above the one at minimal pressure in the Cayley tree pore network is equivalent to the analogous number in the model of independent channels, discussed in the previous Section and reported in Eq. (4.15).

4.2.3 Determination of the flow rate

For moderately high pressures, as for the independent channels problem, the total flow rate reduces to the sum of independent contributions $Q_t(\Delta P_{\min} + x) = \int_0^x dx'\, n_t^{\rm ch}(x-x')/t$, where $\Delta P_{\min} \equiv \Delta P_c^{(0)}$. For large t, this leads to the same flow rate of eq. (4.16), namely

$$\overline{Q_t(\Delta P_{\min} + x)} \overset{t\gg 1}{=} \frac{e^{\beta_c x} - 1}{\beta_c t}. \tag{4.31}$$

Again, this expression captures the first two regimes of the flow: when $\Delta P \to \Delta P_{\min}$ the flow is linear, corresponding to Eq. (4.22), while for larger pressures an exponential regime takes over.
At very high pressure drop, instead, when all channels are open, we recover the second linear behavior with

$$Q_t(\Delta P) = \kappa(\Delta P - \Delta P^*) \quad \text{with } \Delta P \to \infty \tag{4.32}$$

The permeability κ can be computed observing that for finite t the following recursive equation holds

$$\kappa_t = \frac{2\kappa_{t-1}}{1 + 2\kappa_{t-1}} \tag{4.33}$$

which, together with $\kappa_1 = 1$, allows to find the solution $\kappa_t = 2^{t-1}/(2^t - 1)$. So, for large t, $\kappa \simeq 1/2$. The effective threshold ΔP^* is found noting that the total flow rate in a Cayley tree of t levels obeys the following recursive equations

$$Q_t(P_{\rm in}) = (P_{\rm in} - P' - P_\tau)_+ \tag{4.34}$$

$$(P_{\rm in} - P' - P_\tau)_+ = Q_{t-1}^{(l)}(P') + Q_{t-1}^{(r)}(P') \tag{4.35}$$

The first equation is the flow rate across the tube between the root, at pressure $P_{\rm in}$, and the following node, at pressure P', while the second comes from Kirchhoff's law applied at the latter node, which connects the two different sub-trees of $t-1$ levels, indicated by the superscripts (l) and (r). Inserting in both equations the expression for the flow rate at high pressure drop (4.32), leads to the following relation for the effective threshold

$$\Delta P^* = P_\tau + \frac{1}{2}\left(\Delta P^{*(l)} + \Delta P^{*(r)}\right) \tag{4.36}$$

Being $\Delta P^{*(l)}$ and $\Delta P^{*(r)}$ independent random variables, coming from separate subtrees, the average of (4.36) over many disorder realizations finally reads $\overline{\Delta P^*} = t\overline{P_\tau}$.
An estimation of the pressure drop $\Delta P_{\rm sat}$, at which the crossover between the nonlinear regime of Equation (4.31) and the linear regime of Equation (4.32) occurs, is obtained, as in Section 4.1, by matching the effective permeability at low pressure, $d\overline{Q_t}/d\Delta P \sim \exp(\beta_c(\Delta P - \Delta P_{\min}))/t$, with the value $1/2$ at high pressure:

$$\Delta P_{\rm sat} = \Delta P_{\min} + \beta_c^{-1} \ln t. \tag{4.37}$$

Imposing the pressure drop (4.37) in Eq. (4.30), we find that the number of open channels at the saturation pressure is $\sim t$. This means in other words that,

starting from $\Delta P_{\min}$ and increasing the pressure slightly more ($\sim \ln t$), it is enough to have $\sim t$ channels with very small overlap between them and to reach the total permeability κ. Unlike the case of independent channels, where all channels were already open at $\Delta P_{\rm sat}$ expressed in Eq. (4.19), the fraction of open channels is very small compared to the total number of channels 2^{t-1}. At even larger pressure, the fluid flows indeed in more and more channel, but this does not affect much the permeability of the network.

4.2.4 Numerical simulations on the Cayley tree

To check these results, we carried out exact numerical simulations on the Cayley tree. The algorithm we use for finding the critical pressure drops $\Delta P_c^{(0)}, \Delta P_c^{(1)}, \Delta P_c^{(2)}, \ldots$ is a simplified version of a general algorithm valid for the flow of a Bingham fluid in any directed network, which is illustrated in the supplementary material of [32]. In practice, the critical pressure drop $\Delta P_c^{(0)}$ is computed as the ground state of the associated directed polymer model via a minimization algorithm, while the following pressures are found with an iterative procedure. At each step, we denote by $\mathcal{C}_s$ the subtree made only from the channels which are open at $\Delta P \in [\Delta P_c^{(s)}, \Delta P_c^{(s+1)}]$ (where $\Delta P_c^{(s+1)}$ is not yet determined). Then:

1. Using Kirchhoff's equations, we determine the pressure at each node of $\mathcal{C}_s$ as a function of the applied pressure drop ΔP. These functions are linear in ΔP, since the flow rate (4.20) is linear in every open tube.

2. We find all the subtrees connected to a node in $\mathcal{C}_s$ which are still closed. In figure 4.2.3 they are highlighted by ovals.

3. For each subtree, we find its ground state, which we denote by $\mathcal{E}_{[1]}^{(s)}, \mathcal{E}_{[2]}^{(s)}, \ldots$. They are indicated with dashed lines in figure 4.2.3.

4. We find the minimal applied pressure drop $\Delta \tilde{P}_{c\,[1]}^{(s)}, \Delta \tilde{P}_{c\,[2]}^{(s)}, \ldots$ at which the ground state of each subtree opens. This is done by setting the node pressure at the root of each subtree (determined in step (1) using Kirchhoff's equation) equal to $\mathcal{E}_{[1]}^{(s)}, \mathcal{E}_{[2]}^{(s)}, \ldots$.

5. The new critical pressure drop is the minimal among all subtrees, namely $\Delta P_c^{(s)} = \min_\alpha \Delta \tilde{P}_{c\,[\alpha]}^{(s)}$, and the corresponding channel will open.

We stop at $t = 23$ due to the exponential growth in t of the number of configurations on the Cayley tree.
From these simulations, it comes out that the flow curve as function of the pressure is a piece-wise linear function, with breakpoints at the critical pressure drops $\Delta P_c^{(0)}, \Delta P_c^{(1)}, \ldots, \Delta P_c^{(n^{ch})}$. For each segment, the flow is linear and reads $Q_t(\Delta P) = \kappa_{\rm eff}(\Delta P - \Delta P_{\rm eff}^*)$. The first parameter, $\kappa_{\rm eff}$, is the permeability of the set of channels that have been opened up to that pressure, while $\Delta P_{\rm eff}^*$ depends on the threshold along them. In Fig. 4.2.4, we study their behavior as a function of $n^{\rm ch}$. In particular, in Fig. 4.2.4 middle, we observe that the permeability grows quickly with $n^{\rm ch}$ and after $n_{\rm SAT}^{\rm ch} \sim t$ reach the value $\kappa = 1/2$ (see inset of Fig. 4.2.4 middle). This rapid growth is not seen for $\Delta P_{\rm eff}^*$ which increases slowly with $n^{\rm ch}$ as shown in Fig. 4.2.4 right.

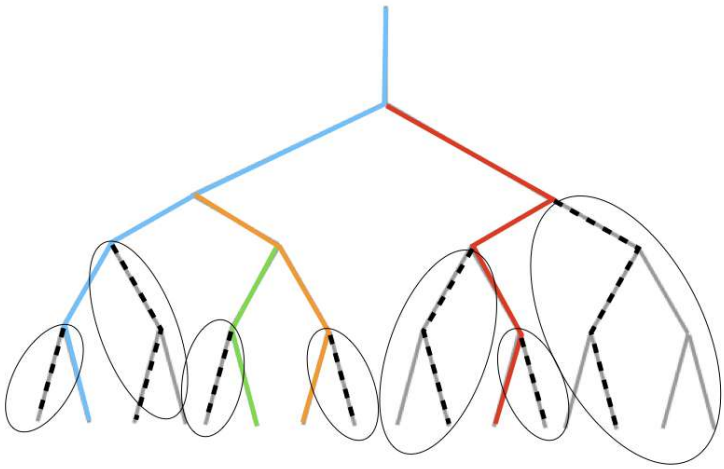

Figure 4.2.3: Sketch of the algorithm used for the exact solution of the flow in the Cayley tree. The colored channels indicates the paths already opened. The ovals highlights the subtrees which are still closed, in which the related ground state is marked with a dashed line.

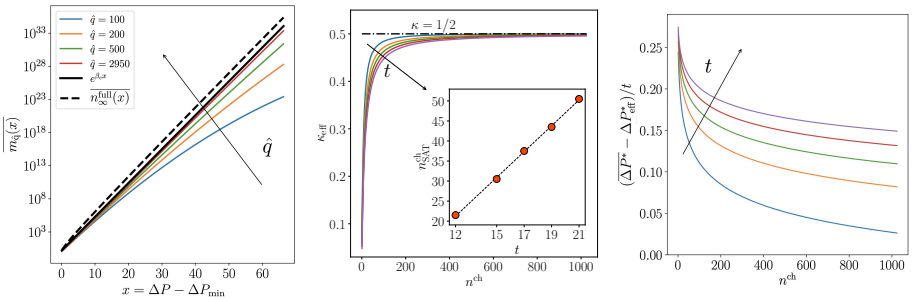

Figure 4.2.4: Left: $\overline{m_{\hat{q}}(x)}$ and $\overline{n_\infty^{\rm full}(x)}$ (dashed black line) obtained by numerical integration of Eq.(B.10) and Eq.(B.11) with different initial conditions. Middle and Right: exact numerical simulations on finite Cayley tree of moderate moderate sizes $t = 12, 15, 17, 19, 21$. The opening of the first $\sim t$ channels is sufficient to saturate the effective permeability, $\kappa_{\rm eff}(n_{\rm SAT}^{\rm ch}) = 0.4 = 0.8\kappa$ (inset). However $\Delta P_{\rm eff}^*$ displays a much slower evolution and it is still far from the saturation value $\overline{\Delta P^*}$ when $n^{\rm ch} \sim 1000 \gg t$. The simulations were carried out using a Gaussian distribution $\Pi(P_{\tau_c})$ with zero mean and variance $\sigma^2 = 1/12$. The corresponding value for β_c from (4.29) is $\beta_c = \sqrt{2 \ln 2}/\sigma$.

CHAPTER

FIVE

TRANSITION FROM VISCOUS FINGERS TO FOAM IN A PORE NETWORK

A numerical study of a transition from viscous fingering displacement to foam during drainage in heterogeneous porous media is illustrated in this Chapter. Concerning drainage scenarios, the literature extensively delves into distinct examinations of continuous displacement on the one hand, and foam flow on the other hand, as explained in Section 2.2. Nevertheless, it is reasonable to expect the existence of a transition between these two regimes during two-phase flow. If a constant pressure drop is imposed on the system, the emergence of capillary or viscous fingering results in an increase of the overall flow rate, and in a transformation of the pressure gradient along the flow direction. Considered that a minimum injection flow rate or pressure gradient is required for generating foam in the medium, it is possible that a fingering regime may develop into a foam displacement scenario. As illustrated in a recent paper which motivated the present investigation [78], a transition from a compact displacement to viscous fingering was observed experimentally. The authors observe that in a radial configuration with an imposed pressure drop, the invasion occurs through a stable front, and the advancing pattern displays an intense blob dynamic, typical of foam. However, beyond a certain radial distance, the front transitions into a shape resembling viscous fingering. It's worth noting that when injecting fluid at a constant flow rate in this radial setup, the front velocity naturally decreases due to mass conservation. If the formation of foam requires a critical velocity, it is plausible that foam generation might cease after reaching a certain distance. This transition can be seen as the mirror case of the one found in our investigation.

In this context, it's also important to highlight that when considering the Darcy scale, where the porous material can be viewed as a continuous medium, the fractal patterns formed by continuous front flow, such as viscous fingers, become negligible in terms of their spatial extent. It is foam-like structures, which lack fractal characteristics, that lead to saturation variations at these scales.

In Section 5.1 we illustrate the pore network model we adopt for our numerical simulations. In particular, we provide the basic equations governing the fluid displacement at the pore level, and we explain the rules we adopt for redistributing both fluids at the nodes. The results collected are shown, analyzed and discussed in Section 5.2.

In brief, when the flow is driven by a constant pressure difference ΔP between the inlet and the outlet, the displacement front can exhibit a transition from a viscous fingering regime to a foam-like region. When this happens, the transition occurs at a certain distance from the inlet Λ, which is observed to be independent with time, from the moment the first foam is formed. We measure Λ as a function of the ratio between the non-wetting and wetting viscosities, μ_n/μ_w and of the ratio between the pressure applied and the typical capillary pressure drop, $\Delta P/P_\gamma$, obtaining that it scales as a power-law with both parameters

$$\Lambda \propto (\Delta P/P_\gamma)^{-\alpha}(\mu_n/\mu_w)^{-\beta}. \tag{5.1}$$

The exponents α e β are measured, also for different distributions of the tube radii.
The total flow rate Q is observed to be evolving in time, in particular passing from an exponential increase in the fingering regime to an inflection when foam is formed. The inflection is stronger for lower values of the ratio $\Delta P/P_\gamma$. The reduction of the increase of Q is associated to a loss of global mobility, typical of strong foam. At the same time, the local pressure gradient in the medium displays an increase in the same area where foam is located. This is due to the presence of numerous menisci randomly located in the pore throats, and that explains the mobility loss.
Furthermore, the flow velocity during these drainage events is not homogeneous but localized in few channels, both in the viscous fingers and in the foam region, although in the latter the channels tends to divide into several smaller ones. This leads to very different behaviour of the local flow rate in the fingers region, where the fluctuations are mostly stable in time, from the foam region, where the value drops intermittently to zero. The Fourier analysis suggest that the first resemble a Brownian motion, while the second an anti-correlated (pink) signal.

5.1 Methods

Simulations were carried out in the framework of dynamic pore-network modeling (see Section 2.3.2). The pore network we consider here has an underlying geometry of a regular square lattice of $N_x \times N_y$ links as shown in Figure 5.1.1, which is tilted by an angle of 45° with the direction of the global pressure drop. Instead of separating the pore bodies from the throats, this network consists of *composite links*, which means that each link contains a narrow pore throat in between two wider pore bodies. This is modeled by having links with varying radius along its length, similar to an hourglass shape. The total porous space of the network is therefore contained by all the links, and the nodes represent only the positions of the intersections of the links. We consider all links with identical length l, and presenting axial symmetry. The disorder is then introduced in the characteristic radius r_0 of the links. Two different distributions for $r_0 > 0$ are considered:

- Uniform distribution

$$\Pi(r_0) = \begin{cases} 1/a & \text{if } r_0 \in [\overline{r_0} - a/2, \overline{r_0} + a/2] \\ 0 & \text{otherwise} \end{cases}; \tag{5.2}$$

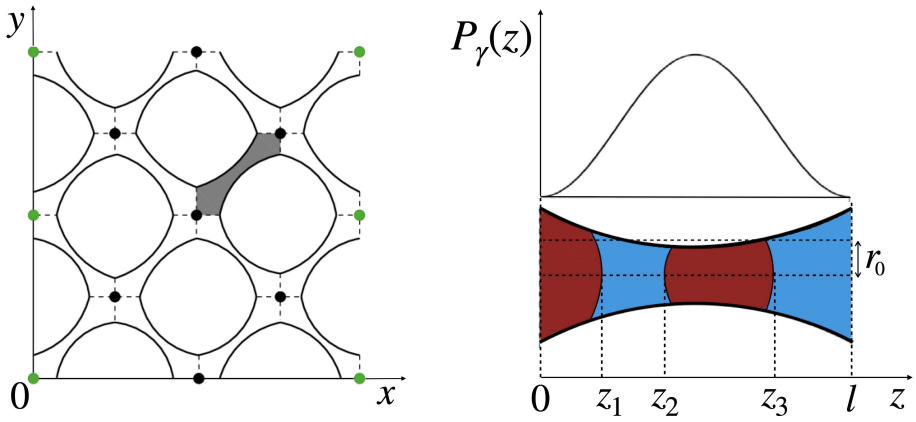

Figure 5.1.1: Left: Illustration of a pore network made by $N_x \times N_y = 4 \times 4$ links. The hour-glass shaped links are connected to each other at nodes denoted by circular dots. Because of the periodicity, green dots at the same height represent the same node. One of the links is colored gray. Right: Illustration of a single link filled with two fluids, separated by different interfaces (menisci). The blue and red color represent the wetting and non-wetting fluid, respectively. The capillary pressure drop for an interface, expressed by equation (5.4), is shown above the link, where $P_\gamma(z)$ is plotted as a function of the interface position $0 < z < l$.

- Rayleigh distribution

$$\Pi(r_0) = \frac{r_0}{\overline{r_0}^2} e^{-r_0^2/(2\overline{r_0}^2)}; \tag{5.3}$$

here, $\Pi(r_0)$ is the corresponding PDF, $\overline{r_0}$ is the average radius and a is the interval width for the uniform distribution.

We restrict to low Reynolds numbers, and we assumed that the radius does not deviate too much from its characteristic value $r_{0,ij}$ of the link. In this case, the Poiseuille equation can apply when one Newtonian fluid is present in the tube. In case of two immiscible and incompressible fluids present in the same link, the Poiseuille equation needs to be modified [108]. First, the viscosity μ will be the effective viscosity $\mu_{ij} = \mu_n S_{ij} + \mu_w(1 - S_{ij})$. Here S_{ij} is the local non-wetting saturation, namely the fraction of the link length occupied by the non-wetting fluid, while μ_n and μ_w are respectively the non-wetting and wetting viscosities. Second, there is a capillary pressure drop P_γ across the meniscus separating the two fluids that must be taken into account. As the links of the network have a varying radius along their length, P_γ will depend on the position of a meniscus. For the converging-diverging type of an hourglass-shaped link, we model the variation of the capillary pressure with the position $0 < z < l$ of a meniscus by a modified Young-Laplace law [109, 85],

$$|P_\gamma(z)| = \frac{2\gamma}{r_{0,ij}} \left[1 - \cos\left(\frac{2\pi z}{l}\right)\right] , \tag{5.4}$$

where $\gamma = \hat{\gamma}\cos\theta$, $\hat{\gamma}$ being the surface tension between the two fluids and θ the contact angle between the meniscus and the link wall, which is supposed not to

vary during the motion. With these two modifications, the Poiseuille equation for a number of m menisci inside a link can be generalized as,

$$Q_{ij} = \frac{\pi r_{0,ij}^4}{8\mu_{ij} l} \left[P_i - P_j - \sum_{k=1}^{m} P_\gamma \left(z_k \right) \right] , \tag{5.5}$$

where the summation is over all the interfaces $k = 1, \ldots, m$, inside the link, taking into account the direction of the capillary forces.

To reproduce drainage displacements, we initially fill completely the network with the wetting fluid, and then we inject the non-wetting fluid at the inlet, consisting in the edge of the network at $y = 0$. From the outlet at the opposite edge, at $y = N_y$, fluids can leave the network. As we perform the simulations at a constant pressure drop ΔP, we impose fixed pressure values P_{in} and P_{out} at all the inlet and outlet nodes respectively, such that $\Delta P = P_{\text{in}} - P_{\text{out}}$. The pressure gradient occurs then in the direction going from the inlet to the outlet edge. The two lateral edges of the network parallel to the direction of pressure drop are connected using periodic boundary condition.

Since both fluids are incompressible, as explained in Section 2.3.2, the equivalent of the Kirchhoff law for the electrical current can be adopt, which we report in the following:

$$\sum_{j \in \text{ngb}(i)} Q_{ij}(t) = 0 , \tag{5.6}$$

where $j \in \text{ngb}(i)$ are the neighboring nodes connected to the node i by links. This provides a closed set of linear equations which, once solved, allows to compute both the local node pressures $\{P_i(t)\}$ and the flow rates $\{Q_{ij}(t)\}$ for the whole network. From the local flow rates we update the positions of each menisci in the system, displacing it by a distance

$$\Delta z_{ij} = \frac{\Delta t \, Q_{ij}}{\pi r_{0,ij}^2} \tag{5.7}$$

in the direction of the local flow. Here the time step Δt is chosen in such a way that the largest displacement of any meniscus in any link does not exceed $0.1\, l$ in one time step.

To distribute fluids from links to their neighboring links at the links intersections or nodes, we consider an algorithm that does not impose any restriction on the blob sizes inside any link, and for which the blob sizes are determined by the dynamics of the flow [93]. This makes it possible for the model to generate not only the continuous capillary or viscous fingers but also foams with smaller blobs. The model can therefore capture the transition from fingering to foam formations while changing external flow parameters, and no alteration in the fluid distribution algorithms is necessary. The algorithm first calculates the total volume of fluids $V_i = -\sum_j Q_{ij} \Delta t$ that each node i receives from the incoming neighboring links, namely the links for which $Q_{ij} < 0$ for a node i according to equation 5.5. The individual values of the wetting and non-wetting volumes V_i^w and V_i^n that the node receives from the incoming links are calculated from the displacements of the menisci following equation 5.7. The two fluid volumes are then redistributed to the outgoing neighboring links, the links for which $Q_{ij} > 0$ for any node i. The redistribution follows an impartial rule where the ratio between the total injected

volumes of fluids V_{ij} in different outgoing links is equal to the ratio between the flow-rates Q_{ij} in those links, and the ratio between the volumes of wetting (V_{ij}^w) and non-wetting (V_{ij}^n) fluids in each individual outgoing link is proportional to the incoming wetting and non-wetting volumes V_i^w and V_i^n in the distributing node. This is done by creating new wetting and non-wetting blobs of volume $V_{ij}^w = Q_{ij}\Delta t V_i^w/V_i$ and $V_{ij}^n = Q_{ij}\Delta t V_i^n/V_i$ respectively in every outgoing link of node i. The order of the new wetting and non-wetting droplets are chosen arbitrary. Furthermore, when the number of the blobs exceeds a maximum limit in a link, we merge two nearest blobs keeping the volume conserved, but without detaching any blob attached to a node which may be a part of a cluster spanned over several links.

In summary, at every time step Δt, we calculate the local pressures P_i for each node and flow rates Q_{ij} in each link by solving equations 5.5 and 5.6, then update the positions of the menisci using equation 5.7. The fluids are then exchanged between different links which in general alters the local non-wetting saturation S_{ij} in the links, as well as the number and positions of the menisci. This necessitates the linear system of equations (5.5) and (5.6) to be solved again in the next time step.

As discussed in Section 2.2, the main competing mechanisms that control the flow characteristics in two-phase Newtonian flow are the viscosity ratio and the capillary number. The viscosity ratio can be defined as $M = \mu_n/\mu_w$, whereas the capillary number is generally defined for the flow driven under the constant flow rate Q as [110, 111, 109],

$$\mathrm{Ca}_Q = \frac{\mu_w Q}{\gamma \Sigma}\ , \tag{5.8}$$

where $\Sigma = N_x \pi \overline{r_0}^2$ is the average cross-sectional area of the pore network. However, when the system is driven under a constant pressure drop ΔP as we are studying here, the total flow rate Q varies with time. The capillary number is therefore defined as a function of the pressure drop [112],

$$\mathrm{Ca}_P = \frac{\Delta P/N_y}{2\gamma/\overline{r_0}}. \tag{5.9}$$

where $\Delta P/N_y$ is the average pressure drop across one link and $2\gamma/\overline{r_0}$ is the typical capillary pressure drop for a meniscus in a link. These two dimensionless numbers fully characterize the invasion displacement. This means in particular that different simulations with the same values of M and Ca_P will produce invasion patterns which are statistically equivalent. In Appendix D we show the validity of this statement.

5.2 Results

Figure 5.2.1 displays the evolution in time of a typical invasion front with $M = 10^{-2}$, $\mathrm{Ca}_P = 0.25$ and r_0 uniformly distributed. Unless indicated otherwise, the results presented will correspond to a lattice of size $N_x \times N_y = 200 \times 200$. Here, we describe the evolution of our system using the normalized injected pore volume $\mathrm{IPV} = V_{\mathrm{inj}}/V_{\mathrm{tot}}$, where V_{inj} is the volume of the injected fluid and V_{tot} is the volume of the total pore space of the network. Initially, the non-wetting phase enters in

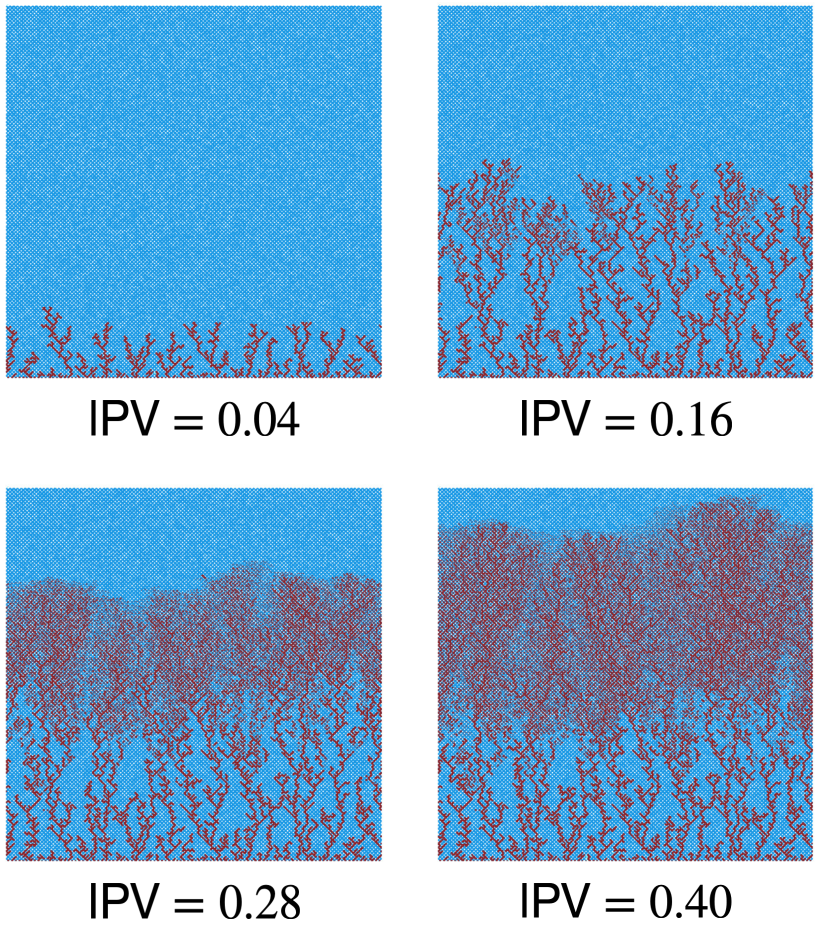

Figure 5.2.1: Snapshots at different growing values of the injected pore volume (IPV). The blue and red color represent the wetting and non-wetting fluid, respectively. We observe a transition from viscous fingering to foam at a certain distance from the inlet. For this simulation we set $\mathrm{Ca}_P = 0.25$, $M = 10^{-2}$, and r_0 generated according to the uniform distribution (5.2) with $\overline{r_0} = 0.25\,l$ and $a = 0.15\,l$.

the porous medium and exhibits the common viscous fingering occurring at high flow rate [58]. At this early stage, the non-wetting fluid remains continuous in the absence of any breakage. Also, we note that the invaded pores are never occupied again by the wetting phase. However, as the fingers advances through the network, we observe that the continuous non-wetting fingers eventually break up and the invading pattern exhibits a very different foam-like structure composed of many small droplets. Notably, this transition between the continuous viscous fingers to the foam regime appears at a certain distance Λ from the inlet that depends on both the capillary number Ca_P and viscosity ratio M. We will analyse this in detail in the following Subsection.

Figure 5.2.2 represents a diagram of the invasion pictures at breakthrough, namely when the invading fluid reaches the outlet, for different viscosity ratios and capillary numbers for which the transition is observed. It can be noted that the distance of occurrence of the transition decreases with both the capillary number and the viscosity ratio. Both trends can be qualitatively understood. As discussed in Section 2.2.2, a certain critical pressure drop is required to generate foam. During an invasion process, we can conjecture that the foam is generated in the vicinity of the invasion front, so we should consider the pressure drops across the links close to the front and consider their evolution during the invasion. We remind that we keep the pressure drop between the inlet and the outlet fixed, and since we are injecting a fluid that has much lower viscosity than the defending fluid, the pressure gradient across the non-invaded part of the system increases as the front advances. The local pressure drops across the throats located just after the front will therefore increase as well, explaining why foam is triggered only after the front reaches a certain distance from the inlet. Moreover, the pressure gradient rises with both the parameters Ca_P and M. Increasing either the capillary number or the viscosity ratio should then trigger the foam at a shorter distance from the inlet. One might guess that the height of the location of foam generation decreases with the inverse of both the capillary number and the viscosity ratio, namely $\Lambda \propto \mathrm{Ca}_P^{-1}$ and $\Lambda \propto \mathrm{M}^{-1}$. However, as we will see in the next Subsection, where we present a method to characterize and analyze the transition distance Λ, this is not the case.

5.2.1 Characterization of the fingering-to-foam transition distance Λ

To analyse the transition from viscous fingering to foam, we first need to define a method that differentiates the two regions. For this, we define a quantity $t_{ij} = |S_{ij} - 1/2|$ for every link. This is because, for a continuous displacement pattern, this quantity should be equal to $1/2$, as every link will be fully saturated by either of the two fluids and S_{ij} will be either 0 or 1. Then, t_{ij} will differ from $1/2$ for a link when it is occupied by both the fluids. To define Λ, we then average this quantity in the direction transverse to the overall flow for a certain normalized distance from the inlet y/l and find a quantity $T(y/l)$ given by

$$T(y/l) = \frac{1}{N_x} \sum_{x=1}^{N_x} \left| S_{ij} - \frac{1}{2} \right|. \tag{5.10}$$

In order to decrease the noise, we average $T(y/l)$ for a given IPV over different realizations of the disorder given by different radii configurations, and we refer

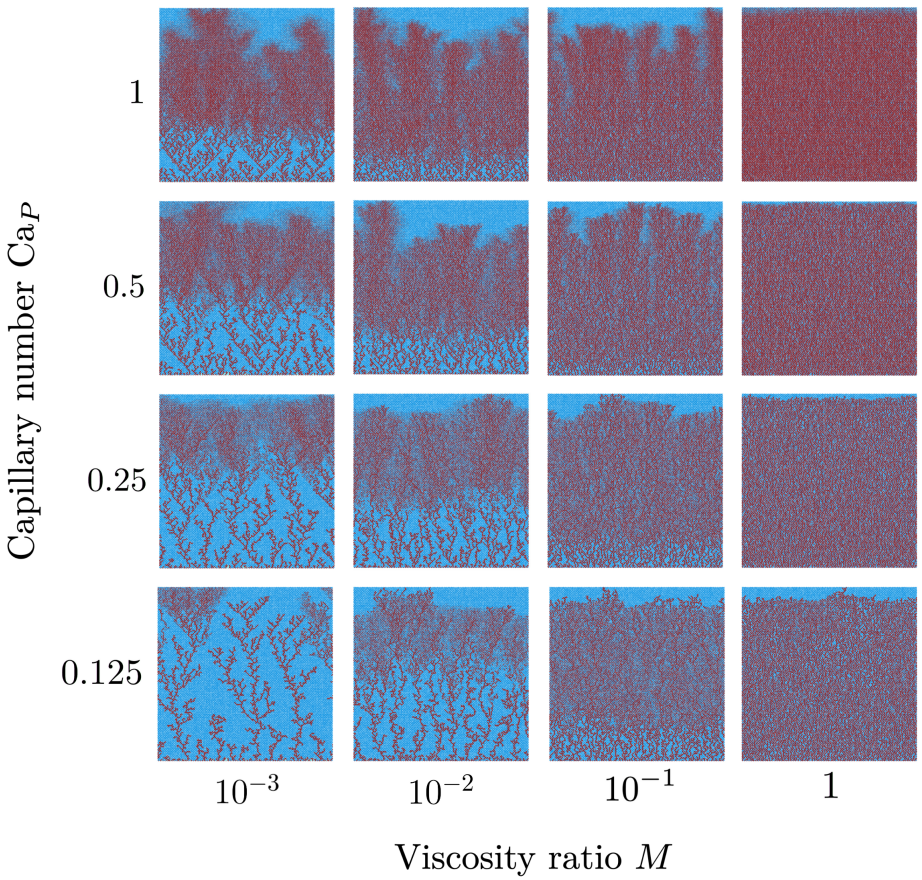

Figure 5.2.2: Diagram of the invasion patterns at breakthrough for different viscosity ratio and capillary number. The blue and red color represent the wetting and non-wetting fluid, respectively. For these simulations r_0 is generated according to the uniform distribution (5.2) with $\overline{r_0} = 0.25\,l$ and $a = 0.15\,l$.

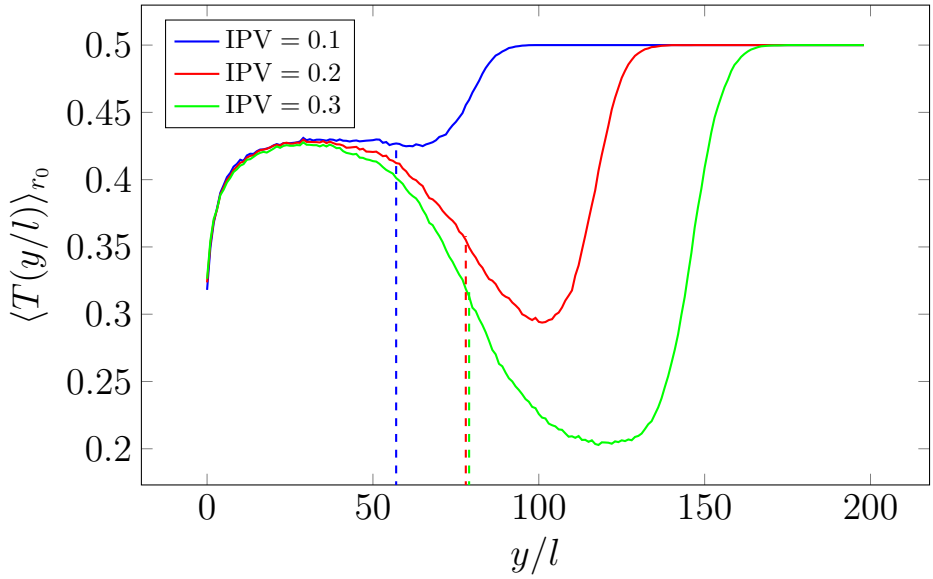

Figure 5.2.3: Plot of $\langle T(y/l)\rangle_{r_0}$, defined in equation (5.10), for different growing IPV. For these simulations we set $\mathrm{Ca}_P = 0.25$, $M = 10^{-2}$, and r_0 uniformly distributed according to equation (5.2) with $\overline{r_0} = 0.25\,l$ and $a = 0.15\,l$. Each vertical dashed line indicates the position of the minimum of the derivative of the curve of the corresponding color, which defines Λ for that IPV.

to this average as $\langle T(y/l)\rangle_{r_0}$. For all the simulations studied, unless specified otherwise, the average is done over 100 realizations of the radii disorder.

The typical trend of $\langle T(y/l)\rangle_{r_0}$ for different IPV is shown in Figure 5.2.3. For all IPV, and after a short distance from the inlet ($y/l \gtrsim 10$ in the figure), $\langle T(y/l)\rangle_{r_0}$ reaches a high value plateau ($\langle T(y/l)\rangle_{r_0} \simeq 0.42$ in the figure). This corresponds to the viscous fingering region, where most of the links are saturated by either one of the two fluids. Beyond this plateau, two trends are observed depending on IPV. At lower IPV, before the start of foam formation, there is no decrease in the value of $\langle T(y/l)\rangle_{r_0}$, since it increases directly to a higher plateau value 0.5. This value represents the regions fully saturated by the wetting fluid. At higher IPV, $\langle T(y/l)\rangle_{r_0}$ undergoes a significant decrease that characterizes the onset of foam, before reaching again the plateau at 0.5. From this curve, we define the value Λ as the position of the minimum of the curve's derivative, as illustrated in Figure 5.2.3.

In Figure 5.2.4 (left), Λ versus IPV is plotted for different combinations of the capillary number Ca_P. After an initial transient interval, Λ reaches a plateau, where it maintains a constant average value until breakthrough. This value at the plateau depends on Ca_P, and in particular, for higher Ca_P, the Λ plateau is lower and attained sooner. This reflects that the onset of foam formation happens at earlier stage of invasion with increasing values of Ca_P, as observed in Figure 5.2.2. The plateau value, Λ_{sat}, is then calculated averaging Λ from the end of the transient interval until the breakthrough. In Figure 5.2.4 (right), we plot the plateau value Λ_{sat} as a function of Ca_P for the two types of radii distribution, uniform and

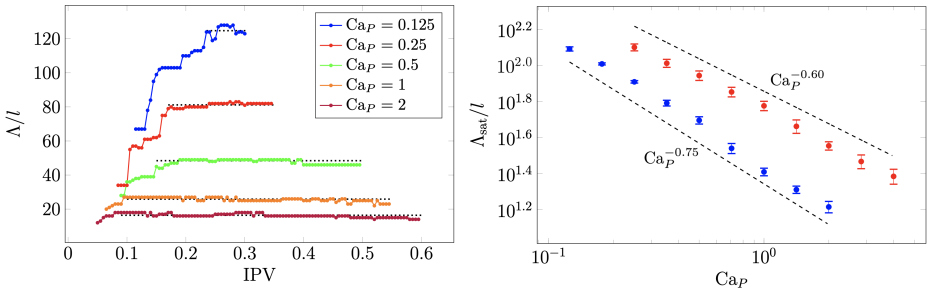

Figure 5.2.4: Left: Plot of Λ/l as a function of IPV for different Ca_P, setting $M = 10^{-2}$ and uniformly distributed according to Eq. (5.2) with $\overline{r_0} = 0.25\,l$ and $a = 0.15\,l$. Λ reaches a plateau value Λ_{sat}/l, indicated by an horizontal dotted line, which is determined by averaging the values after reaching the plateau. Right: Λ_{sat}/l for different values of Ca_P. Blue dots correspond to simulations with $M = 10^{-2}$ and r generated according to the uniform distribution (5.2) with $\overline{r_0} = 0.25\,l$ and $a = 0.15\,l$. Red dots correspond to simulations with $M = 10^{-2}$ and r_0 generated according to the Rayleigh distribution (5.3) with $\overline{r_0} = 0.1\,l$; their trend $\propto \mathrm{Ca}_P^{-0.75}$ is represented by a dashed-dotted line. The error bars represent the standard deviation related to the values of Λ/l averaged to obtain Λ_{sat}/l. The dashed lines shows the trends found with a weighted fit of the data.

Rayleigh. We observe a non-trivial power law decay of $\Lambda_{\mathrm{sat}} \propto \mathrm{Ca}_P^{-\alpha}$. A weighted fit of the data obtained from the uniform radii distribution gives $\alpha \simeq 0.75 \pm 0.03$, while from the data from the Rayleigh radii distribution we have $\alpha \simeq 0.60 \pm 0.05$. The two trends are represented in Figure 5.2.4 (right) with dashed lines. It is worth noting that the simple prediction $\alpha = 1$ discussed in the previous section is invalidated.

The time evolution of Λ as function of the viscosity ratio M is shown in Figure 5.2.5 (left). Here also, Λ reaches a plateau, where the value at the plateau Λ_{sat} decreases with the increase of M as seen in Figure 5.2.2. We find that Λ_{sat} follows a power-law, $\Lambda_{\mathrm{sat}} \propto M^{-\beta}$. For the Rayleigh distribution, a weighted fit for all the data collected returns a power-law $\beta \simeq 0.31 \pm 0.03$. For the uniform distribution, a crossover between two different trends was observed at $M \simeq 10^{-2}$. For the data in the interval $[2.5 \cdot 10^{-3}, 10^{-2}]$ the fit gives $\beta \simeq 0.25 \pm 0.04$, while in the interval $[\sqrt{2} \cdot 10^{-2}, 8 \cdot 10^{-2}]$ we measured $\beta \simeq 0.40 \pm 0.06$. In Figure 5.2.5 (right) these trends are highlighted with dashed lines.

The independence of the power law exponents, found for both Ca_P and M, on the radii distribution remains an open question. Recently, it was reported in literature that steady state rheology of two-phase flow depends in general on the pore size distribution. In particular, some physical quantities can vary when changing the shape of the distribution, but remaining constant if we change only the distribution width while keeping the same shape, and vice versa [86]. Here, it seems that the power law is not independent from the type (so, the shape) of the radii distribution chosen, since the values of the exponents measured for the two distributions don't present a good reciprocal compatibility within the error. On the other hand, we have observed that Λ remains constant when keeping the same type of distribution and changing only its width (see the Appendix D).

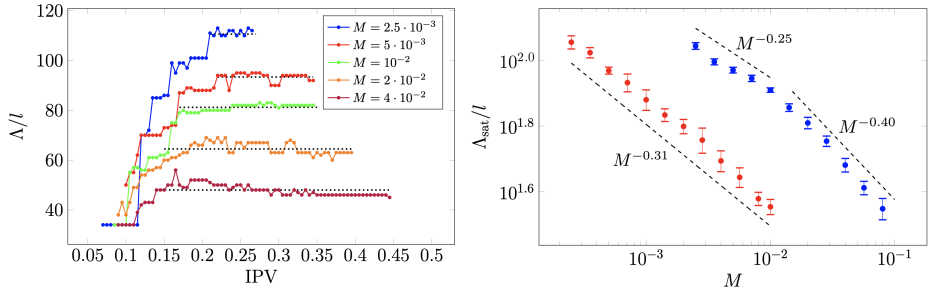

Figure 5.2.5: Left: Plot of Λ/l as a function of IPV for different M, with $\mathrm{Ca}_P = 0.25$ and r_0 uniformly distributed according to Eq. (5.2) with $\overline{r_0} = 0.25\,l$ and $a = 0.15\,l$. Λ reaches a plateau value Λ_{sat}/l, indicated by an horizontal dotted line, which is determined by averaging the values after reaching the plateau. Right: Λ_{sat}/l for different values of M, Blue dots correspond to simulations with $\mathrm{Ca}_P = 0.25$ and r generated according to the uniform distribution (5.2) with $\overline{r_0} = 0.25\,l$ and $a = 0.15\,l$. Red dots correspond to simulations with $\mathrm{Ca}_P = 1$ and r generated according to the Rayleigh distribution (5.3) with $\overline{r_0} = 0.1\,l$. The error bars represent the standard deviation related to the values of Λ/l averaged to obtain Λ_{sat}/l. The dashed lines shows the trends found with a weighted fit of the data. $M^{0.31}$

Now that we have quantified the location of the foam generation, in the following we investigate its influence on the total flow rate.

5.2.2 Total flow rate

Figure 5.2.6 shows the temporal evolution of the Q-based capillary number Ca_Q, defined in equation (5.8), for different values of Ca_P. Since it is directly proportional to Q, Ca_Q can be thought as a dimensionless flow rate. Moreover, being the global pressure drop fixed throughout the evolution of the system, the total flow rate for a given IPV can be interpreted as the global permeability of the system. For all Ca_P, initially the flow rate increases due to the viscous fingering instability, as we replace a more viscous fluid with a less viscous one. For later values of IPV, however, we observe an inflection point, which corresponds to the emergence of foam. This inflection is more pronounced with lower values of Ca_P. For the lowest capillary numbers studied, the flow rate even seems to be non-monotonic. This is an indication that the generated foam has a very low mobility, which is a typical characteristic of strong foam [67, 68]. Interestingly, we note that, at very low capillary number, the dispersion of the data, represented in Figure 5.2.6 by their standard deviation, becomes very high when the front is close to the outlet.

To better investigate this decrease of mobility, we looked at the evolution of the gradient of pressure along the flow direction. To do this, we average the absolute values of the local pressure drop $dP_{ij} = P_i - P_j$ along the x-direction:

$$|dP_x|(y/l) = \frac{1}{N_x} \sum_{x=1}^{N_x} |dP_{ij}|. \tag{5.11}$$

Figure 5.2.7 (left) shows the time evolution of the normalized quantity $\langle |dP_x| \rangle_{r_0} / (2\gamma/\overline{r_0})$

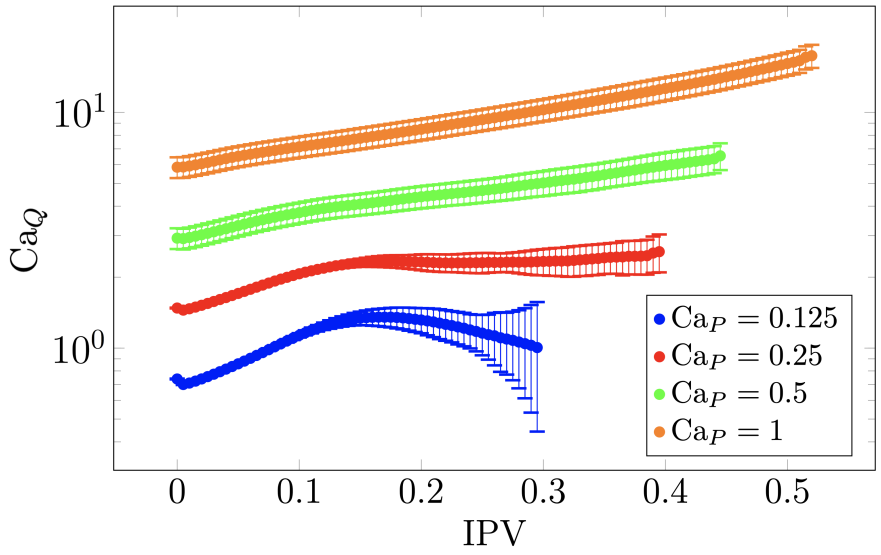

Figure 5.2.6: Plot of the dimensionless flow rate Ca_Q, defined in equation (5.8), as a function of IPV, averaged over 1000 realizations of the radii disorder, and for different values of Ca_P. The error bars represent the standard deviations of the values collected from the different realizations of the disorder given by the radii configurations. For these simulations we set $M = 10^{-2}$ and r_0 uniformly distributed according to equation (5.2) with $\overline{r_0} = 0.25\,l$ and $a = 0.15\,l$.

averaged over different realizations of the radii disorder. Close to the inlet (for $y/l \lesssim 20$), the value is quite high because of our injection condition, where many links contain a meniscus. Further, the gradient of pressure first decreases reaching a minimum, and then increases again to reach a plateau value. The lower value region corresponds to the viscous fingering region, where the pressure drop is localized in few channels of low viscosity. The higher plateau closer to the outlet corresponds instead to the region saturated with the defending viscous fluid, hence the higher value. Moreover, as discussed previously, the plateau value increases as the invasion front advances.

Nevertheless, the most important feature is the appearance of a bump after a certain IPV, between the minimum and the plateau, whose height and width increase as time goes by. This bump corresponds to the foam region, which decreases significantly the mobility of this region. A few observations can be made in this regard. First, the bump starts growing at approximately the same position for different IPV. The location of foam onset is thus approximately independent of time, which confirms the stability of the foam generation location. This pressure gradient measurement could thus have been used as an alternative method to quantify Λ. Second, the fact that the bump is higher than the plateau indicates that the mobility of the foam is less than that of the more viscous fluid, despite the foam being highly saturated with less viscous one. This effect is then linked to the presence of menisci in the foam. To quantify the impact of capillarity, we calculate the average of the capillary pressure drops, namely $dP_{\gamma,ij} = dP_{ij} - 8\mu_{ij}Q_{ij}/(\pi r_{0,ij}^4)$

from eq. (5.5), along the x-direction:

$$|dP_{\gamma,x}|(y/l) = \frac{1}{N_x}\sum_{x=1}^{N_x}|dP_{\gamma,ij}|. \tag{5.12}$$

In Figure 5.2.7 (right) the time evolution of the normalized quantity $\langle|dP_{\gamma,x}|\rangle_{r_0}/(2\gamma/\overline{r_0})$ is shown. Initially, we observe a monotonic decrease between the inlet and outlet, with a sharp drop outlining the displacement front. At a certain time, a capillary pressure bump appears, which is due to foam generation and the occurrence of several menisci. We note that this bump has approximately the same magnitude and evolution as in the previous one, which confirms that mobility loss is mainly due to the presence of many menisci in this region. Another interesting feature is that the curves at different IPV seem to collapse behind the front, just before the onset of the foam, around a local minimum.

5.2.3 Foam generation in the pore network

In the previous Subsection, we have quantified the occurrence of strong foam and its consequence on the total flow rate. In the introduction, we discussed a crude argument for foam generation which would occur because the gradient of pressure increases at the tip. However, from this argument one would expect that the location of Λ decreases like Ca_P^{-1} or M^{-1}, which is not the case. Moreover, by considering the pressure gradient for different combinations of the parameters, we were not able to identify a clear threshold value of the local pressure drop for the onset of foam. To further analyse the mechanism of foam generation, we show details of few snapshots of very early foam generation in Figure 5.2.8 (upper row). We observe that foam is not necessarily generated at the tip of the front. Instead, blobs are produced by the fragmentation of already developed fingers located also behind the front (like for the one highlighted by the black circle in the last snapshot). In other words, branches created by the viscous fingering might be unstable and fragment at a certain location.
Together with this process of fragmentation, we note that there seems to be an interaction between different growing fingers. As depicted in Figure 5.2.8 (upper row), the fragmentation of a branch is related to the approach of another (the one below on the right side). In Figure 5.2.8 (bottom row), we present the local flow rate field corresponding to the snapshots above by plotting a dimensionless local flow rate, between two generic links i and j, defined as

$$\widetilde{Q}_{ij} = \frac{\mu_w Q_{ij}}{\pi \overline{r}^2 \gamma} \tag{5.13}$$

The figures show that the fragmentation of the branch occurs together with a decrease of the flow rate in the corresponding links. The flow rate in the approaching finger on the right remains instead approximately constant, so its value becomes higher than that of the breaking finger.
There is therefore a competition between the different branches of the invading pattern related to the emergence of foam, meaning that the fragmentation of a branch will stop its expansion, and thus favor the growth of the others. Competition between growing channel in porous media was already observed and studied,

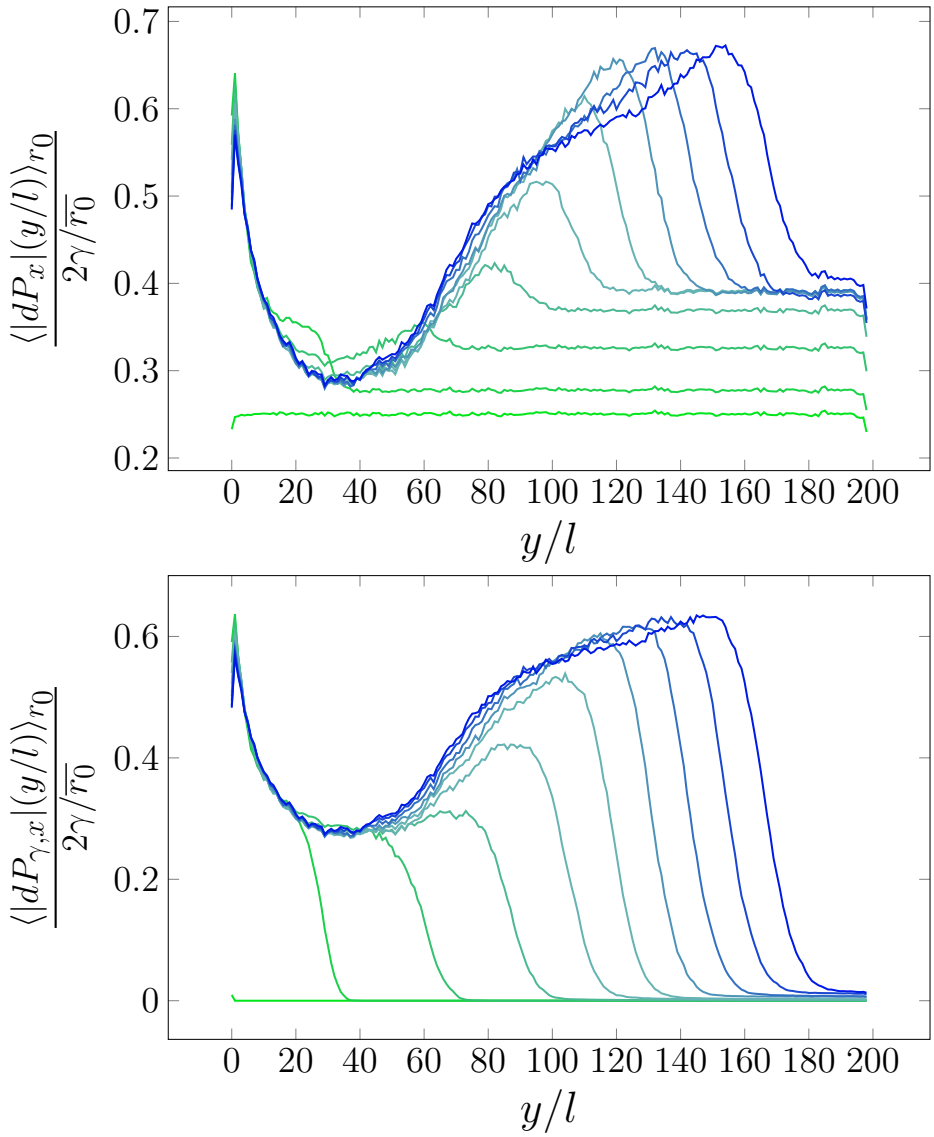

Figure 5.2.7: Left: Plot of $\langle |dP_x| \rangle_r / (2\gamma/\overline{r_0})$, as function of y-position, for different values of IPV. Different color shades represent increasing values of IPV, equally spaced from 0 (light green) to 0.4 (dark blue). The average is done over 100 different realization of the radii disorder. Right: Plot of the capillary contribution $\langle |dP_{\gamma,x}| \rangle_r / (2\gamma/\overline{r_0})$ of the pressure drop profile pictured on the right at the same IPV. For these simulations we set $\mathrm{Ca}_P = 0.25$, $M = 10^{-2}$, and r_0 uniformly distributed according to equation (5.2) with $\overline{r_0} = 0.25\,l$ and $a = 0.15\,l$.

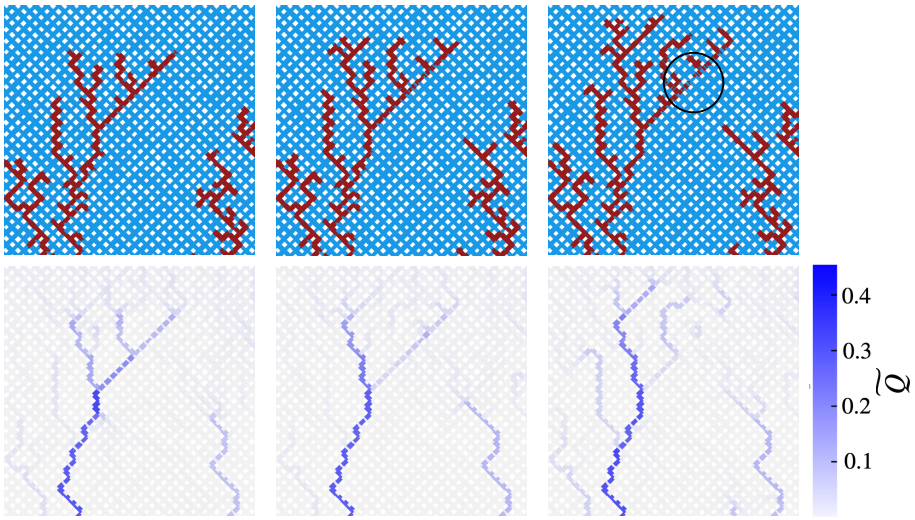

Figure 5.2.8: Foam creation in the pore network. Upper row: detail of different snapshots, at consecutive times from left to right, showing an event of foam formation. The right finger of the bigger branch fragment to create foam, highlighted with a black circle in the rightmost image. Lower row: color map of the dimensionless local flow rate $\widetilde{Q}$ defined in equation (5.13) for the respective snapshots.

also in the context of dissolution in fractured or porous rocks [113]. Furthermore, since the breakage of fingers cause its growth rate to drop significantly, there is a relationship between the creation and propagation of foam and the fluctuations observed in the local flow rate field. In the next subsection, we measure and characterize the time evolution of the local flow rate both in the finger region and in the foam region.

5.2.4 Fluctuations of local flow rate

Figure 5.2.9 illustrates the map of the dimensionless local flow rate $\hat{q}$ defined in equation (5.13) for few snapshots close to breakthrough, in a simulation setting $M = 10^{-2}$, $\mathrm{Ca}_P = 0.25$ and r_0 uniformly distributed according to equation (5.2) with $\overline{r_0} = 0.25\,l$ and $a = 0.15\,l$. As expected, in the viscous fingering region, below Λ, the flow is localized in a few, almost parallel channels, corresponding to the branches of the fingers which were not interrupted during the competition process, mentioned in the previous Section. The flow rate intensity of a single channel exhibit fluctuation in time, although the average value remains approximately stable and does not drop to zero. On the other hand, above Λ, in the foam region, the main flowing channels fragment into several smaller ones, thus distributing the flow throughout the surrounding links. In this region, new channels are continuously formed and destroyed due to the continuous foam generation led by fragmentation. It results in fluctuations of the local flow rate which are qualitatively different from the ones in the viscous fingering region. To better investigate these fluctuations in time, we select a single link located in a flowing channel, in the fingering region and in the foam region. We plot $\widetilde{Q}$ as a function

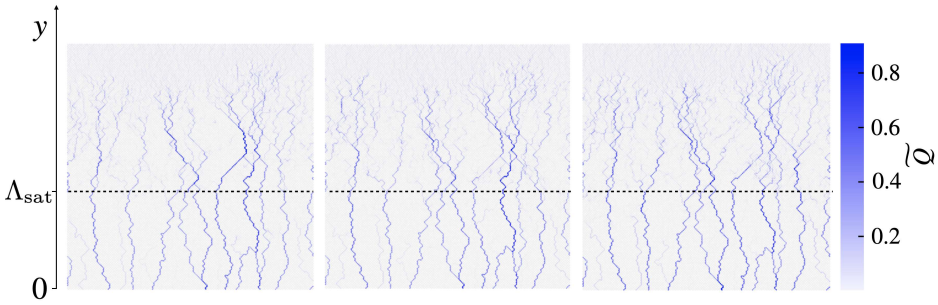

Figure 5.2.9: Color map of the dimensionless local flow rate $\widetilde{Q}$ defined in equation (5.13), at consecutive times from left to right, for a simulation with $\mathrm{Ca}_P = 0.25$, $M = 10^{-2}$, and r_0 uniformly distributed according to Equation (5.2) with $\overline{r_0} = 0.25\,l$ and $a = 0.15\,l$. The horizontal dashed lines represent the position of Λ_{sat} in the pictures, corresponding to $\Lambda_{\mathrm{sat}}/l \simeq 79$.

of the normalized time t/T, where T is the total invasion time. Results are shown in Figure 5.2.10 (upper row) for a link (left) in the viscous finger region, $y < \Lambda_{\mathrm{sat}}$, and a link (right) in the foam region, $y > \Lambda_{\mathrm{sat}}$. We can see that in both cases $\widetilde{Q}(t/T)$ resemble a stochastic process.

To characterize this stochastic process, Figure 5.2.10 (upper row) shows the absolute value of the temporal Fourier transform of the local flow rate, $|\mathscr{F}[\widetilde{Q}](f)|$. We can see that, for the link at in the viscous fingering region (left), the Fourier spectrum decays approximately as the inverse of the frequency, namely $|\mathscr{F}[\widetilde{Q}](f)| \propto f^{-1}$, for $f \lesssim 10^{-1}$. This indicates that $\hat{q}$ behaves like a random walk (Brownian) noise, at least for the lower frequencies. On the other hand, for the link in the foam region (right), the power-law decay occurs approximately as $|\mathscr{F}[\widetilde{Q}](f)| \propto f^{-1/2}$ for $f \lesssim 10^{-1.5}$. An exponent smaller (in modulus) than -1 is typical of anti-correlated signals, and in particular the exponent $-1/2$ is an indicator of pink noise. As a remark, we report that we performed an analysis, not shown here, of both the local flow rate signals using wavelets, and observed results consistent with these obtained by Fourier analysis.

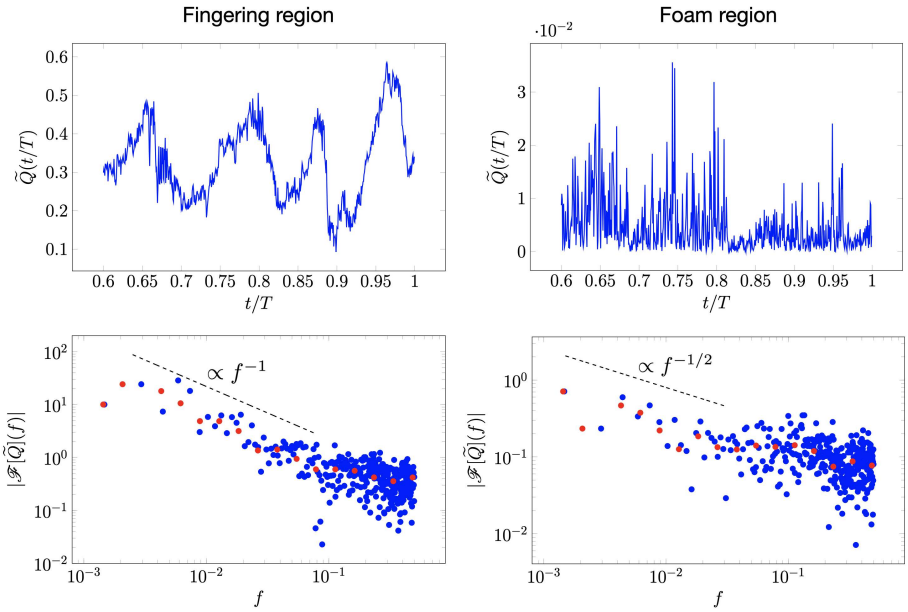

Figure 5.2.10: Upper row: Plots of the dimensionless local flow rate $\widetilde{Q}$ defined in equation (5.13) for a link, belonging to a flowing channel, located at $y/l = 40$ (left plot) and at $y/l = 120$ (right plot), as a function of the normalized time t/T in the interval $0.6 \leq t/T \leq 1$, when foam is already formed. Lower row: Plots of the absolute value of Fourier spectrum $|\mathscr{F}[\widetilde{Q}](f)|$ of the corresponding $\widetilde{Q}(t/T)$ shown above. Blue dots represent the values obtained from FFT. Red dots are obtained averaging these values in 20 equally logarithmic-spaced bins in the interval $[10^{-3}, 1]$. For this simulation, $\mathrm{Ca}_P = 0.125$, $M = 10^{-2}$, and r_0 uniformly distributed according to equation (5.2) with $\overline{r_0} = 0.25\,l$ and $a = 0.15\,l$.

CHAPTER

SIX

CONCLUSIONS

In the present thesis, the description and characterization of both the steady-state non-linear flow and the unsteady-state two-phase flow in porous media was reviewed and explored, adopting a theoretical approach.
Regarding the problem of the two-phase non-Newtonian flow in capillary tubes, an investigation which combines the effects coming from (i) the yield stress nature of one of the two phases and (ii) the capillary forces separating the two fluids, has limited precedents in the existing body of research and, to our knowledge, appears to be novel in the specific framework of the capillary bundle model. In parallel to this, the examination of the flow behavior of a Bingham fluid within a tree-like pore network model seems to have not been explored previously (and in the independent channels configuration as well). During both these investigative projects, expressions for the steady-state average flow rate $\overline{Q}$ as a function of the pressure drop imposed ΔP were proposed, analytically derived when possible, or extracted from numerical simulations. A non-linear behaviour for $\overline{Q}(\Delta P)$ was found when ΔP was higher than, but sufficiently close to, the critical pressure drop $\Delta P_{\min}$, constituting each of these cases a derogation from the linear Darcy law. The non linearity can be in general tracked back to the subsequent opening of new paths (tubes in the capillary bundle, channels in the pore network), as already pointed out in literature. What determines the particular laws found for $\overline{Q(\Delta P)}$ is the way the critical pressures ΔP_c of the single channels above $\Delta P_{\min}$ are distributed. For the two-phase capillary bundle, the specific tube geometry affects the probability distribution of these pressure thresholds, so different tube geometries lead to different laws for $\overline{Q(\Delta P)}$. In particular, a power-law was found in the sinusoidal case, while a non-essential singularity is developed in the case of a triangular tube. For the Bingham flow in a Cayley tree, the exponential growth found for $\overline{Q(\Delta P)}$ can be explained by the fact that the first open channels share low overlap between them, and their number above $\Delta P_{\min}$ is the same as if they would be independent, for which an exponential growth is known to hold true.
In the case of unsteady drainage displacement, a transition from viscous fingering to foam formation, obtained when imposing an overall pressure drop, appears to be never observed before. The characterization of the transition height performed as a function of the pressure-based capillary number Ca_P and the viscosity ratio M allows in principle to control the location of this transition, finding the optimal conditions for reproducing it *in situ*. The formation of a stable front, a significant

increase in the non-wetting saturation, and a decrease of global mobility, the latter observed assessing the overall flow rate, are the main effect observed related to the foam formed from this transition, which might find possible practical applications. Although it is not still clear what leads to the fragmentation of fingers, a connection with the fluctuations in the local flow rate was hypothesized and established. The characterization of the temporal evolution of the local flow rate is seen to be the key for understanding this phenomenon, which might lead to future investigations.
The role of the porous medium heterogeneity in determining the flow characteristics was also questioned in the frame of these projects. Confirming the findings of previous works concerning one dimensional porous media, in the capillary bundle we found a strong dependence of the steady-state flow curves from the different type of disorder, here represented by the different variations of the radius along the tubes. On the other hand, the exponential behaviour found for the average flow rate in a multi-dimensional Cayley tree pore network seems to be independent on the distribution from which the thresholds of the pore tubes are generated, since this affects only the prefactor. However, when dealing with the drainage displacement in two dimensional pore network, it was found that the transition location in the pore medium is affected by the type of distribution chosen for the pore size. Instead, keeping the same kind of PDF and tuning only its width, the position of the transition is observed not to vary. This is in agreement with previous numerical pore network investigations, affirming that the shape of a distribution and its width, taken separately, might control different physical quantities. Hence, even in porous media with dimensionality greater than one, flow properties are not necessarily independent from the disorder chosen.

6.1 Future perspectives

Since we have characterized the steady-state of a two-phase non-Newtonian flow in a one-dimensional porous medium, a natural continuation of this work would consist in extending this description to a porous medium of dimensionality equal to two or greater. In the framework of a dynamic pore network model, the contribution from the different forces into play (viscous, capillary, yield stress) can be assessed to find a characteristic law for the flow rate versus pressure drop in a two- or three-dimensional pore network, also as a function of the fractional flow rate. Since the relations regulating the flow at the pore level are non-linear, efficient methods, already developed for solving systems of non-linear equations, can be applied for solving the flow problem.
The unsteady immiscible displacement and foam formation can be also extended, by supposing that the the wetting or the non-wetting phase present yield stress. With respect to the case that we have analyzed, an additional force contributes in the dynamics. The characterization of the transition will then depend by one more parameter, expressing the ratio between the yield stress force and the other ones.
In all of these studies which involve dynamic pore network model simulations, the algorithms that we already implied for displacing the fluids and distributing them between different pores can still be adopted. Nevertheless, the model can

be improved, for example extending it in three dimensions, or by incorporating other effects that have been previously neglected, like wettability changes given by dynamic contact angles, or the formation of fluid films at the pore walls that might affect the dynamics, especially in drainage scenarios.
As a concluding remark, we remind that the models and numerical simulations presented in this thesis can be verified by the experimental observation. Experiments can be either performed by adopting samples of materials that naturally present a porous structure, or building engineered tools having the same features of a porous medium. While the final goal should be to apply the knowledge to real situations involving real porous material, the latter choice present the advantage of studying general and statistical properties which are not sample-dependent.

APPENDICES

APPENDIX

A

BLOBS OF DIFFERENT SIZES IN SINUSOIDAL TUBES

In this Appendix we generalize the study of the flow in sinusoidal tubes considering N blobs of different lengths. We call Δx_0 the size of the blob positioned at x_b and Δx_i the size of the blob at $x_b + x_i$, and for all i we take $\Delta x_i \ll l$. We also consider a radius variation small enough so that we can take every Δx_i constant. In the limit of small flow rate $q \to 0$, the pressure drop at the edges of the i-th blob is

$$P^+_{x_b+x_i} - P^-_{x_b+x_i+\Delta x_i} = \Delta x_i \left(\frac{q(x_b)}{C_0 r_0^{4+\frac{1}{n}}} \right)^{\frac{n}{n+1}} + P_{\tau,i} \left(1 + af\left(\frac{x_b + x_i}{r_0} \right) \right). \quad \text{(A.1)}$$

where $P_{\tau,i} = 2\tau_c \Delta x_i / r_0$. To this, one must add the capillary pressure drop $aP_\gamma \Delta x_i f'((x_b + x_i)/r_0)$. Summing the contributions of all the N blobs and neglecting the pressure drop induced by the Newtonian fluid, we obtain the following flow rate equation:

$$q(x_b, \{x_i\}; \{\Delta x_i\}) = C_0 r_0^{4+\frac{1}{n}} \left[\frac{\Delta P - \Gamma\left(x_b/r_0; \{x_i/r_0\}, \{\Delta x_i\}\right)}{\sum_{i=0}^{N-1} \Delta x_i} \right]^{\frac{1}{n}+1}, \quad \text{(A.2)}$$

where

$$\begin{aligned} \Gamma\left(\frac{x_b}{r_0}; \left\{ \frac{x_i}{r_0} \right\}, \{\Delta x_i\} \right) &= \sum_{i=0}^{N-1} P_{\tau,i} + \\ &+ a\left(\frac{2\tau}{r_0} G\left(\frac{x_b}{r_0}; \left\{ \frac{x_i}{r_0} \right\}, \{\Delta x_i\} \right) + \frac{P_\gamma}{r_0} G'\left(\frac{x_b}{r_0}; \left\{ \frac{x_i}{r_0} \right\}, \{\Delta x_i\} \right) \right) \end{aligned} \quad \text{(A.3)}$$

and the function

$$G\left(\frac{x_b}{r_0}; \left\{ \frac{x_i}{r_0} \right\}, \{\Delta x_i\} \right) = \Delta x_0 \, f\left(\frac{x_b}{r_0} \right) + \sum_{i=1}^{N-1} \Delta x_i \, f\left(\frac{x_b + x_i}{r_0} \right). \quad \text{(A.4)}$$

We now focus on the case of a tube presenting the sinusoidal modulation given by eq. (3.38). Defining $\theta_b = 2\pi x_b / l$ and $\theta_i = 2\pi x_i / l$, equation (A.4) can be written as a single sine function

$$G(x_b/r_0; \{x_i/r_0\}, \{\Delta x_i\}) = \sqrt{N} A \sin(\theta_0 + \phi) \quad \text{(A.5)}$$

with the amplitude

$$A = \frac{1}{\sqrt{N}} \sqrt{\left(\Delta x_0 + \sum_{i=1}^{N-1} \Delta x_i \cos\theta_i \right)^2 + \left(\sum_{i=1}^{N-1} \Delta x_i \sin\theta_i \right)^2}$$

and the phase shift $\phi = \arcsin\left(A^{-1} \sum_{i=1}^{N-1} \Delta x_i \sin\theta_i \right)$.
Similarly, we obtain $G'(x_b; \{x_i\}, \{\Delta x_i\}) = -\sqrt{N} A (2\pi/l) \sin(\theta_b + \phi)$. So $\Gamma(\theta_b; \{\theta_i\}, \{\Delta x_i\})$ can be written as:

$$\Gamma(\theta_b; \{\theta_i\}, \{\Delta x_i\}) = \sum_{i=0}^{N-1} P_{\tau,i} + \sqrt{N} A\, P'_t \cos(\theta_b + \phi + \varphi), \tag{A.6}$$

where $P'_t = a\sqrt{(2\tau_c/r_0)^2 + (2\pi P_\gamma / l)^2}$ and $\varphi = -\arccos\left(2\tau_c/(r_0 P'_t)\right)$. The maximum of eq. (A.6) gives the pressure threshold

$$\Delta P_c = \sum_{i=0}^{N-1} P_{\tau,i} + \sqrt{N} A\, P'_t. \tag{A.7}$$

We now suppose that every blob size is distributed uniformly between two extreme values Δx_m and Δx_M, with $\Delta x_\mathrm{m} < \Delta x_\mathrm{M} \ll l$. Then, for N sufficiently large, $\sum_{i=0}^{N-1} P_{\tau,i} = N \langle P_{\tau_c} \rangle$ with $\langle P_{\tau_c} \rangle = \tau_c \left(\Delta x_\mathrm{M} + \Delta x_\mathrm{m} \right) / r_0$. Moreover we assume the angular position θ_i to be distributed uniformly in the interval $[0, 2\pi]$. It follows that the probability distribution $\Pi(A)$, in the domain $[0, +\infty[$, has the following expression:

$$\Pi(A) = \frac{2A}{\Delta^2}\, e^{-\frac{A^2}{\Delta^2}}; \tag{A.8}$$

here we define $\Delta^2 = (\Delta x_\mathrm{M}^2 + \Delta x_\mathrm{m}^2 + \Delta x_\mathrm{m} \Delta x_\mathrm{M})/3$. In particular, $\Pi(A)$ vanishes linearly as $A \to 0$. To prove (A.8), we calculate the probability distribution of the variable $B = NA^2$

$$\begin{aligned} g(B) = {} & \frac{1}{(2\pi)^{N-1}} \frac{1}{(\Delta x_\mathrm{M} - \Delta x_\mathrm{m})^N} \int_0^{2\pi} d\theta_1 \ldots \int_0^{2\pi} d\theta_{N-1} \\ & \times \int_{\Delta x_\mathrm{m}}^{\Delta x_\mathrm{M}} d\Delta x_0 \cdots \int_{\Delta x_\mathrm{m}}^{\Delta x_\mathrm{M}} d\Delta x_{N-1}\, \delta\left(B - NA^2\right). \end{aligned} \tag{A.9}$$

The Laplace transform of eq. (3.58) is

$$\begin{aligned} \widetilde{g}(s) = {} & \frac{1}{(2\pi)^{N-1}} \frac{1}{(\Delta x_\mathrm{M} - \Delta x_\mathrm{m})^N} \int_0^{2\pi} d\theta_1 \ldots \int_0^{2\pi} d\theta_{N-1} \\ & \times \int_{\Delta x_\mathrm{m}}^{\Delta x_\mathrm{M}} d\Delta x_0 \cdots \int_{\Delta x_\mathrm{m}}^{\Delta x_\mathrm{M}} d\Delta x_{N-1} e^{-s\left(\left(\Delta x_0 + \sum_i \Delta x_i \cos\theta_i \right)^2 + \left(\sum_i \Delta x_i \sin\theta_i \right)^2 \right)}. \end{aligned} \tag{A.10}$$

We now define the statistical variables $m_x = \sum_{i=1}^{N-1} \Delta x_i \cos\theta_i$ and $m_y = \sum_{i=1}^{N-1} \Delta x_i \sin\theta_i$. The mean and variance of both $\Delta x_i \cos\theta_i$ and $\Delta x_i \sin\theta_i$ in the interval $[0, 2\pi] \times [\Delta x_\mathrm{m}, \Delta x_\mathrm{M}]$ are respectively 0 and $\Delta^2/2$. m_x and m_y are statistical independent

since their covariance is zero. When $N-1 \simeq N$ is sufficiently large, the distribution of both m_x and m_y is Gaussian with mean zero and variance $N\Delta^2/2$. Eq. (A.10) becomes:

$$\begin{aligned}\widetilde{g}(s) &= \int_{-\infty}^{+\infty} dm_x \frac{e^{-\frac{m_x^2}{N\Delta^2}}}{\sqrt{\pi N\Delta^2}} \int_{-\infty}^{+\infty} dm_y \frac{e^{-\frac{3m_y^2}{N\Delta^2}}}{\sqrt{\pi N\Delta^2}} \int_{\Delta x_{\mathrm{m}}}^{\Delta x_{\mathrm{M}}} d\Delta x_0 \, \frac{e^{-s\left((\Delta x_0+m_x)^2+m_y^2\right)}}{\Delta x_{\mathrm{M}} - \Delta x_{\mathrm{m}}} \\ &= \frac{1}{(1+N\Delta^2 s)} \int_{\Delta x_{\mathrm{M}}}^{\Delta x_{\mathrm{M}}} d\Delta_0 \, \frac{e^{-\Delta x_0^2\left(s-\frac{s^2}{\frac{1}{N\Delta^2}+s}\right)}}{\Delta x_{\mathrm{M}} - \Delta x_{\mathrm{m}}} \xrightarrow{N\gg 1} \frac{1}{1+N\Delta^2 s}\end{aligned} \tag{A.11}$$

The Laplace inversion gives $g(B) = \exp(-B/(Ns))/(Ns)$, from which eq. (A.12) follows. From $\Pi(A)$ we get the distribution of ΔP_c in the interval $[N\langle P_{\tau_c}\rangle, +\infty]$:

$$\pi(\Delta P_c) = \frac{6(\Delta P_c - N\langle P_{\tau_c}\rangle)}{N\Delta^2 P'_\gamma} \, e^{-\frac{3\left(\Delta P_c - N\langle P_{\tau_c}\rangle\right)^2}{N\Delta^2 P'^2_\gamma}}. \tag{A.12}$$

APPENDIX

B

INSIGHT ON SOME DISORDERED MODELS

This Appendix provide some basic knowledge on the models of disordered systems implied in the work of Chapter 4, including results useful for solving the flow problems addressed in that Chapter. In Section B.1 the Random Energy Model is treated, while in Section B.2 the problem of the directed polymer on a Cayley tree is illustrated, including its connection with the discrete KPP equation.

B.1 Random Energy Model

The Random Energy Model (REM) [114] is a model for a disordered system, consisting in a collection of N energy levels E_α, where the label $\alpha = 1, \dots, N$. We assume that N scales with the power of an integer number, namely $N = K^t$ with $K > 1$. Each energy is an independent random variable distributed according to a Gaussian probability distribution with average $t\overline{E}$ and standard deviation $\sqrt{t}\sigma$, with $\overline{E} \in \mathbb{R}$ and $\sigma \in \mathbb{R}^+$:

$$\Pi_t(E) = \frac{e^{-\frac{(E-t\overline{E})}{t\sigma^2}}}{\sqrt{2\pi t}\sigma} \tag{B.1}$$

In this Section we show how to derive the number of energy levels over the minimum energy $E_{\min} = \min_\alpha E_\alpha$ in the limit $N \to \infty$ (equivalent to $t \to \infty$).
First, we calculate the cumulative distribution for $E_{\min}$, corresponding to the probability that $E_{\min}$ is bigger than a certain energy E. This can be written as $F_t(E^N$, where $F_t(E)$ is the cumulative of the Gaussian distribution (B.1) related to a single energy level:

$$F_t(E) = \int_E^{+\infty} dE'\, \Pi_t(E') = \frac{1}{2}\,\mathrm{Erfc}\left(\frac{E-t\overline{E}}{\sqrt{2t}\sigma}\right) \overset{E\to-\infty}{\sim} 1 + \frac{\sqrt{t}\sigma e^{-\frac{(E-t\overline{E})^2}{2\sigma^2 t}}}{\sqrt{2\pi}(E-t\overline{E})}. \tag{B.2}$$

In the last passage (B.2) we consider the limit $E \to -\infty$ since for large N we expect the minimum to follow the same limit. We now set the variable shift $E = a_N + b_N u$, where a_N and b_N are scaling factors that can be derived for large

N [115], and at leading order are equal to

$$a_N \approx t\bar{\tau} - \sigma\sqrt{t}\left[\sqrt{2\ln N} - \frac{\ln(2\sqrt{\pi \ln N})}{\sqrt{2\ln N}}\right] + \dots$$
$$b_N \approx \frac{\sigma\sqrt{t}}{\sqrt{2\ln N}} + \dots$$

Applying the scaling $N = K^t$, the cumulative distribution for the minimal energy writes

$$\begin{aligned}
&\lim_{N\to+\infty} F_t(a_N + b_N u)^N = \\
&= \lim_{t\to+\infty} F_t\left(\underbrace{t(\overline{E} - \sigma\sqrt{2\log K}) + \frac{\sigma\log(2\sqrt{\pi t\log K})}{\sqrt{2\log K}}}_{E_0} + \frac{\sigma u}{\sqrt{2\log K}}\right)^N \qquad \text{(B.3)}\\
&= e^{-e^u},
\end{aligned}$$

which corresponds to the cumulative of the Gumbel distribution function. The minimal energy $E_{\min}$ can be then written as the sum of a deterministic part, highlighted as E_0 in (B.3), and a fluctuating part distributed according to a Gumbel distribution.

We now consider a given realization of the REM. We define the number of energy levels above the minimum, including the minimum itself, up to a quantity $x > 0$ as

$$n^{\mathrm{REM}}(x) = \#(E_\alpha : E_{\min} \le E_\alpha < E_{\min} + x) = \sum_{\alpha=1}^{N} \vartheta(E_{\min} + x - E_\alpha), \qquad \text{(B.4)}$$

where $\vartheta(x)$ is the Heaviside theta function. The probability for $n^{\mathrm{REM}}(x)$ to be exactly equal to $M+1$ can be calculated as

$$\mathrm{Prob}(n^{\mathrm{REM}}(x) = M{+}1) = N\binom{N-1}{M}\int dE\ \rho_t(E)[F_t(E){-}F_t(E{+}x)]^M F_t(E{+}x)^{N-M-1}; \qquad \text{(B.5)}$$

The average of $n^{\mathrm{REM}}(x)$ is then the sum of all possible values $0 \le M \le N-1$ weighted by the respective probabilities:

$$\begin{aligned}
\overline{n^{\mathrm{REM}}(x)} &= \sum_M (M+1)\,\mathrm{Prob}(d(x) = M+1)\\
&= 1 + N(N-1)\int dE\ \rho_t(E)[F_t(E) - F_t(E+x)]F_t(E)^{N-2}. \qquad \text{(B.6)}
\end{aligned}$$

Making the substitution as in Eq. (B.3), in the limit $N = K^t \to \infty$ we obtain

$$n_\infty^{\mathrm{REM}}(x) = \lim_{t\to\infty} \overline{n^{\mathrm{REM}}(x)} = 1 + \int du\ e^{2u-e^u}(e^{\beta_c x} - 1) = e^{\beta_c x} \qquad \text{(B.7)}$$

where $\beta_c = \sqrt{2\log K}/\sigma$. The derivative of (B.7) is the average over many realizations of the disorder of the density of energy levels in the limit of high number of tubes. The latter will be helpful in another problem, the calculation of the flow rate of a Bingham fluid in a series of independent channels, as illustrated in the next Section.

B.2 Directed polymer on a Cayley tree

A Cayley tree network consist in a hierarchical lattice, which starts from an origin node and develop attaching, to every node at a certain level, K other nodes in the following level. For a tree of t levels, there will be in total K^t directed paths, all starting from the origin and each one ending in a different leaf. We will refer to this directed paths as *directed polymers*. Here we will deal with the case $K = 2$. We suppose that every link connecting two nodes i and j present an energy value ϵ_{ij} which is thrown from a certain distribution $\Pi(\epsilon)$. We define E_α the energy of a directed polymer α as the sum of the energies of the links along α:

$$E_\alpha = \sum_{(ij)\in\alpha} \epsilon_{ij} \tag{B.8}$$

It is useful to label the directed paths α by ordering the energies as $E_0 < E_1 < E_2 < \dots$. We call *ground state* the directed polymer with the lowest energy $E_0 = \min_\alpha E_\alpha$, while we refer to the directed polymers with higher energies as *excited states*.
We now define the overlap $\hat{q}_{\alpha\alpha'}$, between two directed polymers α and α', as the number of common links between α and α'. We note that, in the Cayley tree geometry, when two directed polymers split, they will never join again, so the overlap occurs in the first $\hat{q}_{\alpha\alpha'}$ levels. It has been proven that the directed polymers on Cayley tree display one step replica symmetry breaking (1-RSB) [102]. This means that in the limit $t \to \infty$, the overlap among any two low-energy directed polymers is either very small, namely $\hat{q}_{\alpha\alpha'} \sim O(1)$, or very large, namely $\hat{q}_{\alpha\alpha'} \sim t$ [116] (finite t corrections are also known [117, 118]).

We are now interested in calculating the number of energy levels with energy smaller than $E_0 + x$, with $x > 0$, namely

$$n_t^{\text{full}}(x) = \#(E_\alpha : E_0 \le E_\alpha < E_0 + x) = \sum_{\alpha=1}^{N} \vartheta(E_0 + x - E_\alpha). \tag{B.9}$$

It has been proven [119] that the average of (B.9) over different realizations of the disorder can be written as $\overline{n_t^{\text{full}}(x)} = \int dx'\, r_t(x'; x)$, where the function $r_t(x'; x)$ satisfies the following recursive equation:

$$r_{t+1}(x'; x) = 2 \int d\epsilon\, \Pi(\epsilon) \Omega_t(x' - \epsilon) r_t(x' - \epsilon; x), \tag{B.10}$$

$$\Omega_{t+1}(x) = \int d\epsilon\, \Pi(\epsilon) \Omega_t(x - \epsilon)^2, \tag{B.11}$$

with the initial conditions $r_1(x'; x) = \Pi(x + x')$ and $\Omega_1(x) = \int_x^\infty d\epsilon\, \Pi(\epsilon)$. A derivation for Equation (B.10) is given in Subsection B.2.2. The function $\Omega_t(x)$ is the probability that the ground state energy of the directed polymer on a Cayley tree of t levels is larger than x, namely

$$\Omega_t(x) = \overline{\prod_\alpha \vartheta(E_\alpha - x)} = \overline{\vartheta(E_0 - x)}\,, \tag{B.12}$$

so $1-\Omega_t(x)$ is the cumulative distribution of the minimum energy of a directed polymer of t levels. Equation (B.11) is the discrete Kolmogorov-Petrovsky-Piskuno (KPP) equation, which corresponds to growing a $t+1$-level tree starting from two t-level trees [102]. Insight on the KPP equation are provided in Subsection B.2.1.

In the limit $t \to \infty$ a closed-form expression for $\overline{n_\infty^{\text{full}}(x)}$ is not known [120], however a numerical integration of (B.10) and (B.11) shows that the following asymptotic holds [119]:

$$\overline{n_\infty^{\text{full}}(x)} \overset{x\gg 1}{=} Axe^{\beta_c x} \tag{B.13}$$

with $\beta_c = \sqrt{2\log 2}/\sigma$ and A a non-universal constant of order 1.

B.2.1 Discrete KPP equation

Consider a function of the energies E_α with a multiplicative form

$$G_t(x) = \overline{\prod_\alpha g(x-E_\alpha)} \tag{B.14}$$

for some $g(x)$. $G_{t+1}(x)$ and $G_t(x)$ can be related by the following discrete KPP recursive equation:

$$G_{t+1}(x) = \int d\epsilon\, \Pi(\epsilon) G_t^2(x-\epsilon) \tag{B.15}$$

where $\Pi(\epsilon)$ is the PDF of a single link energy and the initial conditions reads $G_{t=0}(x) = g(x)$. The discrete KPP equation (B.15) allows for travelling wave solutions of the form

$$G_t(x) = w(x+ct) \qquad \text{when } t\to\infty \tag{B.16}$$

where c is the velocity of the traveling wave. When the initial conditions $G_0(x) = g(x)$ satisfy $\lim_{x\to\infty} g(x) = 0$ and $\lim_{x\to-\infty} g(x) = 1$, c is positive and the front moves backward (when the limits are reversed c is negative and the front propagates in the forward direction). The form of the front $w(x)$ satisfies the following fixed point equation:

$$w(x+c) = \int d\epsilon\, \Pi(\epsilon) w^2(x-\epsilon) \tag{B.17}$$

We consider initial conditions of the form $g(x) \overset{x\to-\infty}{=} 1-e^{\beta x}$. By substituting this form into Equation (B.17) and expanding at first order in $e^{\beta x}$ one obtains an equation for c as a function of β:

$$c(\beta) = \frac{1}{\beta}\log\left(2\int d\epsilon\, \Pi(\epsilon) e^{-\beta\epsilon}\right) \tag{B.18}$$

The velocity presents a minimum at $\beta = \beta_c$. It was proven [121, 122, 103] that the increasing branch of $c(\beta)$ is unstable and that for $\beta > \beta_c$ both the velocity and the front shape freeze, namely $c(\beta > \beta_c) = c(\beta_c)$ and the front shape takes the form $w_{\min}(x)$ satisfying the fixed point equation:

$$w_{\min}(x + c(\beta_c)) = \int d\epsilon\, \Pi(\epsilon) w_{\min}^2(x-\epsilon) \tag{B.19}$$

This equation corresponds to Equation (4.28) of the main text. Indeed, for $g(x) = \vartheta(-x)$, which corresponds to $\beta \to \infty$, we have $\Omega_t(x)$ as expressed in Eq. (B.12). So $w_{\min}(x)$ corresponds to the probability that the minimal energy of a tree with $t \to \infty$ is larger than x.

B.2.2 Average number of energy levels above the minimum

We report here a derivation for $\overline{n_t^{\text{full}}(x)}$, expressed as $\overline{n_t^{\text{full}}(x)} = \int dx'\, r_t(x';x)$ with $r_t(x';x)$ given by Equation (B.10). By definition

$$n_t^{\text{full}}(x) = \overline{\sum_\alpha \vartheta(x + E_0 - E_\alpha)} = \overline{n_t(E_0 + x)} \tag{B.20}$$

where $n_t(x) = \sum_\alpha \theta(x - E_\alpha)$ We now introduce the generating function of $n_t^{\text{full}}(x)$ with $|\lambda| < 1$:

$$\chi_t(x;\lambda) = \overline{\lambda^{n_t^{\text{full}}(x)}} \tag{B.21}$$

This function satisfies the following identity:

$$\chi_t(x;\lambda) = \int dx'\, \overline{\lambda^{n_t(x'+x)}\delta(x' - E_0)} = 1 + \partial_x \int dx'\, \overline{\lambda^{n_t(x'+x)}\vartheta(E_0 - x')} \tag{B.22}$$

To prove the validity of (B.22) we used $(\partial_x \lambda^n)\vartheta = (\partial_{x'}\lambda^n)\vartheta = \partial_{x'}(\lambda^n\vartheta) - \lambda^n(\partial_{x'}\vartheta)$. The integrand of Equation (B.22) satisfies a discrete KPP equation (B.15) since it can be recast into a multiplicative form:

$$\lambda^{n_t(x'+x)}\vartheta(E_0 - x') = \prod_\alpha \lambda^{\vartheta(x'+x-E_\alpha)}\vartheta(E_\alpha - x') \tag{B.23}$$

In this case, the initial condition reads $g(x';x,\lambda) = \lambda^{\vartheta(x'+x)}\vartheta(-x')$. The average number of energy levels above the minimum can be written as:

$$\overline{n_t^{\text{full}}(x)} = \partial_\lambda \chi_t(x;\lambda)|_{\lambda=1} \tag{B.24}$$

We thus expand for $\lambda = 1 - \epsilon$

$$\overline{\lambda^{n_t(x'+x)}\vartheta(E_0 - x')} = \Omega_t(x') - \varepsilon R_t(x';x) + O(\epsilon^2) \tag{B.25}$$

The function $\Omega_t(x)$ is defined in (B.12). This expansion leads to:

$$\overline{n_t^{\text{full}}(x)} = \int dx'\, \partial_z R_t(x';x) = \int dx'\, r_t(x';x) \tag{B.26}$$

where we set $r_t(x';x) = \partial_x R_t(x';x)$. Now, by plugging the expansion (B.25) in (B.15) and taking the first order in ε, we obtain a linear equation for $R_t(x';x)$

$$R_{t+1}(x';x) = 2\int d\tau\; p(\epsilon)\Omega_t(x'-\epsilon)R_t(x'-\epsilon;x)\;, \quad R_{t=0}(x';x) = \frac{1}{2}\vartheta(x'+x)\vartheta(-x')\;. \tag{B.27}$$

Moreover because of the linearity of (B.27), $r_t(x;z)$ satisfies

$$r_{t+1}(x';x) = 2\int d\epsilon\; \Pi(\epsilon)\Omega_t(x'-\epsilon)r_t(x'-\epsilon;x)\;, \quad r_{t=0}(x';x) = \frac{1}{2}\delta(x'+x) \tag{B.28}$$

whic corresponds to Eq. (B.10).
As reported in the main text, the same equations hold for the determination of $m_{\hat{q}}(x)$. Indeed Equation (B.28) changes as:

$$r_{\hat{q}+1}(x';x) = 2\int dP_\tau\ \Pi(P_\tau) w_{\min}(x'-P_\tau+c(\beta_c)) r_{\hat{q}}(x'-P_\tau;x)\ , \quad r_{\hat{q}=0}(x';x) = -w'_{\min}(x'+x) \tag{B.29}$$

Yielding:

$$m_{\hat{q}}(x) = \int dx'\, r_{\hat{q}}(x';x)\ . \tag{B.30}$$

APPENDIX

C

OPENING OF THE SECOND AND THIRD CHANNEL

In this Appendix we report the derivation of the expression for $\Delta P_c^{(1)}$ used in Section 4.2.1 in the main text and $\Delta P_c^{(2)}$. We also write down the expression of the flow for two channels.

C.1 The two channels problem

For simplicity we will set the pressure at the leaves $P_{\text{out}} = 0$, so $\Delta P = P_{\text{in}}$. The proof works also for finite P_{out} without loss of generalization.

When $\Delta P_c^{(1)} < \Delta P \leq \Delta P_c^{(2)}$, flow occurs along two channels: the one correspond-

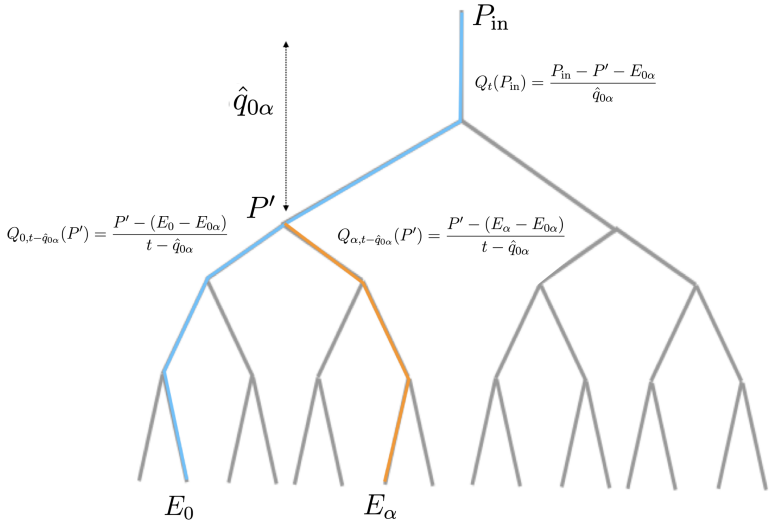

Figure C.1.1: Schematics for the Cayley tree with two open channels.

ing to the ground state, with pressure threshold $\Delta P_c^{(0)}$, and a second channel α with energy E_α (we remind that with 'energy' of a channel we mean the sum of the pressure thresholds along that channel). In Figure C.1.1 we depict them in blue and orange respectively. These two channels have an overlap equal to $\hat{q}_{0\alpha}$; we

denote with $E_{0\alpha}$ the sum of the pressure thresholds along this common portion, and P' the pressure at the bottom of the common part. The total flow rate in the network can be written as the flow rate along the common part:

$$Q_t(P_{\text{in}}) = \frac{P_{\text{in}} - P' - E_{0\alpha}}{\hat{q}_{0\alpha}} \tag{C.1}$$

The pressure P' can be determined using the conservation of the flow:

$$\frac{P_{\text{in}} - P' - E_{0\alpha}}{\hat{q}_{0\alpha}} = Q_{0,t-\hat{q}_{0\alpha}}(P') + Q_{\alpha,t-\hat{q}_{0\alpha}}(P') \tag{C.2}$$

where $Q_{0,t-\hat{q}_{0\alpha}}(P')$ is the flow along the subtree containing the ground state, $Q_{\alpha,t-\hat{q}_{0\alpha}}(P')$ containing the other channel α (see the two branches of Figure C.1.1). Since each of these is a single channel of length $t - \hat{q}_{0\alpha}$, we can use once again the modified Poiseuille equation. One has

$$Q_{0,t-\hat{q}_{0\alpha}}(P') = \frac{P' - (E_0 - E_{0\alpha})}{t - \hat{q}_{0\alpha}}\,, \qquad Q_{\alpha,t-\hat{q}_{0\alpha}}(P') = \frac{P' - (E_\alpha - E_{0\alpha})}{t - \hat{q}_{0\alpha}} \tag{C.3}$$

From equation (C.2) we derive first the expression for $P'(P_{\text{in}})$ and then $Q_t(P_{\text{in}})$:

$$\begin{aligned} P'(P_{\text{in}}) &= \frac{\hat{q}_{0\alpha}(E_0 + E_\alpha) + (t - \hat{q}_{0\alpha})P_{\text{in}}}{t + \hat{q}_{0\alpha}} - E_{0\alpha}\,, \\ Q_t(P_{\text{in}}) &= \frac{2}{t + \hat{q}_{0\alpha}}\left(P_{\text{in}} - \frac{E_0 + E_\alpha}{2}\right). \end{aligned} \tag{C.4}$$

We can now determine the pressure drop ΔP^* such that $Q_t(\Delta P^*)$ as reported in Eq. (C.1) is equal to $(\Delta P^* - \Delta P_c^0)/t$, namely

$$\Delta P^* = \Delta P_c^{(0)} + \frac{t}{t - \hat{q}_{0\alpha}}(E_\alpha - \Delta P_c^{(0)}) \tag{C.5}$$

For pressure $\Delta P \in (\Delta P_c^{(0)}, \Delta P^*)$ we have $(\Delta P^* - \Delta P_c^0)/t > Q_t(\Delta P_c^*)$, this means that the fluid cannot flow in the second channel and the flow rate is given by $Q_{0,t}(P)$. Above ΔP^* the second channel is open and the flow rate is given by $Q_t(\Delta P_c^*)$. The criterion to select the first excited channel that opens above $\Delta P_c^{(0)}$, is that the pressure $\Delta P_c^{(1)}$ is the smallest among all the ΔP^* computed for all possible two-channel geometries. This translates into

$$\Delta P_c^{(1)} = \min_{\Delta P_c^*} \Delta P_c^* = \Delta P_c^{(0)} + \min_{\alpha \neq 0} \frac{t}{t - \hat{q}_{0\alpha}}(E_\alpha - \Delta P_c^{(0)}) \tag{C.6}$$

The channel satisfying the minimum condition is denoted by α_1.

C.2 The three channels problem

There are three possible configurations for the position of the second excited channel with respect to the ground state and the first one. They each lead to a slightly different expression for the pressure $\Delta P_c^{(2)}$, but all simplify to $\Delta P_c^{(2)} = E_{\alpha_2}$ in the limit $t \to \infty$.

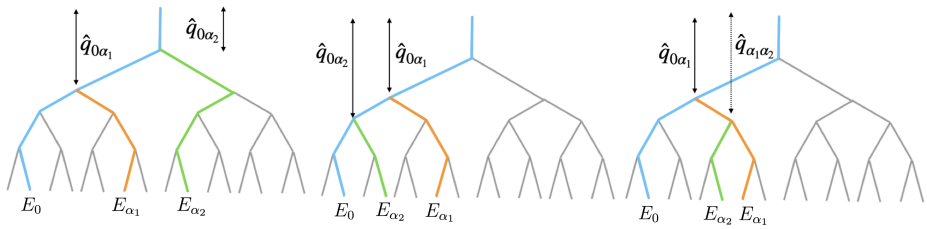

Figure C.2.1: Schematics for the Cayley tree with three open channels in the three possible geometrical arrangements.

The first case is the simplest: the second channel opens with a common overlap $\hat{q}_{0\alpha_2} = \hat{q}_{\alpha_1\alpha_2}$ with the ground state and the first channel. See Figure C.2.1 left. By construction, $\hat{q}_{0\alpha_2} < \hat{q}_{0\alpha_1}$.
The pressure $\Delta P_c^{(2)}$ reads:

$$\Delta P_c^{(2)} = \min_{\alpha_2 \neq \{\alpha_1, 0\}} \left[E_{\alpha_2} - \frac{\hat{q}_{0\alpha_2}}{t + \hat{q}_{0\alpha_1} - 2\hat{q}_{0\alpha_2}} (E_{\alpha_1} + E_0 - 2E_{\alpha_2}) \right] \tag{C.7}$$

In the limit $t \to \infty$, we saw that $\hat{q}_{0\alpha_1} = O(1)$; from this and $\hat{q}_{0\alpha_2} < \hat{q}_{0\alpha_1}$, it follows that $\hat{q}_{0\alpha_2} = O(1)$ and $\Delta P_c^{(2)} = E_{\alpha_2}$.

The second case corresponds to the opening of the second excited channel from the ground state with an overlap $\hat{q}_{0\alpha_2} > \hat{q}_{\alpha_1\alpha_2} = \hat{q}_{0\alpha_1}$. See figure C.2.1 middle. The pressure $\Delta P_c^{(2)}$ reads:

$$\Delta P_c^{(2)} = \Delta P_c^{(0)} - \frac{\hat{q}_{0\alpha_1}}{t - \hat{q}_{0\alpha_1}} (E_{\alpha_1} - \Delta P_c^{(0)}) + \min_{\alpha_2 \neq \{\alpha_1, 0\}} \frac{t + \hat{q}_{0\alpha_1}}{t - \hat{q}_{0\alpha_2}} (E_{\alpha_2} - \Delta P_c^{(0)}) \tag{C.8}$$

When $t \to \infty$, the previous argument for the first excited channel sets $\hat{q}_{0\alpha_1}/t \approx 0$. In this limit, the resulting expression for $\Delta P_c^{(2)}$ is:

$$\Delta P_c^{(2)} = \Delta P_c^{(0)} + \min_{\alpha_2 \neq \{\alpha_1, 0\}} \frac{t}{t - \hat{q}_{0\alpha_2}} (E_{\alpha_2} - \Delta P_c^{(0)}) \qquad \text{when } t \to \infty \tag{C.9}$$

This expression is identical to Equation (C.6) with the substitution $\alpha \to \alpha_2$, and applying the same arguments of the first channel we arrive at setting $\hat{q}_{0\alpha_2}/t \approx 0$, leading $\Delta P_c^{(2)} = E_{\alpha_2}$.

The last case is the mirror of the previous one, with the second channels that opens from the first one with overlap $\hat{q}_{\alpha_1\alpha_2} > \hat{q}_{0\alpha_1} = \hat{q}_{0\alpha_2}$. See figure C.2.1 right. The pressure $\Delta P_c^{(2)}$ reads:

$$\Delta P_c^{(2)} = \Delta P_c^{(0)} + \frac{t}{t - \hat{q}_{0\alpha_1}} (E_{\alpha_1} - \Delta P_c^{(0)}) + \min_{\alpha_2 \neq \{\alpha_1, 0\}} \frac{t + \hat{q}_{0\alpha_1}}{t - \hat{q}_{\alpha_1\alpha_2}} (E_{\alpha_2} - E_{\alpha_1}) \tag{C.10}$$

When $t \to \infty$, the previous argument for the first excited channel sets $\hat{q}_{0\alpha_1}/t \approx 0$. In this limit, the resulting expression for $\Delta P_c^{(2)}$ is:

$$\Delta P_c^{(2)} = E_1 + \min_{\alpha_2 \neq \{\alpha_1, 0\}} \frac{t}{t - \hat{q}_{\alpha_1\alpha_2}} (E_{\alpha_2} - E_{\alpha_1}) \qquad \text{when } t \to \infty \tag{C.11}$$

This expression is again similar to Equation (C.6) and applying the same arguments of the first channel we arrive at setting $\hat{q}_{\alpha_1\alpha_2}/t \approx 0$, leading $\Delta P_c^{(2)} = E_{\alpha_2}$.

APPENDIX

D

DEPENDENCE OF THE INVASION PATTERN FROM THE GLOBAL PARAMETERS

For all the simulations discussed in Chapter 5, we assumed that the viscosity ratio $M = \mu_N/\mu_W$ and the capillary number $\mathrm{Ca}_P = (\Delta P/N_x)/(2\gamma/\overline{r_0})$ fully characterize the displacement patterns. In this Appendix, we want to verify this assumption, showing that different simulations prepared setting the same values for M and Ca_P will return the same pattern. For each of the invasion patterns shown in Figure D.0.1, different values for both the surface tension γ and the global pressure drop ΔP were chosen, but such that Ca_P is the same. The patterns are very similar to each other, varying only by small details at the scale of few pores. In particular, the foam originates and propagates from the same transition height Λ. Analogously, Figure D.0.2 show three different patterns for which both the average radius $\overline{r_0}$ and $\Delta P/N_x$ are varied. Also in this case, identical values of Ca_P leads to similar patterns. An analogue test for the viscosity ratio M was done. In Figure D.0.3 it is shown that a different choice for the wetting and non-wetting viscosities, μ_w and μ_n, will not modify the macroscopic output, as long as their ratio is kept equal.
We also investigate the dependence of the invasion pattern from the width of the radii distribution. For different simulations, we generate the tubes radii from the same uniform distribution shown in the main text, that we report here

$$\Pi(r_0) = \begin{cases} 1/a & \text{if } r_0 \in [\overline{r_0} - a/2, \overline{r_0} + a/2] \\ 0 & \text{otherwise} \end{cases}, \tag{D.1}$$

having the same $\overline{r_0}$ but different width a. The outputs are presented in Figure D.0.4, where we observe Λ to remain the same, while the number of finger and the compactness of the foam seem both to decrease as a rises. A further analysis might characterize and quantify this relationship.
Finally, to look at the influence of the network size, in Figure D.0.5 we show some patterns obtained varying only the number of tubes per side, $N_x = N_y \equiv N$ in a square network. We observe the finger-foam transition to occur at approximately the same distance Λ from the inlet, so the foam just propagates for longer distances when N is bigger.
Note that the unit of measure of the physical quantities, not reported here, can be chosen arbitrarily, as long as the choice remain consistent with the fact that the global parameters introduced must be dimensionless.

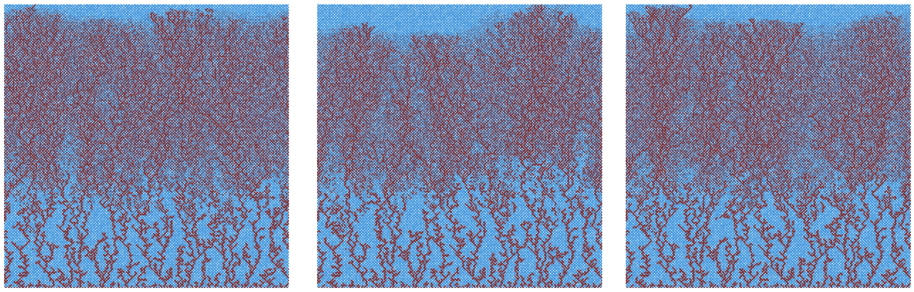

Figure D.0.1: Snapshots of the invasion pattern at breakthrough setting different combinations of the surface tension γ and the global pressure drop ΔP but keeping $\mathrm{Ca}_P = 0.25$ For these simulations we set $N_x = N_y = 200$, $M = 10^{-2}$ and r_0 uniformly distributed according to eq. (D.1) with $\overline{r_0} = 0.25l$ and $a = 0.15l$.

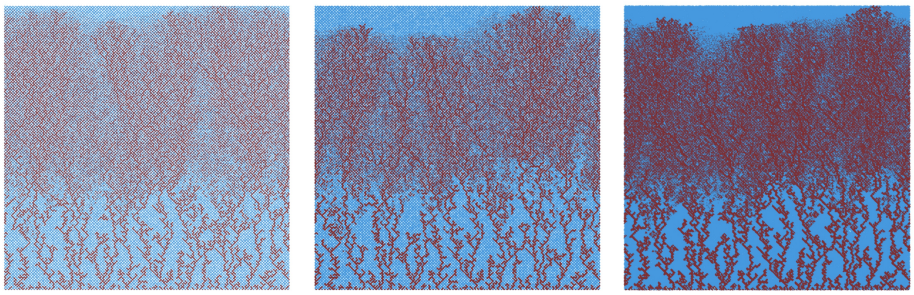

Figure D.0.2: Snapshots of the invasion pattern at breakthrough setting different combinations of the average radius $\overline{r_0}$ and the global pressure drop ΔP but keeping $\mathrm{Ca}_P = 0.25$. For these simulations we set $N_x = N_y = 200$, $M = 10^{-2}$ and r_0 uniformly distributed according to eq. (D.1) with $a = 0.15l$.

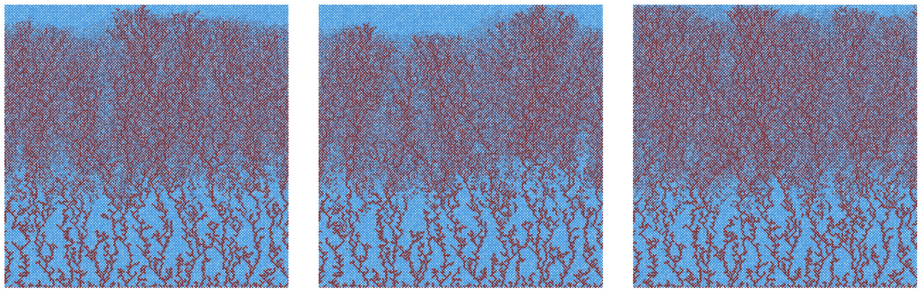

Figure D.0.3: Snapshots of the invasion pattern at breakthrough setting different combinations of the viscosities μ_n and μ_w but keeping $M = 10^{-2}$. For these simulations we set $N_x = N_y = 200$, $\mathrm{Ca}_P = 0.25$ and r_0 uniformly distributed according to eq. (D.1) with $\overline{r_0} = 0.25l$ and $a = 0.15l$.

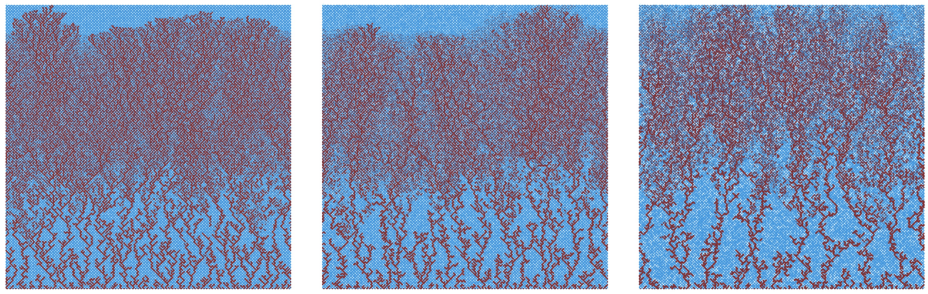

Figure D.0.4: Snapshots of the invasion pattern at breakthrough with r_0 uniformly distributed according to eq. (D.1) with $\overline{r_0} = 0.25\,l$ and different values for a. For these simulations we set $N_x = N_y = 200$, $\mathrm{Ca}_P = 0.25$ and $M = 10^{-2}$.

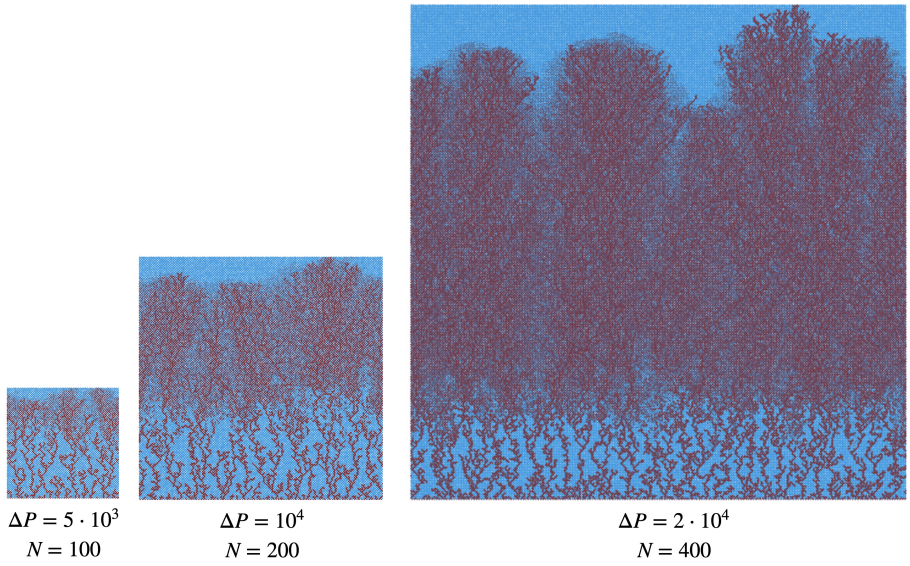

Figure D.0.5: Snapshots of the invasion pattern at breakthrough setting different system lengths $N = N_x = N_y$. For these simulations we set $\mathrm{Ca}_P = 0.25$, $M = 10^{-2}$, and r_0 uniformly distributed according to eq. (D.1) with $\overline{r_0} = 0.25l$ and $a = 0.15l$.).

REFERENCES

[1] Our World in Data. *Primary energy consumption by source, World, 2022*. 2022. URL: https://ourworldindata.org/sources-global-energy (visited on 05/09/2023).

[2] A. Kopp, H. Class, and R. Helmig. "Investigations on CO2 storage capacity in saline aquifers: Part 1. Dimensional analysis of flow processes and reservoir characteristics". In: *International Journal of Greenhouse Gas Control* 3.3 (2009), pp. 263–276. ISSN: 1750-5836. DOI: https://doi.org/10.1016/j.ijggc.2008.10.002. URL: https://www.sciencedirect.com/science/article/pii/S1750583608000972.

[3] J. Feder, E. G. Flekkøy, and A. Hansen. *Physics of flow in porous media*. Cambridge University Press, 2022.

[4] Henry Darcy. *Les fontaines publiques de la ville de Dijon: exposition et application...* Victor Dalmont, 1856.

[5] P. G. Nutting. "Physical Analysis of Oil Sands". In: *AAPG Bulletin* 14.10 (Oct. 1930), pp. 1337–1349. ISSN: 0149-1423. DOI: 10.1306/3D932938-16B1-11D7-8645000102C1865D. eprint: https://pubs.geoscienceworld.org/aapgbull/article-pdf/14/10/1337/4351370/aapg_1930_0014_0010_1337.pdf. URL: https://doi.org/10.1306/3D932938-16B1-11D7-8645000102C1865D.

[6] L. J. Klinkenberg. "The Permeability Of Porous Media To Liquids And Gases". In: *Drilling and Production Practice* (1941), pp. 200–213.

[7] P. Forchheimer. "Wasserbewegung durch Boden". In: *Zeitschrift des vereins Deutscher Ingenieure* 42 (1901), pp. 1782–1788.

[8] C. C. Mei and J.-L. Auriault. "The effect of weak inertia on flow through a porous medium". In: *Journal of Fluid Mechanics* 222 (1991), pp. 647–663. DOI: 10.1017/S0022112091001258.

[9] C. C. Mei and J.-L. Auriault. "A calculation of the viscous force exerted by a flowing fluid on a dense swarm of particles". In: *Flow, Turbulence and Combustion* 1 (Dec. 1949), pp. 27–34. DOI: 10.1007/BF02120313. URL: https://doi.org/10.1007/BF02120313.

[10] R. Jäger, M. Mendoza, and H. J. Herrmann. "Clogging at pore scale and pressure-induced erosion". In: *Phys. Rev. Fluids* 3 (7 July 2018), p. 074302. DOI: 10.1103/PhysRevFluids.3.074302. URL: https://link.aps.org/doi/10.1103/PhysRevFluids.3.074302.

[11] R. Jäger, M. Mendoza, and H. J. Herrmann. "Mechanism behind Erosive Bursts In Porous Media". In: *Phys. Rev. Lett.* 119 (12 Sept. 2017), p. 124501. DOI: 10.1103/PhysRevLett.119.124501. URL: https://link.aps.org/doi/10.1103/PhysRevLett.119.124501.

[12] Filippo Bianchi et al. "Tomographic Study of Internal Erosion of Particle Flows in Porous Media". In: *Transport in Porous Media* 122 (1 Jan. 2018), pp. 169–184. DOI: 10.1007/s11242-017-0996-8. URL: https://doi.org/10.1007/s11242-017-0996-8.

[13] J.M. Piau. "Carbopol gels: Elastoviscoplastic and slippery glasses made of individual swollen sponges: Meso- and macroscopic properties, constitutive equations and scaling laws". In: *Journal of Non-Newtonian Fluid Mechanics* 144.1 (2007), pp. 1–29. ISSN: 0377-0257. DOI: 10.1016/j.jnnfm.2007.02.011. URL: http://www.sciencedirect.com/science/article/pii/S0377025707000687.

[14] H. Pascal. "Nonsteady flow through porous media in the presence of a threshold gradient". In: *Acta Mechanica* 39.3 (Sept. 1981), pp. 207–224. ISSN: 1619-6937. DOI: 10.1007/BF01170343. URL: https://doi.org/10.1007/BF01170343.

[15] H.A. Barnes, J.F. Hutton, and K. Walters. *An introduction to rheology.* Vol. 3. Elsevier Science Limited, New York, NY, 1989.

[16] P. Coussot. *Rheometry of pastes, suspensions, and granular materials: applications in industry and environment.* John Wiley and Sons, New York, NY, 2005.

[17] A. S. Popel and P. C. Johnson. "Microcirculation and hemorheology". In: *Annual Review of Fluid Mechanics* 37.1 (2005), pp. 43–69. DOI: 10.1146/annurev.fluid.37.042604.133933.

[18] N. Bessonov et al. "Methods of blood flow modelling". In: *Mathematical modelling of natural phenomena* 11.1 (2016), pp. 1–25. DOI: 10.1051/mmnp/201611101.

[19] A. C. Barbati et al. "Complex Fluids and Hydraulic Fracturing". In: *Annual Review of Chemical and Biomolecular Engineering* 7.1 (2016), pp. 415–453. DOI: 10.1146/annurev-chembioeng-080615-033630.

[20] R. P. Widmer Soyka et al. "Numerical description and experimental validation of a rheology model for non-Newtonian fluid flow in cancellous bone". In: *Journal of the Mechanical Behavior of Biomedical Materials* 27 (2013), pp. 43–53. ISSN: 1751-6161. DOI: 10.1016/j.jmbbm.2013.06.007.

[21] Winslow H. Herschel and Ronald Bulkley. "Konsistenzmessungen von Gummi-Benzollösungen". In: *Kolloid-Zeitschrift* 39 (Aug. 1926), pp. 291–300. DOI: 10.1007/BF01432034. URL: https://doi.org/10.1007/BF01432034.

[22] V.M. Entov. "On some two-dimensional problems of the theory of filtration with a limiting gradient." In: *Prikl. Mat. Mekh.* 31 (1967), pp. 820–833. DOI: 10.1016/0021-8928(67)90120-7.

[23] H.C. Park, M.C. Hawley, and R.F. Blanks. "The flow of non-Newtonian solutions through packed beds". In: *SPE* 15.11 (1973), p. 4722. DOI: 10.1002/pen.760151102.

[24] T. Sochi and M.J. Blunt. "Pore-scale network modeling of Ellis and Herschel-Bulkley fluids". In: *J. Pet. Sci. Eng.* 60.2 (2008), pp. 105–124. ISSN: 0920-4105. DOI: 10.1016/j.petrol.2007.05.009.

[25] A. Rodríguez de Castro and G. Radilla. "Non-Darcian flow of shear-thinning fluids through packed beads: Experiments and predictions using Forchheimer's law and Ergun's equation". In: *Advances in Water Resources* 100 (2017), pp. 35–47. ISSN: 0309-1708. DOI: 10.1016/j.advwatres.2016.12.009.

[26] T. Chevalier et al. "Darcy's law for yield stress fluid flowing through a porous medium". In: *J. Non-Newtonian Fluid Mech.* 195.0 (2013), pp. 57–66. ISSN: 0377-0257. DOI: 10.1016/j.jnnfm.2012.12.005.

[27] N. Waisbord et al. "Anomalous percolation flow transition of yield stress fluids in porous media". In: *Phys. Rev. Fluids* 4 (6 June 2019), p. 063303. DOI: 10.1103/PhysRevFluids.4.063303.

[28] S. Roux and H. J. Herrmann. "Disorder-Induced Nonlinear Conductivity". In: *Europhys. Lett.* 4.11 (1987), p. 1227. DOI: 10.1209/0295-5075/4/11/003.

[29] M. Chen, Y.C. Yortsos, and W.R. Rossen. "Insights on foam generation in porous media from pore-network studies". In: *Colloids and Surfaces A: Physicochemical and Engineering Aspects* 256.2 (2005), pp. 181–189. ISSN: 0927-7757. DOI: 10.1016/j.colsurfa.2005.01.020. URL: https://www.sciencedirect.com/science/article/pii/S0927775705000865.

[30] L. Talon and D. Bauer. "On the determination of a generalized Darcy equation for yield-stress fluid in porous media using a Lattice-Boltzmann TRT scheme". In: *Eur. Phys. J. E* 36.12 (2013), p. 139. ISSN: 1292-8941. DOI: 10.1140/epje/i2013-13139-3.

[31] T. Chevalier and L. Talon. "Generalization of Darcy's law for Bingham fluids in porous media: From flow-field statistics to the flow-rate regimes". In: *Phys. Rev. E* 91 (2 Feb. 2015), p. 023011. DOI: 10.1103/PhysRevE.91.023011.

[32] Chen Liu et al. "Darcy's Law for Yield Stress Fluids". In: *Phys. Rev. Lett.* 122 (24 June 2019), p. 245502. DOI: 10.1103/PhysRevLett.122.245502. URL: https://link.aps.org/doi/10.1103/PhysRevLett.122.245502.

[33] S. Nash and D .S. Rees. "The effect of microstructure on models for the flow of a Bingham fluid in porous media". In: *Transp. Porous Media* (2016). DOI: 10.1007/s11242-016-0813-9.

[34] Apiano F. Morais et al. "Non-Newtonian Fluid Flow through Three-Dimensional Disordered Porous Media". In: *Phys. Rev. Lett.* 103 (19 Nov. 2009), p. 194502. DOI: 10.1103/PhysRevLett.103.194502. URL: https://link.aps.org/doi/10.1103/PhysRevLett.103.194502.

[35] Reiner Helmig. *Multiphase flow and transport processes in the subsurface: a contribution to the modeling of hydrosystems.* Springer-Verlag, 1997. URL: https://doi.org/10.1007/s11242-017-0996-8.

[36] S. Sinha and A. Hansen. "Effective rheology of immiscible two-phase flow in porous media". In: *Europhys. Lett.* 99.4 (2012), pp. 44004–. ISSN: 0295-5075. DOI: 10.1209/0295-5075/99/44004.

[37] K. T. Tallakstad et al. "Steady-state, simultaneous two-phase flow in porous media: An experimental study". In: *Phys. Rev. E* 80 (3 Sept. 2009), p. 036308. DOI: 10.1103/PhysRevE.80.036308.

[38] E. M. Rassi, S. L. Codd, and J. D. Seymour. "Nuclear magnetic resonance characterization of the stationary dynamics of partially saturated media during steady-state infiltration flow". In: *New Journal of Physics* 13.1 (2011), pp. 015007–. ISSN: 1367-2630. DOI: 10.1088/1367-2630/13/1/015007.

[39] T. Chevalier et al. "History effects on nonwetting fluid residuals during desaturation flow through disordered porous media". In: *Phys. Rev. E* 91 (4 Apr. 2015), p. 043015. DOI: 10.1103/PhysRevE.91.043015.

[40] Y. Zhang et al. "Quantification of Nonlinear Multiphase Flow in Porous Media". In: *Geophysical Research Letters* 48.5 (2021). DOI: 10.1029/2020GL090477.

[41] A. G. Yiotis, L. Talon, and D. Salin. "Blob population dynamics during immiscible two-phase flows in reconstructed porous media". In: *Phys. Rev. E* 87 (3 Mar. 2013), p. 033001. DOI: 10.1103/PhysRevE.87.033001.

[42] S. Sinha et al. "Effective Rheology of Two-Phase Flow in Three-Dimensional Porous Media: Experiment and Simulation". In: *Transport in Porous Media* 119.1 (Aug. 2017), pp. 77–94. ISSN: 1573-1634. DOI: 10.1007/s11242-017-0874-4.

[43] A. G. Yiotis et al. "Nonlinear Darcy flow dynamics during ganglia stranding and mobilization in heterogeneous porous domains". In: *Phys. Rev. Fluids* 4 (11 Nov. 2019), p. 114302. DOI: 10.1103/PhysRevFluids.4.114302.

[44] O. Aursjø et al. "Film flow dominated simultaneous flow of two viscous incompressible fluids through a porous medium". In: *Front. Physics* 2 (2014), p. 63. DOI: 10.3389/fphy.2014.00063.

[45] S. Roy, A. Hansen, and S. Sinha. "Effective Rheology of Two-Phase Flow in a Capillary Fiber Bundle Model". In: *Frontiers in Physics* 7 (2019), p. 92. ISSN: 2296-424X. DOI: 10.3389/fphy.2019.00092.

[46] A. Birovljev et al. "Gravity invasion percolation in two dimensions: Experiment and simulation". In: *Phys. Rev. Lett.* 67 (5 July 1991), pp. 584–587. DOI: 10.1103/PhysRevLett.67.584. URL: https://link.aps.org/doi/10.1103/PhysRevLett.67.584.

[47] Benzhong Zhao, Christopher W. MacMinn, and Ruben Juanes. "Wettability control on multiphase flow in patterned microfluidics". In: *Proceedings of the National Academy of Sciences* 113.37 (2016), pp. 10251–10256. DOI: 10.1073/pnas.1603387113. eprint: https://www.pnas.org/doi/pdf/10.1073/pnas.1603387113. URL: https://www.pnas.org/doi/abs/10.1073/pnas.1603387113.

[48] Roland Lenormand and Cesar Zarcone. "Invasion Percolation in an Etched Network: Measurement of a Fractal Dimension". In: *Phys. Rev. Lett.* 54 (1985), p. 2226. DOI: 10.1103/PhysRevLett.54.2226.

[49] D Wilkinson and J F Willemsen. "Invasion percolation: a new form of percolation theory". In: *J. Phys. A: Math. Gen.* 16 (1983), p. 3365. DOI: 10.1088/0305-4470/16/14/028.

[50] David Wilkinson. "Percolation effects in immiscible displacement". In: *Phys. Rev. A* 34 (1986), p. 1380. DOI: 10.1103/PhysRevA.34.1380.

[51] Knut Jørgen Måløy, Jens Feder, and Torstein Jøssang. "Viscous Fingering Fractals in Porous Media". In: *Phys. Rev. Lett.* 55 (24 Dec. 1985), pp. 2688–2691. DOI: 10.1103/PhysRevLett.55.2688. URL: https://link.aps.org/doi/10.1103/PhysRevLett.55.2688.

[52] G M Homsy. "Viscous fingering in porous media". In: *Annu. Rev. Fluid Mech.* 19 (1987), p. 271. DOI: 10.1146/annurev.fl.19.010187.001415.

[53] I C Salmo et al. "Immiscible Viscous Fingering: Modelling Unstable Water–Oil Displacement Experiments in Porous Media". In: *Transp. Porous Med.* 145 (2022), p. 291. DOI: 10.1007/s11242-022-01847-8.

[54] T. A. Witten and L. M. Sander. "Diffusion-Limited Aggregation, a Kinetic Critical Phenomenon". In: *Phys. Rev. Lett.* 47 (1981), p. 1400. DOI: 10.1103/PhysRevLett.47.1400.

[55] D. W. van Batenbur et al. "Visualisation of Light Oil Mobilisation in ASP Core Floods Using X-Ray CT Imaging". In: *Soc. Petro. Eng.* SPE-174660-MS (2015). DOI: 10.2118/174660-MS. URL: https://onepetro.org/SPEEORC/proceedings-abstract/15EORC/1-15EORC/D011S001R001/184011.

[56] Lincoln Paterson. "Diffusion-Limited Aggregation and Two-Fluid Displacements in Porous Media". In: *Phys. Rev. Lett.* 52 (18 Apr. 1984), pp. 1621–1624. DOI: 10.1103/PhysRevLett.52.1621. URL: https://link.aps.org/doi/10.1103/PhysRevLett.52.1621.

[57] Paul Meakin and J. M. Deutch. "The formation of surfaces by diffusion limited annihilation". In: *The Journal of Chemical Physics* 85.4 (Aug. 1986), pp. 2320–2325. ISSN: 0021-9606. DOI: 10.1063/1.451129. eprint: https://pubs.aip.org/aip/jcp/article-pdf/85/4/2320/11207514/2320_1_online.pdf. URL: https://doi.org/10.1063/1.451129.

[58] Roland Lenormand, Eric Touboul, and Cesar Zarcone. "Numerical models and experiments on immiscible displacements in porous media". In: *Journal of Fluid Mechanics* 189 (1988), p. 165. DOI: 10.1017/S0022112088000953.

[59] Shuang Cindy Cao et al. "Engineering Behavior and Characteristics of Water-Soluble Polymers: Implication on Soil Remediation and Enhanced Oil Recovery". In: *Sustainability* 8 (2016), p. 205. ISSN: 2071-1050. DOI: 10.3390/su8030205. URL: https://www.mdpi.com/2071-1050/8/3/205.

[60] Anindityo Patmonoaji et al. "Three-dimensional fingering structures in immiscible flow at the crossover from viscous to capillary fingering". In: *International Journal of Multiphase Flow* 122 (2020), p. 103147. ISSN: 0301-9322. DOI: https://doi.org/10.1016/j.ijmultiphaseflow.2019.103147. URL: https://www.sciencedirect.com/science/article/pii/S030193221930343X.

[61] Senyou An et al. “Transition From Viscous Fingering to Capillary Fingering: Application of GPU-Based Fully Implicit Dynamic Pore Network Modeling”. In: *Water Resources Research* 56.12 (2020). e2020WR028149 10.1029/2020WR028149, e2020WR028149. DOI: https://doi.org/10.1029/2020WR028149. eprint: https://agupubs.onlinelibrary.wiley.com/doi/pdf/10.1029/2020WR028149. URL: https://agupubs.onlinelibrary.wiley.com/doi/abs/10.1029/2020WR028149.

[62] J Feder. *Fractals*. Springer New York, NY, 1988. DOI: 10.1007/978-1-4899-2124-6.

[63] Roland Lenormand and Cesar Zarcone. “Capillary fingering: Percolation and fractal dimension”. In: *Transp. Porous Med.* 4 (1989), p. 599. DOI: 10.1007/BF00223630.

[64] Suparna Sinha and Sujata Tarafdar. “Viscous Fingering Patterns and Evolution of Their Fractal Dimension”. In: *Industrial & Engineering Chemistry Research* 48.19 (2009), pp. 8837–8841. DOI: 10.1021/ie801836r. eprint: https://doi.org/10.1021/ie801836r. URL: https://doi.org/10.1021/ie801836r.

[65] M. Chen, W. Rossen, and Y. C. Yortsos. “The flow and displacement in porous media of fluids with yield stress”. In: *Chem. Eng. Sci.* 60.15 (2005), pp. 4183–4202. ISSN: 0009-2509. DOI: 10.1016/j.ces.2005.02.054.

[66] William R Rossen. “Theory of mobilization pressure gradient of flowing foams in porous media: I. Incompressible foam”. In: *Journal of Colloid and Interface Science* 136.1 (1990), pp. 1–16. ISSN: 0021-9797. DOI: https://doi.org/10.1016/0021-9797(90)90074-X. URL: https://www.sciencedirect.com/science/article/pii/002197979090074X.

[67] T C Ransohoff and C J Radke. “Mechanisms of foam generation in glass-bead packs”. In: *SPE Res. Eng.* 3 (1988), p. 573. DOI: 10.2118/15441-PA.

[68] *Foam Generation in Porous Media*. Vol. SPE-75177-MS. SPE Improved Oil Recovery Conference. 2002. DOI: 10.2118/75177-MS.

[69] S. I. Kam and W. R. Rossen. “A Model for Foam Generation in Homogeneous Media”. In: *SPE Journal* 8.04 (Dec. 2003), pp. 417–425. ISSN: 1086-055X. DOI: 10.2118/87334-PA. eprint: https://onepetro.org/SJ/article-pdf/8/04/417/2579323/spe-87334-pa.pdf. URL: https://doi.org/10.2118/87334-PA.

[70] A C Payatakes and Madalena M Dias. “Immiscible microdisplacement and ganglion dynamics in porous media”. In: *Reviews in Chemical Engineering* 2.2 (1984), pp. 85–174. DOI: 10.1515/REVCE.1984.2.2.85.

[71] J G Roof. “Snap-off of oil droplets in water-wet pores”. In: *Soc. Petro. Eng. J.* 10 (1970), p. 85. DOI: 10.2118/2504-PA.

[72] William R. Rossen. “A critical review of Roof snap-off as a mechanism of steady-state foam generation in homogeneous porous media”. In: *Colloids and Surfaces A: Physicochemical and Engineering Aspects* 225.1 (2003), pp. 1–24. ISSN: 0927-7757. DOI: https://doi.org/10.1016/S0927-7757(03)00309-1. URL: https://www.sciencedirect.com/science/article/pii/S0927775703003091.

[73] A C Payatakes. "Dynamics of Oil Ganglia During Immiscible Displacement in Water-Wet Porous Media". In: *Annual Review of Fluid Mechanics* 14.1 (1982), pp. 365–393. DOI: 10.1146/annurev.fl.14.010182.002053. eprint: https://doi.org/10.1146/annurev.fl.14.010182.002053. URL: https://doi.org/10.1146/annurev.fl.14.010182.002053.

[74] S. Tomotika and Geoffrey Ingram Taylor. "On the instability of a cylindrical thread of a viscous liquid surrounded by another viscous fluid". In: *Proceedings of the Royal Society of London. Series A - Mathematical and Physical Sciences* 150.870 (1935), pp. 322–337. DOI: 10.1098/rspa.1935.0104. eprint: https://royalsocietypublishing.org/doi/pdf/10.1098/rspa.1935.0104. URL: https://royalsocietypublishing.org/doi/abs/10.1098/rspa.1935.0104.

[75] Rachel Liontas et al. "Neighbor-induced bubble pinch-off: novel mechanisms of in situ foam generation in microfluidic channels". In: *Soft Matter* 9 (46 2013), pp. 10971–10984. DOI: 10.1039/C3SM51605A. URL: http://dx.doi.org/10.1039/C3SM51605A.

[76] Min Chen, Yannis C. Yortsos, and William R. Rossen. "Pore-network study of the mechanisms of foam generation in porous media". In: *Phys. Rev. E* 73 (3 Mar. 2006), p. 036304. DOI: 10.1103/PhysRevE.73.036304. URL: https://link.aps.org/doi/10.1103/PhysRevE.73.036304.

[77] *Conditions for Foam Generation in Homogeneous Porous Media*. Vol. SPE-75176-MS. SPE/DOE Improved Oil Recovery Symposium. Apr. 2002. DOI: 10.2118/75176-MS.

[78] Fredrik K. Eriksen et al. "Transition from viscous fingers to compact displacement during unstable drainage in porous media". In: *Phys. Rev. Fluids* 7 (1 Jan. 2022), p. 013901. DOI: 10.1103/PhysRevFluids.7.013901. URL: https://link.aps.org/doi/10.1103/PhysRevFluids.7.013901.

[79] Volker Reichenberger et al. "A mixed-dimensional finite volume method for two-phase flow in fractured porous media". In: *Advances in Water Resources* 29.7 (2006), pp. 1020–1036. ISSN: 0309-1708. DOI: https://doi.org/10.1016/j.advwatres.2005.09.001. URL: https://www.sciencedirect.com/science/article/pii/S0309170805002150.

[80] A.E. Scheidegger. "Theoretical models of porous matter". In: *Producers Monthly* 17 (1953), pp. 17–23.

[81] A.E. Scheidegger. *The physics of flow through porous media*. University of Toronto Press, 1974.

[82] R. L. Fleischer and P. B. Price. "Tracks of Charged Particles in High Polymers". In: *Science* 140.3572 (1963), pp. 1221–1222. DOI: 10.1126/science.140.3572.1221. eprint: https://www.science.org/doi/pdf/10.1126/science.140.3572.1221. URL: https://www.science.org/doi/abs/10.1126/science.140.3572.1221.

[83] J. Kozeny. "Uber kapillare Leitung des Wassers im Boden (Aufstieg, Versickerung und Anwendung auf die Bewasserung)." In: *Sitzungsber. Akad. Wiss. in Wien, Mathematisch-Naturwissenschaftliche Klasse, Abt. IIa* 136.(2a) (1937), pp. 271–306.

[84] P.C. Carman. "Fluid Flow through Granular Beds". In: *Trans. Inst. Chem. Eng. Lond.* 15 (1937), pp. 150–166.

[85] Santanu Sinha et al. "Effective rheology of bubbles moving in a capillary tube". In: *Phys. Rev. E* 87 (2 Feb. 2013), p. 025001. DOI: 10.1103/PhysRevE.87.025001.

[86] Subhadeep Roy, Santanu Sinha, and Alex Hansen. "Role of Pore-Size Distribution on Effective Rheology of Two-Phase Flow in Porous Media". In: *Frontiers in Water* 3 (2021). ISSN: 2624-9375. DOI: 10.3389/frwa.2021.709833. URL: https://www.frontiersin.org/articles/10.3389/frwa.2021.709833.

[87] I. Fatt. "The Network Model of Porous Media". In: *Transactions of the AIME* 207.01 (Dec. 1956), pp. 144–181. ISSN: 0081-1696. DOI: 10.2118/574-G. eprint: https://onepetro.org/TRANS/article-pdf/207/01/144/2176635/spe-574-g.pdf. URL: https://doi.org/10.2118/574-G.

[88] Qingrong Xiong, Todor G. Baychev, and Andrey P. Jivkov. "Review of pore network modelling of porous media: Experimental characterisations, network constructions and applications to reactive transport". In: *Journal of Contaminant Hydrology* 192 (2016), pp. 101–117. ISSN: 0169-7722. DOI: https://doi.org/10.1016/j.jconhyd.2016.07.002. URL: https://www.sciencedirect.com/science/article/pii/S016977221630122X.

[89] Richard Chandler et al. "Capillary displacement and percolation in porous media". In: *Journal of Fluid Mechanics* 119 (1982), pp. 249–267. DOI: 10.1017/S0022112082001335.

[90] Marek Cieplak and Mark O. Robbins. "Influence of contact angle on quasistatic fluid invasion of porous media". In: *Phys. Rev. B* 41 (16 June 1990), pp. 11508–11521. DOI: 10.1103/PhysRevB.41.11508. URL: https://link.aps.org/doi/10.1103/PhysRevB.41.11508.

[91] V. Joekar-Niasar and S. M. Hassanizadeh. "Analysis of Fundamentals of Two-Phase Flow in Porous Media Using Dynamic Pore-Network Models: A Review". In: *Critical Reviews in Environmental Science and Technology* 42.18 (2012), pp. 1895–1976. DOI: 10.1080/10643389.2011.574101. eprint: https://doi.org/10.1080/10643389.2011.574101. URL: https://doi.org/10.1080/10643389.2011.574101.

[92] Eyvind Aker et al. "A Two-Dimensional Network Simulator for Two-Phase Flow in Porous Media". In: *Transport in Porous Media* 32.2 (Aug. 1998), pp. 163–186. DOI: 10.1023/A:1006510106194. URL: https://doi.org/10.1023/A:1006510106194.

[93] Santanu Sinha et al. "Fluid Meniscus Algorithms for Dynamic Pore-Network Modeling of Immiscible Two-Phase Flow in Porous Media". In: *Front. Phys.* 8 (2021), p. 548497. DOI: 10.3389/fphy.2020.548497.

[94] R.B. Bird, R.C. Armstrong, and O. Hassager. *Dynamics of polymeric liquids. Vol. 1, 2nd Ed. : Fluid mechanics*. John Wiley and Sons Inc., New York, NY, Jan. 1987.

[95] Yunwu Xiong et al. “Impact of pore structure and morphology on flow and transport characteristics in randomly repacked grains with different angularities”. In: *Soils and Foundations* 59.6 (2019), pp. 1992–2006. ISSN: 0038-0806. DOI: https://doi.org/10.1016/j.sandf.2019.10.002.

[96] George H. Weiss. “Random walks and random environments, volume 1: Random walks”. In: *Journal of Statistical Physics* 82.5 (1996), pp. 1675–1677. ISSN: 1572-9613. DOI: 10.1007/BF02183400.

[97] Theodore W Burkhardt. “The random acceleration process in bounded geometries”. In: *Journal of Statistical Mechanics: Theory and Experiment* 2007.07 (July 2007), P07004–P07004. DOI: 10.1088/1742-5468/2007/07/p07004.

[98] F. Mori, S. N. Majumdar, and G. Schehr. “Distribution of the time between maximum and minimum of random walks”. In: *Physical Review E* 101.5 (May 2020). ISSN: 2470-0053. DOI: 10.1103/physreve.101.052111.

[99] David S Dean et al. “Diffusion in periodic, correlated random forcing landscapes”. In: *Journal of Physics A: Mathematical and Theoretical* 47.37 (Aug. 2014), p. 372001. ISSN: 1751-8121. DOI: 10.1088/1751-8113/47/37/372001.

[100] S. N. Majumdar, A. Rosso, and A. Zoia. “Time at which the maximum of a random acceleration process is reached”. In: *Journal of Physics A: Mathematical and Theoretical* 43.11 (Mar. 2010), p. 115001. DOI: 10.1088/1751-8113/43/11/115001.

[101] B. Mauroy et al. “An optimal bronchial tree may be dangerous”. In: *Nature* 427.6975 (Feb. 2004), pp. 633–636. DOI: 10.1038/nature02287. URL: https://doi.org/10.1038/nature02287.

[102] B. Derrida and H. Spohn. “Polymers on disordered trees, spin glasses, and traveling waves”. In: *Journal of Statistical Physics* 51.5 (June 1988), pp. 817–840. ISSN: 1572-9613. DOI: 10.1007/BF01014886. URL: https://doi.org/10.1007/BF01014886.

[103] Satya N. Majumdar and P.L. Krapivsky. “Extreme value statistics and traveling fronts: various applications”. In: *Physica A: Statistical Mechanics and its Applications* 318.1 (2003). STATPHYS - Kolkata IV, pp. 161–170. ISSN: 0378-4371. DOI: https://doi.org/10.1016/S0378-4371(02)01422-X. URL: https://www.sciencedirect.com/science/article/pii/S037843710201422X.

[104] Satya N. Majumdar and P. L. Krapivsky. “Extremal paths on a random Cayley tree”. In: *Phys. Rev. E* 62 (6 Dec. 2000), pp. 7735–7742. DOI: 10.1103/PhysRevE.62.7735. URL: https://link.aps.org/doi/10.1103/PhysRevE.62.7735.

[105] Satya N. Majumdar and P. L. Krapivsky. “Extreme value statistics and traveling fronts: Application to computer science”. In: *Phys. Rev. E* 65 (3 Feb. 2002), p. 036127. DOI: 10.1103/PhysRevE.65.036127. URL: https://link.aps.org/doi/10.1103/PhysRevE.65.036127.

[106] L.-P. Arguin, A. Bovier, and N. Kistler. "Genealogy of extremal particles of branching Brownian motion". In: *Communications on Pure and Applied Mathematics* 64.12 (Aug. 2011), pp. 1647–1676. DOI: 10.1002/cpa.20387. URL: https://doi.org/10.1002/cpa.20387.

[107] Kabir Ramola, Satya N. Majumdar, and Grégory Schehr. "Branching Brownian motion conditioned on particle numbers". In: *Chaos, Solitons, Fractals* 74 (May 2015), pp. 79–88. DOI: 10.1016/j.chaos.2014.12.013. URL: https://doi.org/10.1016/j.chaos.2014.12.013.

[108] Edward W. Washburn. "The dynamics of capillary flow". In: *Physical Review* 17 (1921), p. 273. DOI: 10.1103/PhysRev.17.273.

[109] Eyvind Aker et al. "A two-dimensional network simulator for two-phase flow in porous media". In: *Transport in porous media* 32.2 (1998), p. 163. DOI: 10.1023/A:1006510106194.

[110] Roland Lenormand, Eric Touboul, and Cesar Zarcone. "Numerical models and experiments on immiscible displacements in porous media". In: *Journal of Fluid Mechanics* 189 (1988), pp. 165–187. DOI: 10.1017/S0022112088000953.

[111] Olav Inge Frette et al. "Immiscible displacement of viscosity-matched fluids in two-dimensional porous media". In: *Phys. Rev. E* 55 (1997), p. 2969. DOI: 10.1103/PhysRevE.55.2969.

[112] Grunde Løvoll et al. "Competition of gravity, capillary and viscous forces during drainage in a two-dimensional porous medium, a pore scale study". In: *Energy* 30 (2005), p. 861. DOI: 10.1016/j.energy.2004.03.100.

[113] ML Hoefner and H Scott Fogler. "Pore evolution and channel formation during flow and reaction in porous media". In: *AIChE Journal* 34.1 (1988), pp. 45–54.

[114] Bernard Derrida. "Random-energy model: An exactly solvable model of disordered systems". In: *Phys. Rev. B* 24 (5 Sept. 1981), pp. 2613–2626. DOI: 10.1103/PhysRevB.24.2613. URL: https://link.aps.org/doi/10.1103/PhysRevB.24.2613.

[115] Satya N. Majumdar, Arnab Pal, and Grégory Schehr. "Extreme value statistics of correlated random variables: A pedagogical review". In: *Physics Reports* 840 (2020). Extreme value statistics of correlated random variables: A pedagogical review, pp. 1–32. ISSN: 0370-1573. DOI: https://doi.org/10.1016/j.physrep.2019.10.005. URL: https://www.sciencedirect.com/science/article/pii/S0370157319303291.

[116] Marc Mézard, Giorgio Parisi, and Miguel Angel Virasoro. *Spin glass theory and beyond: An Introduction to the Replica Method and Its Applications*. Vol. 9. World Scientific Publishing Company, 1987.

[117] Bernard Derrida and Peter Mottishaw. "On the genealogy of branching random walks and of directed polymers". In: *EPL (Europhysics Letters)* 115.4 (Aug. 2016), p. 40005. DOI: 10.1209/0295-5075/115/40005. URL: https://doi.org/10.1209/0295-5075/115/40005.

[118] Xiangyu Cao et al. “Liouville Field Theory and Log-Correlated Random Energy Models”. In: *Phys. Rev. Lett.* 118 (9 Feb. 2017), p. 090601. DOI: 10.1103/PhysRevLett.118.090601. URL: https://link.aps.org/doi/10.1103/PhysRevLett.118.090601.

[119] Éric Brunet and Bernard Derrida. “A Branching Random Walk Seen from the Tip”. In: *Journal of Statistical Physics* 143.3 (Apr. 2011), p. 420. ISSN: 1572-9613. DOI: 10.1007/s10955-011-0185-z. URL: https://doi.org/10.1007/s10955-011-0185-z.

[120] Xiangyu Cao, Yan V. Fyodorov, and Pierre Le Doussal. “One step replica symmetry breaking and extreme order statistics of logarithmic REMs”. In: *SciPost Phys.* 1 (2016), p. 011. DOI: 10.21468/SciPostPhys.1.2.011. URL: https://scipost.org/10.21468/SciPostPhys.1.2.011.

[121] AN Kolmogorov, IG Petrovsky, and NS Piskunov. “Investigation of the equation of diffusion combined with increasing of the substance and its application to a biology problem”. In: *Bull. Moscow State Univ. Ser. A: Math. Mech* 1.6 (1937), pp. 1–25.

[122] M. Bramson. *Convergence of Solutions of the Kolmogorov Equation to Traveling Waves*. 1983.